Entropies and predictability of variability indices of the tropical Pacific

D I S S E R T A T I O N

zur Erlangung des akademischen Grades

doctor rerum naturalium

(dr. rer. nat.)

im Fach Physik

eingereicht an der

Mathematisch-Naturwissenschaftlichen Fakultät I

Humboldt-Universität zu Berlin

von

Herr Lic. en Física Aplicada Luis Eduardo Ortiz Tánchez

geboren am 23.05.1979 in Guatemala Stadt, Guatemala

Präsident der Humboldt-Universität zu Berlin:
Prof. Dr. Jürgen Mlynek

Dekan der Mathematisch-Naturwissenschaftlichen Fakultät I:
Prof. Thomas Buckhout, PhD

Gutachter:

1. Prof. Dr. Werner Ebeling
2. Prof. Dr. Karl Lanius
3. Dr. habil. Rainer Feistel

eingereicht am:	15. April 2004
Tag der mündlichen Prüfung:	12. August 2004

Abstract

This doctoral thesis is concerned with the problems of the predictability and the temporal structure of indices of the climatic variability in the tropical Pacific, which is known in the scale of decades as El Niño-Southern Oscillation (ENSO). For this purpose, time series of the anomalies and persistences of the Southern Oscillation Index (SOI), Multivariate ENSO Index (MEI) and of the Sea Surface Temperature (SST) were investigated. Methods of the dynamical and conditional shannon entropies were applied for the investigation of the predictability of symbolic sequences derived from the time series. The investigation of the conditional entropies for symbolic sequences shows that the most probable Events of ENSO occur after constant short sequences. Time correlations are found for several events; these determine the predictability of a sequence as a function of its length. The evolutions of short sequences representing transitions between ENSO states are relatively less predictable. The most predictable short sequences have been studied in detail. It was further found that, in most cases, SST is the most reliable information source. The analysis of the wavelet spectra of the time series shows strong periodicities of 2 to 4 years, which appear between 1900 and 1960, and between 1970 and 2000 in ENSO. There is evidence of a non-markovian process being responsible for these frequency components. Furthermore, the anomalies of the SST series show a gradient of frequency components towards smaller periods.

Keywords:
ENSO, Shannon entropy, Predictability, Time series

Zusammenfassung

Die folgende Arbeit befasst sich mit der Vorhersagbarkeit und der zeitlichen Struktur von Indizes der klimatischen Variabilität des tropischen Pazifiks, bekannt in der Jahrzentenskala als El-Niño-Southern Oscillation (ENSO). Untersucht wurden die Zeitreihen der Anomalien und Persistenzen der Southern Oscillation Index (SOI), den Multivariate ENSO Index (MEI) und die Meeresoberflächentemperatur (SST). Methoden der dynamischen und bedingten schannonschen Entropien wurden für die Untersuchung der Vorhersagbarkeit von symbolischen Sequenzen der Zeitreihen angewendet. Die Untersuchung der bedingten Entropien für symbolische Sequenzen ergibt, dass die meist vorhersagbare Evente von ENSO nach konstanten Teilsequenzen stattfinden. Für mehrere Evente sind zeitliche Korrelationen nachweisbar, die die Vorhersagbarkeit eines Symbols nach einer Teilsequenz in Funktion derer Länge bestimmen. Die Evolution nach Teilsequenzen, die Übergangszuständen entsprechen, sind mit vergleichsweise niedrigeren Vorhersagbarkeiten versehen. Dabei ist auf die meist vorhersagbaren Teilsequenzen im Detail eingegangen. Es wurde weiterhin festgestellt, dass sich die SST in den meisten Fällen als die zuverlässigste Informationsquelle erweist. Die Analyse der Waveletspektren der Zeitreihen zeigt starke Periodizitäten der Ordnung zwischen 2 und 4 Jahren, die zwischen 1900 und 1960, und 1970 und 2000 in ENSO auftreten. Es besteht Evidenz dafür, dass diese Frequenzkomponenten nicht von einem gefiteten Markovprozess erster Ordnung zurückzuführen sind. Eine Steigung der Frequenzkomponenten zu niedrigeren Perioden ist weiterhin in den Anomalien der Meerestemperatur vorzuweisen.

Schlagwörter:
ENSO, Shannon Entropie, Vorhersagbarkeit, Zeitreihen

Contents

List of Figures

List of Tables

Introduction

The prediction and characterization of time series are two very important topics of modern physical research. It is the investigation and development of methods on these themes where statistical physics and nonlinear dynamics have most contributed to the most diverse branches of human knowledge in the last years. Applications to time series analysis of the concepts related with information and chaos have provided an extremely revealing and fertile insight in the processes underlying, to cite a few, climatology, economics, physiology and linguistics.

The implementation of these methods in the climatic research has allowed important steps towards the understanding of problems such as the predictability of synoptic weather systems or the mechanisms for the onset of abrupt climatic changes. Nevertheless, there is still much to be done, especially for phenomena which occur regularly in an unexpected manner. One problem of this kind is the inderdecadal climatic variability, known in the tropical Pacific as El Niño and the Southern Oscillation.

Though much efforts have been put in the solution of this problem by developing theoretical models, the predictions obtained with them have been — especially recently — of limited utility. Hence, statistical approaches from time series analysis remain interesting and relevant for investigating the predictability of the process underlying the phenomenon. Furthermore, the time-

dependent structure of the variability in the Pacific remains difficult to characterize. As some indices of the varibility in the Pacific appear not to differ from noise, it is particularly interesting to investigate their structure in the time.

This work addresses the problems of the predictability and time structure of the El Niño and the Southern Oscillation with methods apt to respond to the problematic presented above. In the first chapter, the information-theoretical concept of Shannon entropy will be introduced and its relationship to the predictability of a sequence when some foreknowledge is given will be derived. The second chapter is devoted to a detailed insight in the problematic of the interdecadal variability in the tropical Pacific, emphatizing its physical grounds and referring to up-to-date literature. Chapter three contains the application of the method of the Shannon entropies to three indices of the Southern Oscillation. These indices are related to the atmospheric and oceanographical variability and represent the most important documentation on observations of the phenomenon. The fourth chapter introduces modern wavelet analysis and makes use of it for the seach of regions of the indices having structural differences to the rest of the series.

The motivation for this work lies in a personal experience of El Niño in 1997-98, as in the long tradition of adressing diverse time series with information-theorethical methods in the Department of Statistical Physics at the Humboldt University in Berlin. It is my wish to have collaborated with this work to the understanding of the predictabiliy and time-structure of this important problem.

Chapter 1

Entropy and Predictability

Meteorology, economics and physiology are only three examples of branches of human knowledge whose variables are often represented as time series. A time series can be defined as a series of observations of the relization of a process during the interval $(0, T)$ at the times $\Delta t, 2\Delta t, ..., n\Delta t = T$. This representation is very useful for stationary processes since it allows for consistent estimates of the autocovariance and autocorrelation functions, as well as consistent estimates of the frequency spectrum using the technique of a spectral window [94]. The importance of this properties lies in the definition of a consistent estimator: it is one whose variance tends to zero when the number of observations tends to infinity. Usually, interesting time series are those of chaotic or stochastic processes, for which the frequency spectrum is not trivial.

Time series analysis is useful for forecasting, qualitative classification and quantitative characterization of processes [16, 89, 129]. We will stick to the first objective, forecasting, introducing methods of information theory and significance tests to investigate the time series. The most important issue we will address is: How can one quantify the uncertainty of a time series? To answer this question, we will first restrict our attention to processes in discrete

time taking discrete values.

1.1 Shannon's Entropy

Let X be a stochastic process taking discrete values $(x_1, ..., x_n)$ with a probability distribution $(p_1, ..., p_n)$. Is it possible to find a function H which quantifies the uncertainty associated with this distribution?

In an axiomatic approach derived by Shannon [99] and complemented by Kinchin [54] and others, H can be derived from the following postulates:

1. H must be a continuous function of the p_i.

2. If all p_i are equal, the quantity $A(n) = H(1/n, ..., 1/n)$ is a monotonic increasing function of n.

3. $H(p_1, .., p_n)$ does not depend on the order of the p_i, that is, under an arbitrary permutation $\{a_1, ..., a_n\}$ of the set $\{1, ..., n\}$, $H(p_1, ..., p_n) = H(p_{a_1}, ..., p_{a_n})$. This condition is known as symmetry.

4. The composition law: We group the first k events in a first composite event with probability $w_1 = p_1 + ... + p_k$, the next j events in a second composite event with probability $w_2 = p_{k+1} + ... + p_{k+j}$, and so on. The conditional probabilities for the individual events of the first group are then $(p_1/w_1, ..., p_k/w_1)$, given that the first composite event has ocurred, and similarly for the other groups. For the measure H to be consistent, its value should be the same directly for the probabilities of the individual events or for them after being composed in any set of groups. This can be written as

$$H(p_1,...,p_k) = H(w_1,w_2,...)+w_1H(p_1/w_1,...,p_k/w_1)+w_2H(p_{k+1}/w_2,...,p_{k+m}/w_2)+... \tag{1.1}$$

where the weighting factors as w_1 appear in the second term of the right hand side of equation (1.1) because the additional uncertainty $H(p_1/w_1,...,p_k/w_1)$ is encountered only with probability w_1.

To derive the form of H, starting from condition (1), given the density of the rationals, it is sufficient to determine H for this set of values for the probabilities. Taking n_i possible events of the sort i, its associated probabilities are

$$p_i = n_i/\sum n_i. \tag{1.2}$$

Now we can consider the decomposition of the distribution $(p_1,...,p_n)$ in $\sum n_i$, $i = 1,...n$ events of equal probability p'. In this way, from each p_i arise n_i elements with the value of p' and $p'/p_i = 1/n_i$. Now the original distribution is a composite set of probabilities in the sense of equation (1.1). This gives from the composition law

$$H(p'_1,...,p'_{\sum n_i}) = H(p_1,...,p_n) + p_1H(p'_1/p_1,...,p'_k/p_1) + .. \tag{1.3}$$

or, recalling the definition of A from the second condition,

$$A(\sum n_i) = H(p_1,...,p_n) + \sum_i p_iA(n_i). \tag{1.4}$$

Taking moreover a decomposition which makes all n_i equal to m, the last equation reduces to

$$A(mn) = A(m) + A(n) \tag{1.5}$$

which is uniquely solved setting [99]

$$A(n) = K \log n \tag{1.6}$$

where $K > 0$ due to condition (2). A substitution of the latter equation in the equation (1.4) gives

$$\begin{aligned} H(p_1, ..., p_n) &= K \log(\sum n_i) - K \sum p_i \log n_i \\ &= -K \sum_i p_i \log p_i \end{aligned} \tag{1.7}$$

This is Shannon's entropy, whose name is explained from the similarity to Boltzmann's entropy in statistical physics. It is a fundamental quantity in the application of information theory to dynamical systems and time series analysis. The property of symmetry is moreover necessary to achieve the so-called characterization theorem [66].

1.1.1 Properties of the Shannon Entropy

Some useful properties of the Shannon Entropy derived from its basic axioms are:

1. $H(p) \geq 0$, with equality when $p_i = 1$ and $p_i = 0$ for all i. Zero entropy implies that the process is deterministic.

2. $H(p) \leq H(1/n, ..., 1/n)$, with the equality holding only when $p_i = 1/n$ for all $i = 1, ..., n$. This implies that the maximum entropy is attained when all probabilities are equal.

3. Considering two probability distributions $P = (p_1, ..., p_n)$ and $Q = (q_1, ..., q_m)$ associated with independent random variables X and Y. The joint probability distribution is

$$P(X = x_i, Y = y_i) = p_i q_j, \quad i = 1, 2, ...n; j = 1, 2, ..., m. \tag{1.8}$$

The entropy of the joint distribution equals the sum of the entropies associated with the independent random variables, i.e.

$$H(p_1 q_1, ..., p_1 q_m; ...; p_n q_1, ..., p_n q_n) = H(p_1, ..., p_n) + H(q_1, ..., q_m). \tag{1.9}$$

This property is called additivity.

1.1.2 The Maximum Entropy principle

In his papers of 1957 [48,49], E.T. Jaynes posed the following question: Let us imagine that X assume the discrete values $\{x_1, ..., x_n\}$ and that we do not have any knowledge about the corresponding probabilities $\{p_1, ..., p_n\}$. If we only know the expected value of a function $f(x) = \sum p_i f(x_i)$, is it possible to determine the expected value of other function $g(x)$?

Up to that date, the stand of knowledge in this inference problem was represented by Laplace's principle of insufficient reason, which asserts that two events are to be assigned equal probabilities if there is no reason to think otherwise. Nevertheless, it has been shown that the Shannon entropy is the only consistent measure of the amount of uncertainty represented by a discrete probability distribution. On this light Jaynes could postulate that the only unbiased and noncommital assignment of probabilities, that is, the only probability distribution which makes no assumptions other than the constraints of the system, should be the one that maximizes the entropy.

It is then required to solve the equation

$$\max H(p_1, ..., p_n) = \sum p_i \log p_i \tag{1.10}$$

subject to the constraints of the probability norm and, for the sake of generality, the knowledge of n expected values of the functions f_i

$$\sum p_i f_i(x_i) = < f_i(x) > \tag{1.11}$$

$$\sum p_i = 1 \tag{1.12}$$

An application of the method of Lagrange multipliers gives the probabilities

$$p(x_i) = e^{-\lambda_0 - \lambda_1 f_1(x_i) - ... - \lambda_n f_n(x_i)} \tag{1.13}$$

where the constants λ_i are given from

$$\lambda_0 = \ln Z, \tag{1.14}$$

$$Z(\lambda_1, ..., \lambda_n) = \sum_i \exp\{-[\lambda_1 f_1(x_i) + ... + \lambda_n f_n(x_i)]\} \tag{1.15}$$

and

$$< f_i(x) >= -\frac{\partial}{\partial \lambda_i} \ln Z, \tag{1.16}$$

and the calculation of the entropy gives

$$H_{max} = \lambda_0 + \lambda_1 < f_i(x) > + ... + \lambda_n < f_n(x) > . \tag{1.17}$$

These results are remarkable since, by adding the Boltzmann constant k_B as the proportionality factor for the international metric system, where the entropy has the dimension of energy divided by temperature, they repeat the results of conventional statistical mechanics. It is found, for instance, that the

Boltzmann distribution of a canonical ensemble is reattained in the maximum entropy formulation, giving the average energy $< E >$ and its possible levels $\{E_1, ..., E_m\}$, for a system of distinguishable particles. The known probabilities, partition function and parameters are found,

$$\begin{aligned} p_i &= e^{-\lambda_0 - \lambda_1 f_1(x)} \\ &= \tfrac{1}{Z} e^{-\frac{1}{k_B T} E_i} \end{aligned} \tag{1.18}$$

and

$$Z = \sum_i e^{-\frac{1}{k_B T} E_i} \tag{1.19}$$

$$\lambda_0 = \ln Z \tag{1.20}$$

$$\lambda_1 = 1/k_B T, \tag{1.21}$$

as are those of the Gibbs distribution for a grand canonical ensemble when the maximum entropy formalism is applied to the expected value $< E >$, its possible states E_i and the mean occupation numbers $< n_i >$ of the $i = 1...s$ kinds of particles, namely

$$\begin{aligned} p_{i,j} &= e^{-\lambda_0 - \lambda_1 n_1 - ... - \beta E_i(n_j)} \\ &= \tfrac{1}{Z} e^{\sum_j (\mu_j n_j - \frac{1}{k_B T} E_i n_j)} \end{aligned} \tag{1.22}$$

and

$$Z = \sum_{j=1}^{s} \sum_{i=1}^{n} e^{\sum_j (\mu_j n_j - \frac{1}{k_B T} E_i(n_j))} \tag{1.23}$$

$$\mu_i = -k_B T \lambda_i \tag{1.24}$$

$$\beta = 1. \tag{1.25}$$

There are many important consequences of these results. First, a non-physical aspect of statistical physics is found, since it coincides with the best possible method of making inferences about a macroscopic system, according to Jaynes. Statistical physics maintains its full physical sense by enumerating the states of a system and its microscopic properties, but is an example of a pure inference problem in a statistical sense. This deprives some basic assumptions of Boltzmann's statistical mechanics of their fundamental character for predicting observables, such as ergodicity and the equal *a priori* probabilities of the microcanonical ensemble.

Another important consequence is that only new experimental findings allow one to make better predictions about the static state of the system, since there is no more general theory than statistical physics to attack such problems. A theoretical development such as, for example, the discovery of new integrals of the motion, which would imply that the system does not obey metrical transitivity, is not enough to exclude a region of phase space that the experimental information has not yet ruled out.

Paying attention to these results, the fundamental reason for the coincidence of statistical mechanics with the maximum entropy inference lies in the form of the distribution found with both methods. In systems with a very large number of degrees of freedom, the probability distribution possesses a single extremely sharp peak, which includes practically the whole "mass"of the distribution. Thus it is explained that the uncertainty for this class of systems is very small and is appropriately described using the mean values as the expected values. This is the entropy concentration theorem.

Since Shore and Johnson [100] axiomatized the desirable properties of inference methods, it is shown that the maximum entropy principle is unique and the is only correct method for inductive inference when new information

is given in the form of expected values. Hence, there are many other applications of the principle of maximum entropy. One of them will be found in the selection of a partition in creating symbolic sequences.

1.2 Symbolic Dynamics

We can describe continuous dynamical systems by means of the vectors of their trajectories $\boldsymbol{x}$ in a d-dimensional phase space $\boldsymbol{\Gamma} \in \mathbb{R}^d$. The dynamics of the system is given by a mapping f^t acting in $\boldsymbol{\Gamma} \to \boldsymbol{\Gamma}$. The time evolution is given in the same way with the mapping f^t where t is an integer and stands for the succesion of numbered instants of time in which the state of the system is determined, giving the flux of the trajectories with the properties

$$f^0(\boldsymbol{x}) = \boldsymbol{x}, \quad \boldsymbol{x} \in \boldsymbol{\Gamma} \tag{1.26}$$

$$f^{t_1}(f^{t_2}(\boldsymbol{x})) = f^{t_1+t_2}(\boldsymbol{x}). \tag{1.27}$$

In general, dynamical systems consist of d first-order differential equations for the components of (x)

$$\frac{d}{dt}\boldsymbol{x} = \boldsymbol{M}(\boldsymbol{x}), \qquad \boldsymbol{M}(\boldsymbol{x}) : \mathbb{R}^d \to \mathbb{R}^d. \tag{1.28}$$

However, the utility of the Shannon entropy is limited to symbolic series at discrete times, so first of all should be the time discretized. For this purpose, the two most important methods are the following:

1) The Poincaré map: Taking the intersections of the trajectories with a predefined hyperplane in $d' < d$ dimensions, or
2) Taking equidistant timings, with $(t = t_0 + n\Delta t)$
for $n = 1, ...n_{max}$

Now the evolution in the time is given with the discrete process $\boldsymbol{X}$

$$\boldsymbol{x_{n+1}} = \boldsymbol{F}(\boldsymbol{x_n}). \tag{1.29}$$

and the new sequence obtained with the discretization of the time is called the orbit, whose time evolution is found applying the invertible mapping $\boldsymbol{F}$. However, $\boldsymbol{F}$ is not easily found from the differential equations for the continuous system. It is now necessary to convert the sequence of numbers of the orbit in a symbolic sequence. For this means we proceed to partition the space $\boldsymbol{\Gamma}$.

1.2.1 Dynamical refinement and the generating partition

We define a finite partition $\mathcal{P} = (P_1, P_2, ..., P_l)$, which partitions the space $\boldsymbol{\Gamma}$ in its integrity in l disjoint subsets P_i, i.e.

$$\cup_{i=1}^{l} P_i = \boldsymbol{\Gamma} \tag{1.30}$$

$$P_i \cap P_j = 0 \quad \forall j \neq i \tag{1.31}$$

Now it is necessary to assign a label to each one of the subsets created with the partition. Therefore an alphabet $\mathcal{A} = \{A_1, A_2, ..., A_l\}$ is introduced, which will assign a symbol A_j to every point of the orbit ocurring in the subset P_j. Thus, there is the following mapping from the orbit to the symbolic sequence:

$$S_i = A_j \in \mathcal{A} \longleftrightarrow \boldsymbol{x_i} \in P(j). \tag{1.32}$$

The partitioning process should be designed allowing the minimal, if any, loss of information in the description of the orbit. A way of characterizing this loss is achieved by recalling the initial conditions of the orbit which evolve in a

definite symbolic sequence. The set of initial conditions for a sequence of length N with the symbols $S_1, S_2, ..., S_N$ corresponding to the subsets $P_{S_1}, ..., P_{S_N}$ of $\mathbf{\Gamma}$ is

$$\Gamma_i^N = P_{S1} \cap \boldsymbol{F^{-1}}(P_{S_1}) \cap \boldsymbol{F^{-2}}(P_{S_2}) \cap, ..., \cap \boldsymbol{F^{-N}}(P_{S_N}), \tag{1.33}$$

where i denotes the specific block of length N in question and $\boldsymbol{F^{-i}}(X)$ represents the n-times inverse mapping of X so that $\boldsymbol{F^n}(\boldsymbol{x})$ in the orbit equals the set $\mathbf{\Gamma}$.

Using this theoretical background, it is possible, at least in principle to find a partition which does not create an information loss by encoding a dynamical system; since this procedure applies the dynamics of the system, it is called *dynamical refinement*. The partition which allows no ambiguity by assigning only one initial condition to every infinite symbol sequence of a dynamical system is called the *generating partition* or *generator* [22, 23]. A generating partition is not unique, since it can be divided in a more complex partition in order to attain the same result.

The problem of finding generating partitions for dynamical systems is very dificult. In 1985, Grassberger and Kantz [39] solved it for the Hénon Map, and since then, some solutions have been found for other systems [87].

1.2.2 Entropy of a symbolic sequence

The concept of entropy and its relationship to the predictability has been very fertile in addressing problems of different disciplines [14]. Quantitative aspects of predictability and the detection of correlations have been applied in neuroscience [102, 103], economics [25, 69], meteorology [55, 75, 131], molecular biology and musicology [121] and literature [79], broadening the scope of useful information obtained with statistical physics. For this means, it is necessary

to discretize the time series. One shall thus deal with symbol sequences on a finite alphabet $\mathcal{A} = \{A_1, A_2, ..., A_l\}$ and length N, the alphabet describing the possible discrete values our observations can take. Formally, the time series on a finite set of discrete values of the last subsection is a symbolic sequence. The construction of these sequences from any one-dimensional time series will be the theme of the next section. An interesting question which can be properly addressed with the measure of the entropy is: How does the uncertainty of predicting a symbol on the sequence change after some information on the past symbols is gained? To answer this question it is first necessary that the process from which the sequence is obtained, the *information source*, be stationary and ergodic.

The investigation of symbol sequences is based on the possibility of taking more than one symbol and its probability along the sequence as a subject of study. It is in general possible to take a block of n neighboring symbols (an $n - block$ or $n - word$) and to look for the probability of finding it in the sequence. This probability p_i^n can be estimated with the relative frequency of appearance of the block i with respect to the $N-n+1$ blocks in the sequence, or with other estimators discussed below. Hence, the Shannon entropy H_n of a sequence can depend on the size of the n-blocks and is computed as follows:

$$H_n = -K \sum p_i^n \log p_i^n. \tag{1.34}$$

In the following we will use the constant K equal to $\frac{1}{\log l}$ so that the entropy H_1 is normed to one, since there are l possibilities for the value of a symbol. The equivalent representation for the entropy

$$H_n = -\sum p_i^n \log_l p_i^n. \tag{1.35}$$

will be used throughout this work. This is one possible choice out of many customary norming schemes, these being useful for comparing entropies of

symbol sequences. Another possibility is to set the base of the logarithm equal to two, achieving thereby a measure of the information in bits, appropriate for calculating the uncertainty in terms of information content of binary (digital) procedures. In the appendix 1 we derive Shannon's entropy in this context, showing how it relates to the information needed to simulate a stochastic process. Taking the natural logarithm is useful in theorethical derivations which relate the entropies with thermodynamics, as shown in the previous section, or with the theory of chaos, see the section 2.4.

1.2.3 Statistical properties of the entropy

As the entropy of a real system is a fluctuating quantity, it is interesting to find an analytical derivation of its distribution [24, 51, 132]. It is possible to specificate the distribution of the first-order Shannon-Entropy for a Bernoulli sequence with a binary partition. Writing the probabilities for the symbol corresponding to a given partition as p respectively q, the probability of finding this symbol n times along a sequence of length N is

$$\rho(n) = \binom{N}{n} p^n (1-p)^{N-n}. \tag{1.36}$$

It is shown in [24] that the distribution of the Shannon entropy, due to its symmetry property, after introducing the Kronecker delta, takes the following form

$$\rho(n) = \binom{N}{n} (p^n (1-p)^{N-n} + p^{N-n}(1-p)^n (1-\delta_{n,\frac{N}{2}}). \tag{1.37}$$

There is, nevertheless, no known general expression for the distribution of higher-order entropies. The topic of the variance of the Shannon entropy is

discussed in [40] and [46]. It is suggested in these works that the Bayesian estimate of the probabilites give more accurate entropy values:

$$p_i^{(n)} = \frac{k_i^n + 1}{N + M_n}, \tag{1.38}$$

where k_i^n is the relative frequency of the event i in the order n and M_n is the number of blocks with frequency different than zero, which attains values up to l^n.

This estimate of the entropy will be used in the present study. Finally, as in every time series analysis, there is a deviation from the exact quantities due to finite-length effects. It has been found [41, 43] that the effect of the length of the series is that the entropy is underestimated. An approximation to first order of this bias in the computation of the entropy is given by Herzel [43] when the estimation of the probability is given by the relative frequency $p_i = n_i/N$:

$$\Delta H_n \approx \frac{(M_n - 1)}{2N \log l} \tag{1.39}$$

A more accurate expression is given by Grassberger [38].

1.3 Generalized Entropies

1.3.1 Local, conditional and dynamical entropies

It is interesting to study a probabilistic system described in terms of two random variables X and Y, defined in the same probability space. If X and Y are independent, it is true from the additivity property of the entropies that

$$H(X, Y) = H(X) + H(Y). \tag{1.40}$$

Nevertheless, a statistical dependence between the variables means a smaller uncertainty in the determination of one after the other, so that it is relevant to introduce a quantity $H(X|y_i)$ which represents the amount of uncertainty about X when a specific outcome y_i of Y is observed. This will be called the *local entropy* after y_i,

$$H(X|y_i) = -\sum_{j=1}^{n} p(x_j|y_i) \log p(x_j|y_i). \tag{1.41}$$

Taking the mean of $H(X|y_i)$ over all m y_i's with probabilities $q(y_i)$, we find the *conditional entropy* of X given Y, $H(X|Y)$, that is, the amount of uncertainty remaining about X given foreknowledge of Y:

$$\begin{aligned} H(X|Y) &= -\sum_{i=1}^{n}\sum_{j=1}^{m} q(y_i)p(x_i|y_j) \log p(x_i|y_j) & (1.42) \\ &= -\sum_{i=1}^{n}\sum_{j=1}^{m} p(x_i, y_j) \log p(x_i|y_i). & (1.43) \end{aligned}$$

In the context of a symbolic sequence on an alphabet of ℓ symbols, it is valid to interprete the variable X as the new symbol A_{n+1} with the possible values $A_{(n+1)_i}$ to occur after an n-block $Y = A_n...A_1$. Then the local entropy after a specific block is

$$H(A_{n+1}|A_{n_j}...A_{1_j}) = -\sum_{i=1}^{\ell} p(A_{(n+1)_i}|A_{n_j}...A_{1_j} \log p(A_{(n+1)_i}|A_{n_j}...A_{1_j}) \tag{1.44}$$

and the conditional entropy after any n-block is

$$H(A_{n+1}|A_n...A_1) = -\sum_{i=1}^{\ell}\sum_{j=1}^{\ell} p(A_{(n+1)_i}, A_{n_j}...A_{1_j}) \log p(A_{(n+1)_i}|A_{n_j}...A_{1_j}). \tag{1.45}$$

From the composition law (eq (1.1)), it is true that

$$H(A_{n+1}...A_1) = H(A_n...A_1) + H(A_{n+1}|A_n...A_1), \tag{1.46}$$

since the probability of ocurrence of any block $A_n...A_1$ is equal to one. This can be written in general as

$$H_{n+1} = H_n + H_{n+1|n} \tag{1.47}$$

and so it is possible to define the uncertainty related to the determination of the symbol A_{n+1} after n symbols are known. This is the *dynamical entropy*

$$h_n = H_{n+1} - H_n, \tag{1.48}$$

which is equal to $H_{n+1|n}$. This definition is completed introducing $h_0 = H_1$ so that the uncertainty of determining a symbolic value without prior information is consistent.

1.3.2 Kolmogorov-Sinai Entropy

Of special interest is the so-called *entropy of the source* h, which estimates the *minimal* mean uncertainty in the prediction of a value of a symbolic series, i.e. the rate of information loss in the time [98]. This value

$$h = \lim_{n\to\infty} \frac{H(n)}{n} \tag{1.49}$$

represents the minimal mean uncertainty taking the length of the sequence towards infinity, since a dependence between a symbolic value and its past is reflected in a conditional entropy less than one. As long as these dependences

(correlations) are detected, the value of $\frac{H_n}{n}$ will diminish. To ensure its minimum, a symbolic sequence of a dynamical system has to be followed up to the infinite length. This limit is directly valid for the dynamic entropies so that $h = \lim_{n\to\infty} h_n$. Nevertheless, this quantity still depends on the partition of the orbit used to create the symbolic sequence. In accordance with the principle of maximum entropy, choosing an imperfect partition is equivalent to assuming information not given about the system, a situation which would signify a reduction on the computed entropies. Therefore it is necessary to take the supremum of the entropy for the set of all partitions $\mathcal{P}$. This is the definition of the Kolmogorov-Sinai entropy h_{KS} [23]

$$h_{KS} = \sup_{\mathcal{P}} \lim_{n\to\infty} h_n \tag{1.50}$$

The Kolmogorov-Sinai entropy fulfills a fundamental relationship in the physics of dynamical systems. This is the Pesin theorem, which relates it with the Lyapunov exponents. For a one-dimensional system is the Lyapunov exponent given by

$$\lambda(x_0) = \lim_{n\to\infty} \frac{1}{n} \log \left|\Pi_{i=0}^{n-1} F'(x_i)\right| = \lim_{n\to\infty} \frac{1}{n} \sum_{i=0}^{n-1} \log |F'(x_i)| \tag{1.51}$$

where $F'(x_n)$ is the derivative of the discrete mapping F at the point x_n. As is known, this quantity (whereas a d-dimensional system has d exponents) represents the contraction or expansion (if it is negative or positive, respectively) of the dynamics in the corresponding dimension, i.e. the stability of the system after starting with the initial condition x_0. An expanding direction means consequently that chaos or stochasticity are involved in the process.

The Pesin theorem illuminates the relationship between the rate of uncertainty associated with a prediction, represented by the Kolmogorov-Sinai

entropy, and the rate of divergence of two trajectories with very similar initial conditions, described by the Lyapunov exponents. Since there arises no uncertainty about the future in contractive or neutral fluxes of trajectories, it is understandable that only the positive Lyapunov exponents λ_i^+ contribute to the Kolmogorov-Sinai entropy. In general, using the natural logarithm and $K = 1$ in the normalization of the entropy, the Pesin theorem states that [12]

$$h_{KS} \leq \sum_i \lambda_i^+ \tag{1.52}$$

and in most cases, including the ones to be analyzed here [12, 27, 52]

$$h_{KS} = \sum_i \lambda_i^+ \tag{1.53}$$

.

This corroborates that the greatest dynamical entropy over all partitions is an invariant of the system, to which the Lyapunov exponents are directly related, without a dependece on the coordinate system that is being used. In turn, the interpretation of the positive Lyapunov exponents is transitive to the Kolmogorov-Sinai entropy, which then also measures the amount of chaos or stochasticity in the process. Now that the Lyapunov exponents are much more easily computed, they act in a standard manner as the best estimate for the Kolmogorov-Sinai entropy.

Finally, since the usage of other normalization than $\max H_n = n$ modifies the asymptotic behavior of H_n/n the values of the Kolmogorov-Sinai entropy must be interpreted in a different way than before:

1. Regular motion: $h_{KS} = 0$ as with our usage of the Shannon entropy.

2. Chaotic motion: $0 < h_{KS} < \infty$. The uncertainty due to chaotic indeterminacy of the dynamics of the systems grows to a finite positive value.

3. Stochastic motion: $h_{KS} \to \infty$. The uncertainty due to noise adds itself without a limit. This represents a theorethical difficulty for practical applications, which cannot be avoided in observations or noise-driven model data.

1.3.3 Kullback-Leibler Entropy and Mutual Information

Considering the case of the incomplete knowledge of a process, described by a probability distribution $p_1^0, ..., p_n^0$, it is of interest to pose the problem of how much information is won with a new distribution $p_1, ..., p_n$, e.g. from a new series of measurements. This problem leads to the following examples of *directed divergences*.

With respect to the event i, there is a gain of information of the size

$$k \log(p_i^0)^{-1} - k \log(p_i)^{-1} \tag{1.54}$$

due to the new distribution. By taking the mean value of this information gain relative to the probabilities of the new distribution one obtains the *Kullback-Leibler Entropy* or *Kullback-Leibler directed divergence* [56,57], which for symbolic series takes the form

$$K(p, p^0) = \sum_{i=1}^{l^n} p_i \log \frac{p_i}{p_i^0}. \tag{1.55}$$

Some properties of the Kullback entropy are [23]:

1. $K(p, p^0) \geq 0$ for every probability distribution p and p^0.

2. The minimum $K(p, p^0)$ equals zero and takes place only when both distributions are identical.

3. Its relationship to the Shannon entropy is best observed, when p_0 is a uniform distribution, taking every probability the value $1/r$. Then

$$K(p, p^0) = -H(p) + k \log r \tag{1.56}$$

4. $K(p, p^0)$ is a convex function of the p_i, that is

$$\frac{\partial^2 K}{\partial p_i \partial p_j} \geq 0. \tag{1.57}$$

By taking two probability distributions and calculating the Kullback entropy of the joint distribution as p and the distribution of the pairs of products of probabilities as p^0, the *mutual information* or *transinformation* is obtained. Writing the joint probability of the possible events x_i^0 and x_i as $p(x_i^0, x_i)$ this is defined as

$$T = K(p(x_i^0, x_i), p(x_i^0) \cdot p(x_i)) \tag{1.58}$$

$$T = \sum_i p(x_i^0, x_i) \log \frac{p(x_i^0, x_i)}{p(x_i^0 \cdot p(x_i))} \tag{1.59}$$

This measure is easily expanded to take into account phase differences in the indexing of the sequences. Introducing the index m for the time lag in symbols, it allows the use of the mutual information to look for changes in the correlations related to a time lag between two series, or even within a single one. Maintaining for generality the notation for events of two series, this mutual information can be written as

$$T^{(m)} = \sum_i p^m(x_i^0, x_i) \log \frac{p^m(x_i^0, x_i)}{p(x_i^0 \cdot p(x_i))} \tag{1.60}$$

where the events x_i^0 and x_i occur with a difference in time of m symbols. The mutual information is a very important measure of correlation, especially since it is a direct substitute for the correlation matrix

$$C_{ij}(m,n) = \langle X_i(n) \cdot X_j(n+m) \rangle - \langle X_i(n) \rangle \langle X_j(n+m) \rangle \tag{1.61}$$

for symbolic sequences, for there is no definite multiplication and substraction defined for them. A mapping of the symbols to numbers as done with the mutual information makes possible the expansion of the correlation concept. [44, 61, 101] and give more possibilities to address the problems of predictability and characterizarion of time series [77, 78].

1.3.4 Rényi and Havrda-Charvát entropies

A generalized probability distribution P is one whose *weight* $W(P) = \sum_{k=1}^{n} p_i < 1$. Defining the mean value entropy of the generalized distributions P and Q as

$$H(P \cup Q) = \frac{W(P)H(P) + W(Q)H(Q)}{W(P) + W(Q)} \tag{1.62}$$

and substituting the composition postulate in the derivation of Shannon's entropy with the additivity property,

$$H(P * Q) = H(P) + H(Q), \tag{1.63}$$

Rényi derived another information measure [93]

$$H_\alpha(P) = \frac{1}{1-\alpha} \log \sum_{i=1}^{n} p_i^\alpha, \quad \alpha > 0, \alpha \neq 1 \tag{1.64}$$

which complies with the limit behavior towards the Shannon entropy as

$$\lim_{\alpha\to 1} H_\alpha(P) = -\sum_{i=1}^{n} p_i \log p_i. \tag{1.65}$$

This is an important measure for coding symbolic messages [15, 72] and for the characterization of nonlinear dynamical systems, where the Rényi dimensions play a significant role [12]. The power law behavior, which is characteristic of phenomena having long-range correlations [101] has also been addressed by means of the Rényi entropies, where one finds that the maximum entropy principle applied to Rényi entropies shows that the power law behavior is inherent to them, as the Boltzmann distribution to Shannon's.

Another measure of information H^α was introduced by Havrda and Charvát [42], the main difference with the measures presented above being that it obeys recursivity with a certain power α. The composition takes then the form

$$\begin{aligned} &H^\alpha(p_1, ..., p_{i-1}, r_{i_1}, r_{i_2}, p_{i+1}, ..., p_n; \alpha) \\ &\quad = H^\alpha(p_1, ..., p_{i-1}, p_i, p_{i+1}, p_n; \alpha) + \alpha p_i^\alpha H^\alpha\left(\frac{r_{i_1}}{p_i}, \frac{r_{i_2}}{p_i}; \alpha\right). \end{aligned} \tag{1.66}$$

The measure which fulfills this condition, is continuous for normed probability distributions, does not change if a probability is equal to zero and takes the basic values $H^\alpha(1, \alpha) = 0$ and $H^\alpha(1/2, 1/2, \alpha) = 1$ is found to be [42]

$$H^\alpha(p_1, ..., p_n; \alpha) = \frac{2^{\alpha-1}}{2^{\alpha-1} - 1}\left(1 - \sum_{i=1}^{n} p_i^\alpha\right); \quad \alpha > 0, \alpha \neq 1, \tag{1.67}$$

$$H^1(p_1, ...p_n; 1) = -\sum_{n}^{i=1} p_i \log p_i, \tag{1.68}$$

complying with the limit case to Shannon's entropy. The relationship between this entropy and Rényi's entropy was clearly put by Kapur [53], who wrote H^{α} as

$$H^{\alpha}(P) = \frac{\sum_{i=1}^{n} p_i^{\alpha} - 1}{1-\alpha}, \quad \alpha \neq 1, \alpha > 0, \tag{1.69}$$

since from equations (1.64) and (1.69)

$$H^{\alpha}(P) = \frac{\exp((1-\alpha)H_{\alpha}(P)) - 1}{1-\alpha}, \quad \alpha \neq 1. \tag{1.70}$$

The most important application of this entropy has taken place since Tsallis rediscovered it in the context of nonextensive statistical mechanics, with the aim of generalizing the Boltzmann-Gibbs statistics to generate power-like distributions in equilibrium [117]. Since then, this work has provided a perspective tat has inspired many investigations in this area.

Many other entropy-like forms of information measures useful for nonlinear systems can be found in [107] and several other directed divergences in [20].

1.4 Surrogate Series Analysis

An important aspect of the analysis of time series is the possibility of uncover the character of the process underlying the series. It is especially interesant to discriminate if one time series represents a nonlinear process, a linear process or if it the series does not give more information than random noise would do. One useful tool to address such a question is the method of surrogate time series [97,109]. Surrogate time series are series derived from the original series, which are designed to test against a null hypothesis whether the original series belongs to a definite class of processes, such as those described above.

To construct a set of surrogate series it is required to find some parameters of the original series, which are associated to a definite class of processes. For example, the mutual independence of the data in a symbolic sequence is expressed in statistics which are independent of the relative positions of the symbols. Hence, by maintaining the probabilities of finding each symbol from the original series by making random shuffles of their positions, one constructs a surrogate set of sequences without temporal correlations. Consequently, if the dynamical entropies of order $n \geq 1$ of the original series are not significantly different from those of the surrogates, this can be regarded as evidence for that the original series (and probably the underlying process) describes independent random variables, with no temporal correlations up to the order n.

Nevertheless, it is not a trivial task to find a set of parameters which correspond to a definite class of processes. Only two cases are relatively evident: the one-symbol probabilities, which are conserved in processes of independent variables as above; and the amplitudes of the Fourier transform, which are conserved in processes of linear correlations. In the latter case, the construction of surrogates is possible when the amplitudes of the periodogram estimator of the power spectrum

$$S_k = \frac{1}{N} \sum_{j=0}^{N-1} x_j \exp\left(\frac{i2\pi kj}{N}\right) \tag{1.71}$$

are multiplied by random phases and then transformed back to the time domain:

$$\bar{x_j} = \frac{1}{N} \sum_{k=0}^{N-1} e^{i\alpha_k} |S_k| \exp\left(-\frac{i2\pi kj}{N}\right), \tag{1.72}$$

where $0 \leq \alpha_k \leq 2\pi$ are independent random numbers.

Given a class of parameters which is the desired to represent the process of the null hypothesis, the construction of the surrogates is often not an easy matter as well. One could think the construction of *typical realizations* can be helpful, that is, constructing surrogate series using the specific values of the parameters which characterize the original series. This approach is not very useful, since it requires often fitting procedures, which introduces systematic errors, needs the specification of fitting parameters and leads to series which fluctuate around the data of the original series. On top of that, it is not possible to recover the true underlying process by any fitting. Hence, the most appealing method to construct surrogates is to create *constrained realizations* [110]. For this means, it is useful to consider the measurable properties of the time series rather tan its underlying model equations. This is possible constructing surrogates with the same second order properties as the measured data, but which are otherwise random, as shown above with the frequencies of the data for the sequence of independent random variables, or the Fourier amplitudes for the linear (possibly stochastic) processes. Schreiber [96, 97] describes recent developments in the constrained randomization approach.

To discriminate the character of a process with some high significance, surrogate series are used in hypotheses tests. Rigorous tests are designed constructing $M = K/\alpha - 1$ surrogates, so that, with the original series, there are K/α series. If the series of the measured data belongs to the K smallest or largest values, the null hyphotesis can be rejected with a significance of α. In two-sided tests, $M = 2K/\alpha - 1$, resulting in a probability α that the data gives either one of the K smallest or largest values. In the present work surrogate series will not be used to test an hypothesis about the character of the studied series, but to look for the *relative* difference of the entropies with those of a process of independent random variables. In this way surrogates will serve the purpose of selecting the most important blocks of a series, acting as an additional criterium facing the unknown variances of higher-order entropies.

Hence, the standard definition of significance in terms of the deviation with respect to the variance will be used, without attempting to interprete the results assuming Gaussian-distributed surrogates (section 3.4.3).

Chapter 2

The Southern Oscillation: Interannual variability of the tropical Pacific

The most important mode of variability in the tropical Pacific is known as El Niño and the Southern Oscillation [115]. In this light, it is hard to imagine that El Niño was discovered by Peruvian sailors as a warm ocean current from the north, which became its name (the Child Jesus) since it appeared shortly after Christmas. As this term is now commonly related to devastating droughts over the western tropical Pacific, torrential floods over the eastern tropical Pacific, and unusual weather patterns over various parts of the world, the view of it has become pejorative. Nevertheless El Niño is a phase of an extremely interesting natural oscillation known as the *Southern Oscillation* [84]. Episodes of El Niño repeat irregularly after being separated by periods where oceanic and atmospheric conditions are benign and opposite to those of El Niño. The term La Niña (the girl) is used for these opposite phases of the Southern Oscillation, when sea surface temperature in the central

and eastern tropical Pacific are unusually low and when the trade winds are very intense. The physics and the general problematic of El Niño and the Southern Oscillation will be addressed in some detail in this chapter.

2.1 El Niño and the Southern Oscillation

The first scientific mention of El Niño occured in the Sixth International Geographical Conference in Lima, Peru, in 1895. This was the place where the oceanic current observed by the Peruvian sailors which "converted the desert in a garden" [71] was discussed for the first time. Afterwards, Hildebrandsson [45] published in 1897 his findings about a phase difference in the fluctuations of the atmospheric pressure between Australia and Argentina, and Lockyer [63], [64] calculated the period of a pressure oscillation between the eastern Indian Ocean and the eastern Pacific. This was the information Sir Gilbert Walker had as he became Director-General of Observatories in India in 1904 and continued a research concerned with the failure of the monsoons in 1877 and 1899 and the catastrophic famines that occured. His work was the milestone of a large investigation of a phenomenon which has not finished surprising scientists [84].

The Southern Oscillation is a term introduced in the series of papers published by Walker and coworkers between 1923 and 1937, denoting the pressure fluctuations between the equatorial extremes of the tropical Pacific [122] - [123]. To avoid confusion with the North Atlantic Oscillation and the North Pacific Oscillation, he coined this term and described it as "when pressure is high in the Pacific Ocean it tends to be low in the Indian Ocean from Africa to Australia". He established moreover many correlations between it and rainfall patterns and wind fields over the tropical Pacific and Indian Oceans, and with temperature fluctuations in southeastern Africa and southwestern North America. Unfortunately, his work was neglected in the following decades because of

the unsolved difficulties in predicting the monsoons. There was seemingly not enough interest in the South American climatology to note that during the Indian food shortages of 1877 and 1899 the Peruvian desert blossomed under the effect of El Niño.

It was not until 1957 and 1958, when during the International Geophysical Year, both the atmospheric and oceanographic conditions were remarkably anomalous, and the Southern Oscillation became interesting again. The coast of Peru experienced an extraordinary fertility and warm waters extended offshore to the date line in the Pacific. At the same time, weak winds and heavy rainfall coincided in the central equatorial Pacific, a normally arid region. The normal conditions of the atmospheric pressure, sea surface temperature and winds were perturbed by El Niño, which was understood as an extreme state of the Southern Oscillation. Since then these phenomena are denoted as ENSO. It was J. Bjerknes from the University of California who postulated correctly that these meteorological and oceanographical variations were not unique but occur interannualy and gave a physical explanation for them [13]. This is based on that in a normal state, dry air sinks over the cold water of the eastern tropical Pacific and flows westward along the equator as a part of the easterly (westward) trade winds. The air is warmed and moistened as it moves over the progressively warmer water until it reaches the western tropical Pacific, where it rises in towering rain clouds. A return flow in the upper troposphere closes this air cycle, which Bjerknes called Walker Circulation. He proposed that the sea surface temperature gradients — the cold water off Peru and the warm water in the western tropical Pacific — are necessary for the atmospheric pressure gradients that drive the Walker Circulation. In El Niño, a warming of the eastern tropical Pacific weakens the Walker Circulation and causes the convective zone of heavy rainfall to move eastward to the central and eastern tropical Pacific. In other words, the Southern Oscillation is caused by the interannual *sea surface temperature variations* of the tropical Pacific.

From an oceanographic point of view, however, sea surface temperature changes are caused by the *surface wind fluctuations* associated with the Southern Oscillation. Combining these circular arguments, Bjerknes inferred that interactions between the ocean and atmosphere determine the mechanism of the Southern Oscillation. It was possible for him to explain the development of El Niño as a consequence of a slight relaxation in the winds which causes a warming of the eastern Pacific and its gradual amplification since this weakens in turn the trade winds. The opposite is also valid for La Niña. It remained nevertheless uncertain how the turnabout from a warm to a cold phase and viceversa occur. This question has been solved with the construction of coupled models of the atmosphere and oceans. Studies with models reveal that the interactions can support modes of oscillation that are strictly originated on the coupled ocean-atmosphere system. There are many possible modes and some of them are interannual fluctuations between warm El Niño and cold La Niña conditions and hence correspond to possible Southern Oscillations.

The stability of the low-frequency variability in the tropical oceans, due to its cause in the fluctuations in the winds have open the doors for the General Circulation Models (GCMs). This is a fortunate situation is contrasting to the subtropical gyres of the ocean, especially the neighborhood of intense currents such as the Gulf Stream, where variability is attributable primarily to instabilities of the mean currents. In these cases, the instabilities are chaotic and amplify perturbations and errors in the initial conditions. Since this is not the case for the tropical waters, it is possible to specify the basic density field of the ocean and the driving force of the winds. GCMs solve the nonlinear primitive equations of motion numerically and have been already of utility in predicting El Niño in the last decade. Many important experiments performed with GCMs are given in the references [85] and [67]; joint projects have been realized to compare the results obtained with coupled GCMs [59], [1]. Though reasonable realistic, General Circulation Models are

are from perfect. Inaccurate forcing functions and an inadequate parameterization are the most frequent flaws in them. Especially for the latter problem remain simpler ocean-atmosphere models extremely important, allowing the study of the role of specific physical processes and the investigation of the parameters involved in variuos phenomena. It is expected in the light of comparisons between numerical experiments and observations that an improved parametrization will contribute to improved simulations. The discrepancies between the models and reality surprise regularly the scientific community, a fact that shows that statistical and information-theoretical methods are still needed.

2.1.1 Development of El Niño

It is not possible to establish a definite development pattern of El Niño, for this has evolved in different manners, especially in the last decades. For many of El Niño episodes, however, there is a standard description, which repesents the typical evolution towards warm states, without dependence of their intensity. This process is called the composite El Niño in an analysis by Rasmusson and Carpenter [91], as was found with six episodes between 1950 and 1976. Here it is illustrated in figure 2.1 with the small event which occured in 2002-2003.

Onset of El Niño in the eastern Pacific

Towards the end of the year preceding a warm event, this will be called the year (-1), the sea level pressure in the central and eastern tropical Pacific starts to decrease, and the trade winds from the east weaken to the west of the date line, where sea surface temperature becomes higher than normal. None of these changes is a reliable precursor of El Niño; similar changes can occur

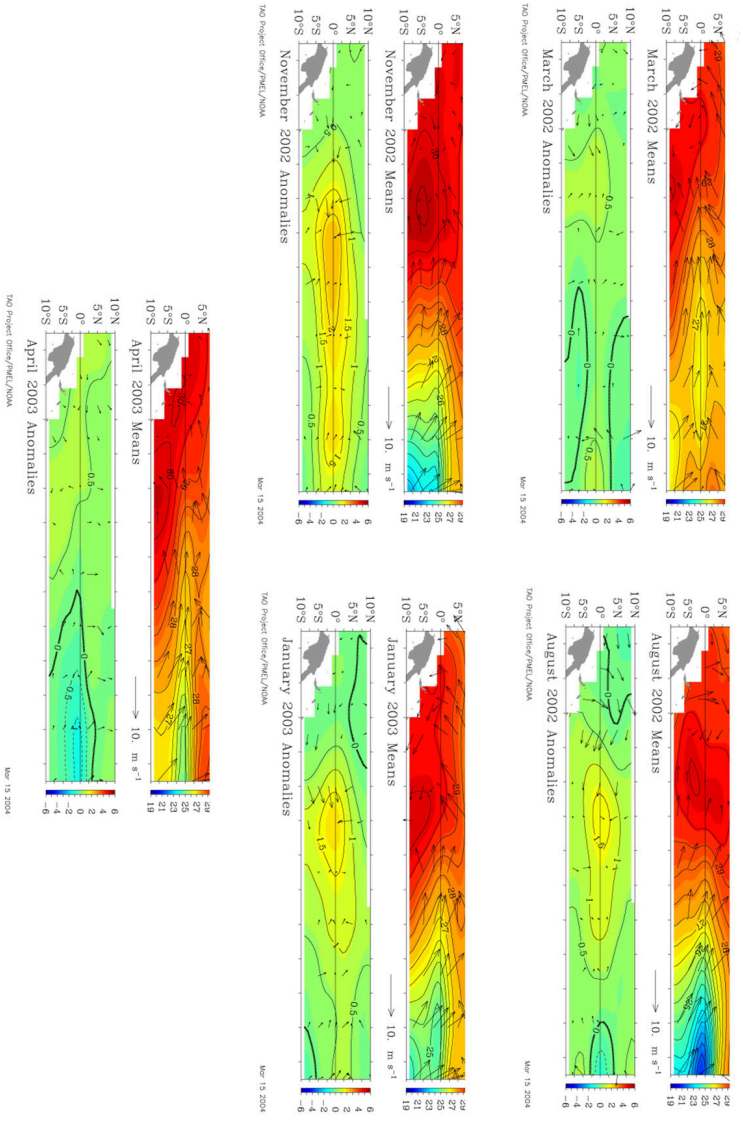

Figure 2.1: Sea surface temperature anomalies (in °C) during a composite El Niño from the TAO/TRITON dataset.

when no El Niño is imminent. However in a composite El Niño, the warm phase of the seasonal cycle in the eastern tropical Pacific is amplified during

the early calender months of year (0), so that surface temperatures and rainfall in the east attain exceptionally high values at the time of the seasonal maxima. This conditions persist in the east for several months and the Intertropical Convergence Zone (ITCZ), responsible for the precipitation, is inhibited from its seasonal movement to the north. Anomalous rainfall, for instance, on the Galapagos Islands (near 90°W) has its maximum in March, April and May of year (0). But not only the movement of the ITCZ is inhibited, also the usual westward propagation of the cool phase of the seasonal cycle. The persistence of high sea surface temperatures therefore implies that the positive sea surface temperature anomalies, relative to the climatology, propagate westward. On the basis of data along the coast of Peru, knowing the speed of the propagation, is possible to estimate when, in the central equatorial Pacific, the cold season will fail to develop and the warm surface waters will persist for several months [9].

Onset of El Niño in the western and central Pacific

While warm, wet conditions prevail in the eastern equatorial Pacific, the convective zone over the western Pacific does not start moving until April of year (0), so that rainfall decreases and sea level pressure increases over Indonesia. Farther east, near Nauru (165°E) to the South American coast, there is now heavy rainfall and northerly wind anomalies are indicative of a southward displacement of the ITCZ. By July of year (0), anomalous conditions in the eastern equatorial Pacific have peaked, although a secondary maximum can appear late in January and early in year (+1). These developments in the east are different from those in the western and central Pacific, where anomalous conditions continue to amplify until the end of year (0). Rainfall at the Line Islands (near 157°W), for example, has its strongest enhancement towards the end of year (0). Figure 2.1 indicates that not only rainfall but

also sea surface temperature anomalies attain a maximum amplitude along the coast of Peru, long before they do so in the central Pacific.

Mature El Niño and onset of La Niña

The eastward movement of the convergence zone that is normally over the western equatorial Pacific, the equatorward displacement of the ITCZ, and the northward movement of the South Pacific Convergence Zone are associated with the collapse of the easterly trade winds so that westerly winds extend to 160°E by September of year (0). Farther west, over Indonesia, for example, negative rainfall anomalies peak between June and September of year (0). Eastern New Guinea, which is between drought-striken Indonesia and the region of heavy rainfall in the central equatorial Pacific, has a weak and inconsistent precipitation anomaly pattern. The large anomalies attain the maximum areal extent towards the end of year (0) and early year (1), the mature phase of El Niño, as shown in figure 2.1. Tropospheric temperatures are now above normal throughout the tropics and the anticiclonic couplet over the region of enhanced precipitation is associated with a teleconnection pattern to higher latitudes. A precursor of the end of El Niño is the appearance of cold surface waters in the eastern equatorial Pacific towards middle of year (+1). These low sea surface temperature spread westward and inaugurate La Niña. The duration of a composite El Niño is of the order of 18 months.

2.2 The physics of El Niño

A realistic description of the Pacific basin makes it necessary to employ spherical coordinates for the representation of the equations of motion while ignoring the departures of the form of the earth from sphericity. This procedure allows to attain important properties of the ocean, as equatorial upwelling

and the existence of a lower density layer at its surface, albeit involving complex scaling considerations and some less enlightening mathematics. Hence, the scope of this section will be limited to the so-called geostrophic approximation, which corresponds to the condition of oceanic dimensions which are much smaller than the radius of the Earth. This condition implies in practice the observation of the flat geometry at a tangent plane of the Earth under a constant Coriolis parameter. Though very simplified, this approach will be useful to introduce the oceanic waves with major influence on El Niõ and on the overall geophysics at planetary scales.

For incompressible fluids in the geostrophic approximation, the continuity equation

$$\frac{\partial \rho}{\partial t} + \nabla \cdot \rho \boldsymbol{u} = 0 \tag{2.1}$$

reduces to the condition

$$\frac{\partial u}{\partial x} + \frac{\partial v}{\partial y} + \frac{\partial w}{\partial z} = 0 \tag{2.2}$$

where x and y are the horizontal coordinates of longitude and latitude and z the vertical coordinate perpendicular to the Earth surface. In a nonrotating frame of reference, the momentum equation for the fluid system takes further the form

$$\rho \left(\frac{\partial}{\partial t} + \boldsymbol{v} \cdot \nabla \right) \boldsymbol{v} = -\nabla p + \rho \nabla \phi + \Im \tag{2.3}$$

where $\boldsymbol{v} = u\hat{\boldsymbol{i}} + v\hat{\boldsymbol{j}} + w\hat{\boldsymbol{k}}$ is the velocity of an element of fluid, ρ its density, p is the pressure, ϕ a potential of conservative forces and $\Im$ represent dissipative forces in general. This equation can be written for the rotating coordinate frame of the earth with the Coriolis parameter $f = \beta y$ (where $\beta = 2\Omega/a$, with Ω the rate of rotation of the earth and a its radius) in its components as

$$\begin{aligned}
\frac{\partial u}{\partial t}+\left[u\frac{\partial u}{\partial x}+v\frac{\partial u}{\partial y}+w\frac{\partial u}{\partial z}\right]-fv =& \frac{-1}{\rho}\frac{\partial p}{\partial x}+\frac{\partial \phi}{\partial x}+\Im_x \\
\frac{\partial v}{\partial t}+\left[u\frac{\partial v}{\partial x}+v\frac{\partial v}{\partial y}+w\frac{\partial v}{\partial z}\right]+fu =& \frac{-1}{\rho}\frac{\partial p}{\partial y}+\frac{\partial \phi}{\partial y}+\Im_y \\
\frac{\partial w}{\partial t}+\left[u\frac{\partial w}{\partial x}+v\frac{\partial w}{\partial y}+w\frac{\partial w}{\partial z}\right] =& \frac{-1}{\rho}\frac{\partial p}{\partial w}+\frac{\partial \phi}{\partial z}+\Im_z
\end{aligned} \tag{2.4}$$

if the dependence of the dissipative forces $\Im$ in the velocity field is invariant with respect to the change of the reference frame. In this case x and y become the *zonal* and *meridional* coordinates. This is the case for many realistic dissipative forces as those to be included in this analysis.

To simulate the simplest structure of the ocean, one can introduce the *shallow water model*. There are several aspects of the ocean, as its stratification and the salinity, which can be important, but for the purposes of this introductory chapter will be neglected. To take into account these processes, approaches developed in [30, 34] are recommended. The model consists of two immiscible layers of fuid, each of constant density, whose interface simulates the sharp and shallow region of maximum thermal gradients that separates the warm waters of the surface from the deeper colder waters. This region is known as the *thermocline* and in absence of warm or cold events of the Southern Oscillation, it is shallow in the estern tropical Pacific and deepents to the west. The upper ocean layer has density ρ_1, a mean depth $H_0(x, y)$, and is bounded above by a rigid lid. The lower layer has density ρ_2 and is infinitely deep so that it must be motionless for the kinetic energy to be finite. (In reality the ocean is 4000 m deep and the mean spatial depth of the thermocline is of approximately 100 m.) The dynamics of the ocean and the propagation of waves will be given by studying small perturbations η in the depth of the thermocline, for which a Cartesian coordinate system is fixed, which rotates with the earth (figure 2.2). This is known as the equatorial $\beta-$plane and its z

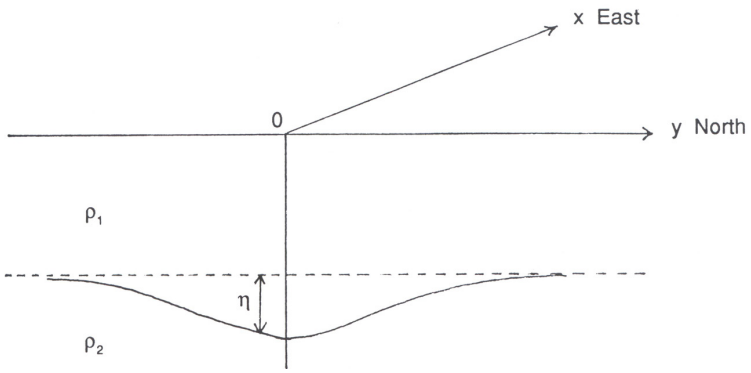

Figure 2.2: The cartesian coordinate system for the shallow-water model.

axis will be centered at the depth H_0, running in the positive direction towards the bottom of the ocean.

In the hidrostatic approximation the pressure at the depth z is given by

$$p = \rho g z + p_0, \tag{2.5}$$

where p_0 is the atmospheric pressure at sea level, so that the gravitational acceleration at the interface will be

$$g' = \frac{\rho_2 - \rho_1}{\rho_1} g. \tag{2.6}$$

As the conservative forces are due to the horizontal winds, it is possible to express them in terms of the wind stress τ along the sea surface, which is the wind force exerted per unit density and area of the ocean, divided into the height of its upper layer: τ^x/H_0 and τ^y/H_0 for the zonal and meridional coordinates respectively. The dissipative forces can be introduced with a Rayleigh damping acting isotropically in the horizontal directions so that $\Im_x = -au$ and $\Im_y = -av$. Finally, it should be noted that with all these forces, all accelerations given by equation (2.4) are independent of z. It is therefore consistent

to assume that the horizontal velocities themselves remain z-independent if they are so initially. This is the case for this system as is confirmed by the Taylor-Proudman theorem [108]. Hence, the horizontal momentum equations become

$$\begin{aligned} \frac{\partial u}{\partial t} + u\frac{\partial u}{\partial x} + v\frac{\partial u}{\partial y} - fv + g'\frac{\partial z}{\partial x} &= -au + \tau^x/H_0 \\ \frac{\partial v}{\partial t} + u\frac{\partial v}{\partial x} + v\frac{\partial v}{\partial y} + fx + g'\frac{\partial z}{\partial y} &= -av + \tau^y/H_0 \end{aligned} \tag{2.7}$$

and the conservation of the mass (2.2) can be integrated in z to yield

$$w(x, y, z, t) = -z\left(\frac{\partial u}{\partial x} + \frac{\partial v}{\partial y}\right) + w_0(x, y, t). \tag{2.8}$$

Applying the boundary condition of a rigid upper surface, this leads to the equation of conservation of mass for any depth H

$$\frac{\partial H}{\partial t} + \frac{\partial}{\partial x}(uH) + \frac{\partial}{\partial y}(vH) = 0. \tag{2.9}$$

The shallow-water model is given by equations (2.7) and (2.9). With the set of assumptions of this model, it has been possible to reduce the number of dynamical equations and by one, by eliminating w explicitly from the dynamics, the number of dependent variables.

2.2.1 A simple model of the ocean

It is interesting to search for oscillating solutions to these equations, for they can explain the propagation of pulses throughout the surface of the ocean. For an analytic treatment, it is useful to consider first the undamped and unforced system. Small amplitude motions of the thermocline can be represented by

its vertical deviation from the mean height of the interface $H_0(x, y)$ so that $H(x, y, t) = H_0(x, y) + \eta(x, y, t)$. The condition that the amplitude is small implies that $\eta \ll H$. Further, we suppose that u and v are small enough that

$$\frac{\partial \boldsymbol{v}}{\partial t} \gg \boldsymbol{v} \cdot \nabla \boldsymbol{v}. \tag{2.10}$$

Then the linearized shallow-water equations without forcing, which ignore all quadratic terms in the dynamical variables u, v and η, are:

$$\begin{aligned} \frac{\partial u}{\partial t} - fv &= -g' \frac{\partial \eta}{\partial x}, \\ \frac{\partial v}{\partial t} + fu &= -g' \frac{\partial \eta}{\partial y}, \\ \frac{\partial \eta}{\partial t} + H_0 \frac{\partial u}{\partial x} + H_0 \frac{\partial v}{\partial y} &= 0. \end{aligned} \tag{2.11}$$

Manipulating the first two equations one gets a single equation in η [81]. This equation is

$$\frac{\partial}{\partial t} \left[\left(\frac{\partial^2}{\partial^2 t^2} + f^2 \right) \eta - \nabla \cdot (c^2 \nabla \eta) \right] - g' f J(H_0, \eta) = 0. \tag{2.12}$$

where

$$c^2 = g' H_0 \tag{2.13}$$

and $J(H_0, \eta)$ is the Jacobian operator over the two functions.

It is possible to derive some important kinds of waves which are present in the ocean and atmosphere by considering the following model: Let a channel be bounded at the latitudes $y = 0$ and $y = Y$, in which the depth of the upper water layer $H_0(x, y)$ does not depend on x and reaches its highest level H_{max} at $y = 0$ and its lowest level at $y = Y$,

$$H_0 = H_{max} \left(1 - \frac{y}{Y} \right). \tag{2.14}$$

In the geostrophic approximation $f \neq 0$ since the plane is centered at $y > 0$. Even though this substitution does not pretend to be a realistic representation of the ocean (equatorial upwelling would make this geometry impossible), it leads to oscillating solutions of equation 2.12 which share the properties of large-scale oceanic waves. (The origin of these waves lies rather in wind stress disturbances). To derive them, the channel can be imagined with $y = 0$ at the equator and northward increasing y. Then, oscillations of the form

$$\eta = \mathrm{Re}\left(\bar{\eta}(y)\right)\, e^{i(kx-\sigma t)} \tag{2.15}$$

may be sought, where $\bar{\eta}$ is the complex wave amplitude which varies with the cross-channel coordinate y. Thus, the eigenvalue problem for $\bar{\eta}(y)$ is

$$\left(1-\frac{y}{Y}\right)\frac{d^2\bar{\eta}}{dy^2} - \frac{1}{Y}\frac{d\bar{\eta}}{dy} + \bar{\eta}\left[\frac{\sigma^2-f^2}{gH_{max}} - k^2\left(1-\frac{y}{Y}\right) - \frac{f}{Y\sigma}k\right] = 0, \tag{2.16}$$

with the boundary conditions in $y = 0$ and $y = Y$

$$\frac{d\bar{\eta}}{dy} + \frac{fk}{\sigma}\bar{\eta} = 0. \tag{2.17}$$

Since y/L is never larger than one, a good approximation to equation 2.16 is

$$\frac{d^2\bar{\eta}}{dy^2} - \frac{1}{Y}\frac{d\bar{\eta}}{dy} + \bar{\eta}\left[\frac{\sigma^2-f^2}{c^2} - k^2 - \frac{f}{Y}\frac{1}{\sigma}k\right] = 0. \tag{2.18}$$

The solution for this equation, where only quantities known to be of order unity have been neglected, is, with complex $\bar{C}$

$$\bar{\eta} = \bar{C}e^{y/Y}e^{i\alpha y} \tag{2.19}$$

with the coefficient

$$\alpha = \frac{\sigma^2 - f^2}{c^2} - \left(k^2 + \frac{1^2}{4Y^2}\right) - \frac{f}{\sigma}\frac{k}{Y}. \tag{2.20}$$

Applying equation 2.16 the eigenvalue relation

$$(\sigma^2 - f^2)(\sigma^2 - k^2c^2)\sin\alpha Y = 0, \tag{2.21}$$

is found, which can be solved to look for oscillatory behavior. It is not difficult to show that the factor $\sigma^2 = f^2$ is a spurious root. The other two factors allow the following geophysical waves.

2.2.2 Kelvin and Rossby waves

- The condition $\sigma = \pm ck$ in equation (2.21) corresponds to a dispersion relation for a wave whose crests are parallel to the y-axis for a non-rotating fluid. This wave is known as the *Kelvin wave*. Taking the positive sign for c, it follows that the dynamical fields can be written in the form

$$\eta = \eta_0 e^{-fy/c} e^{i(kx - \sigma t + \phi)} \tag{2.22}$$

$$u = \frac{\eta_0 c}{H_{max}} e^{-fy/c} e^{(kx - \sigma t + \phi)} \tag{2.23}$$

$$v = 0, \tag{2.24}$$

  so that, as eqs. (2.11) show, u is in geostrophic balance with the pressure field:

$$\frac{\partial u}{\partial t} = -g'\frac{\partial \eta}{\partial x} \tag{2.25}$$

$$\frac{\partial \eta}{\partial t} = -H_{max}\frac{\partial u}{\partial x}. \tag{2.26}$$

With these results, eqs. (2.11) are reduced readily to

$$\frac{\partial^2 u}{\partial t^2} - c^2 \frac{\partial^2 u}{\partial x^2} = 0 \tag{2.27}$$

$$f\frac{\partial u}{\partial t} - c^2 \frac{\partial^2 u}{\partial x \partial y} = 0, \tag{2.28}$$

revealing that Kelvin waves with a negative c are not bounded in y, so that, from the sign of σ, only eastward waves are possible. It can be derived from equations (2.26) the Kelvin wave satisfies the classical wave equation

$$\frac{\partial^2 \eta}{\partial t^2} = c^2 \frac{\partial^2 \eta}{\partial x^2} \tag{2.29}$$

a fact that lets interpret c as the phase velocity of the Kelvin wave. The latitudinal distance $\lambda = (c/\beta)^{1/2}$ is called the *equatorial radius of deformation*. This is the distance over which the gravitational tendency to render the free surface flat is balanced by the tendency of the Coriolis acceleration to deform the surface, as can be observed from equation (2.22).

- The condition $\sin \alpha Y = 0$ in equation (2.21) yields the dispersion relation

$$\sigma^2 - c^2 \left(\frac{fk}{Y\sigma} + k^2 + n^2 + \frac{f^2}{c^2} \right) = 0 \tag{2.30}$$

for $n = \pi^2/Y^2, 2\pi^2/Y^2, \ldots$. The solutions to this equation can be separated according to their frequency. If σ exceeds f, the term in Y is negligible and waves of higher frequency than the rotation of the earth emerge. These waves are called Poincaré waves and due to their high frequency will not be of importance in our analysis. The third root of the cubic equation (2.30) corresponds to the following dispersion relation,

$$\sigma = -\frac{\beta k}{k^2 + n^2 + f_0^2/c^2}, \tag{2.31}$$

where the inertial frequency f_0 at the boundary Y has been introduced. This equation characterizes the elementary *Rossby wave*, which requires f to be nonzero, which means that it cannot be excited along the equator.

As the frequency σ is by definition positive, it is required that the wave number k be negative and consequently all Rossby waves have westward phase propagation. An analysis [35] of this dispersion relation shows, however, that the group velocity of the waves can be either westward or eastward. Waves with zero group velocity have the highest possible frequency $\beta c/2f_0$, so that Rossby waves of this frequency can propagate only equatorward of the latitude where the Coriolis parameter is $f_0 = \beta y_0$. The waves with eastward group velocity are short and dispersive, while the westward waves are long and nondispersive and propagate with a group velocity

$$s = -\beta c^2/f_0^2. \tag{2.32}$$

The superposition of a wave that propagates towards its northern turning latitude y_0 and another wave with the same frequency and wave number that propagates to the south results under certain conditions in a standing latitudinal mode. These waves are called *equatorially trapped waves* and their modes are possible for certain discrete values of the meridional wave number n obtained from the boundary conditions. Manipulating the shallow-water equations to separate the meridional velocity v, and introducing the substitution

$$v = V(y)e^{i(kx-\sigma t)}, \tag{2.33}$$

the eigenvalue problem for v becomes

$$\frac{\partial^2 V}{\partial y^2} + \frac{\beta^2}{c^2}(Y_0^2 - y^2)V = 0 \tag{2.34}$$

where

$$Y_0^2 = \left(\frac{\sigma^2}{c^2} - k^2 - \frac{\beta k}{\sigma}\right)\frac{c^2}{\beta^2}. \tag{2.35}$$

This equation has solutions which are oscillatory in an equatorial zone of width $2Y_0$ but are exponentially decaying poleward of the latitudes $\pm Y_0$. The equatorially trapped waves are allowed if the condition

$$\frac{c}{\beta}\left(\frac{\sigma^2}{c^2} - k^2 - \frac{\beta k}{\sigma}\right) = 2n + 1, \tag{2.36}$$

with $n = 0, 1, 2, \ldots$ is fulfilled. The structure of this waves is given by the eigenfunctions of equation (2.34), which are the Hermite functions

$$D_n = e^{-\xi^2/2} H_n(\xi), \qquad \xi = y/\lambda \tag{2.37}$$

where H_n is the nth Hermite polynomial, so that, differently to the Kelvin waves

$$v = D_n(y/\lambda)\exp i(kx - \sigma t) \tag{2.38}$$

$$u = i(2\beta)^{1/2}\exp i(kx - \sigma t)\left[\frac{n^{1/2}D_{n-1}}{\sigma + ck} + \frac{(n+1)^{1/2}D_{n+1}}{\sigma - ck}\right] \tag{2.39}$$

$$\eta = -(2\beta)^{1/2}\exp i(kx - \sigma t)\left[\frac{n^{1/2}D_{n-1}}{\sigma + ck} - \frac{(n+1)^{1/2}D_{n+1}}{\sigma - ck}\right] \tag{2.40}$$

At low frequencies, the dispersion relation of these waves simplifies to

$$\sigma = \frac{-\beta k}{k^2 + \frac{2n+1}{\lambda^2}}, \tag{2.41}$$

a fact that reveals that these modes are very similar to the Rossby waves of equation (2.31), with westward propagation for long and nondispersive waves with a group velocity which attains the value $c/(2n+1)$. This velocity corresponds to a traveling time around fifty days for the gravest Rossby mode through the whole length of the Pacific, while a Kelvin wave needs twice this time. Free and trapped westward Rossby waves are of paramount importance in the oceanic adjustment to a change in the winds. It is beyond the scope of this introduction to the dynamics of the Southern Oscillation to show that westward Rossby waves reflect to the east as Kelvin waves and eastward Kelvin waves reflect to the west as Rossby waves. This is nevertheless an important fact that accounts for the sustained oscillations from El Niño to La Niña and back. An initially bell-shaped thermocline displacement disperses into an eastward propagating Kelvin wave and westward propagating Rossby waves, as found in numerical experiments by Philander and coworkers [86] shown in figure 2.3.

2.2.3 A simple model of the atmosphere

A minimal model of the atmosphere, due to its compresibility and continuous stratification, is much more difficult to construct than a model of the ocean. Hence we will restrict to investigate the surface stress exerted by the winds in the boundary layer of the atmosphere with the ocean responding to a given heat source. This is the most important process from an atmospheric point of view in the interactions between the ocean and atmosphere.

Let the wind transport at the boundary layer be defined as

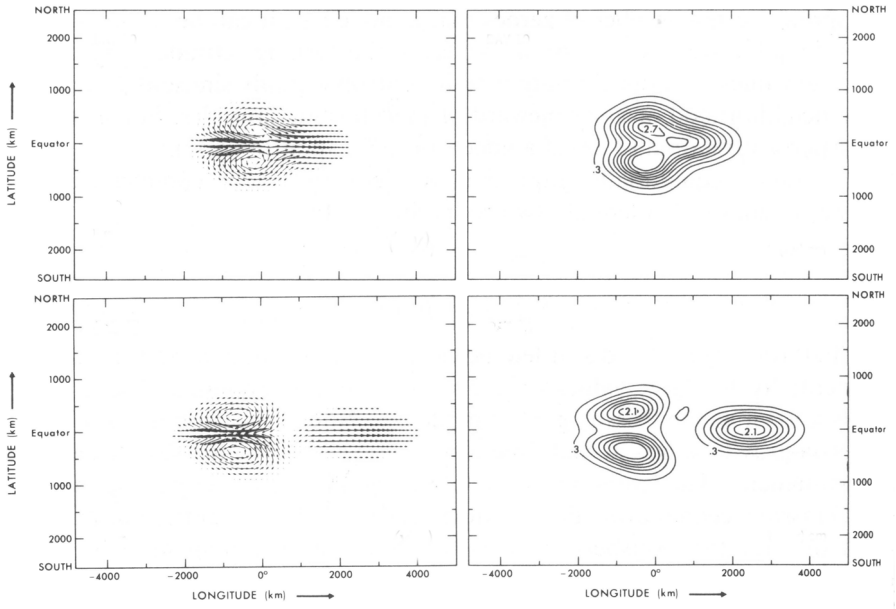

Figure 2.3: The dispersion of an initially bell-shaped thermocline displacement into an equatorial Kelvin wave and two off-equatorial Rossby waves. The left-hand panels show the horizontal currents ad the right-hand panels the thermocline displacements. Adapted from Philander *et. al.* [86]

$$U = \int_{p_S}^{p_T} u dp/g \qquad V = \int_{p_S}^{p_T} v dp/g \tag{2.42}$$

where p_S is the pressure at the surface and p_T is that at the top of the boundary layer. With the simplest parametrization of the surface stress of the winds $\boldsymbol{\tau}$ as proportional to the mass transport of the boundary layer

$$\boldsymbol{\tau} = A(U, V) \tag{2.43}$$

it is possible to express the linear momentum equations and the equation for the conservation of mass, integrated vertically as in equation (2.42) as

$$
\begin{aligned}
AU - fV + \frac{\partial \varphi}{\partial x} &= 0 \\
AV + fU + \frac{\partial \varphi}{\partial y} &= 0 \\
\omega + \frac{\partial U}{\partial x} + \frac{\partial V}{\partial y} &= 0,
\end{aligned} \tag{2.44}
$$

where φ is the geopotential and ω the vertical flux. Differently to the behavior in midlatitudes, where horizontal temperature gradients are large and a steady heat source can be balanced by the horizontal advection of colder air towards the source, in the tropics the horizontal temperature gradients are small and a heat source gives rise to strong upward motion of air. This allows to establish a balance between the heating and adiabatic cooling as a consequence of the vertical motion, so that if the rate of heating per unit mass is Q and the vertical velocity w,

$$
w = Q/HN^2 \tag{2.45}
$$

where H is the characteristic height of the heated air layer and $N =$ is the Brunt-Väisälä frequency associated to the restoring force exerted over a fluid of different density than that of the air at its surroundings at some height. Assuming that the heating is proportional to the precipitation P and that the radiative cooling is proportional to φ, it is possible to write the vertical equation in (2.44) as

$$
B\varphi + c_A^2 \left(\frac{\partial U}{\partial x} + \frac{\partial V}{\partial y} \right) = -aP, \tag{2.46}
$$

where a s a constant, B can be interpreted as a coefficient for Newtonian cooling and c_A is a measure of the static stability of the atmosphere, determining the Brunt-Väisälä frequency.

This very simple model allows to examinate the effect of a forcing with the latitudinal structure of the precipitation

$$P = (1 - y/Y)e^{(-y^2/4Y^2)} \tag{2.47}$$

confined to a band of longitude 20° wide and $L = 10°$ latitude [34]. The field of low-level winds obtained is shown in figure 2.4, where convergence onto the heated region and cyclonic vorticity due to the rising motion are evident. The highest velocities of the wind take place at the center of the forcing and are asymetric in the x axis as strong westerly winds feed principally the vortex. There are many crude assumptions in this model, especially those for the dissipative term in B. Hence, it is reassuring that certain aspects of the response are insensitive to the value assigned [73].

2.2.4 A model of the Southern Oscillation

A very simple coupled model to explore interactions between the ocean and atmosphere has as its meteorological component the model discusse above, which provides a reasonably accurate representation of the surface winds in response to a specified heat source. The oceanographic component is the shallow-water model of equations (2.7) and (2.9), which give an acceptable description of the changes in the depth of the thermocline in response to the wind stresses. These models of the ocean and atmosphere can be coupled by driving the ocean with the winds from the atmospheric model as proportional to the transport,

$$(\tau^x, \tau^y) = \gamma(U, V) \tag{2.48}$$

and by relating the atmospheric heat source Q to the state of the ocean. The

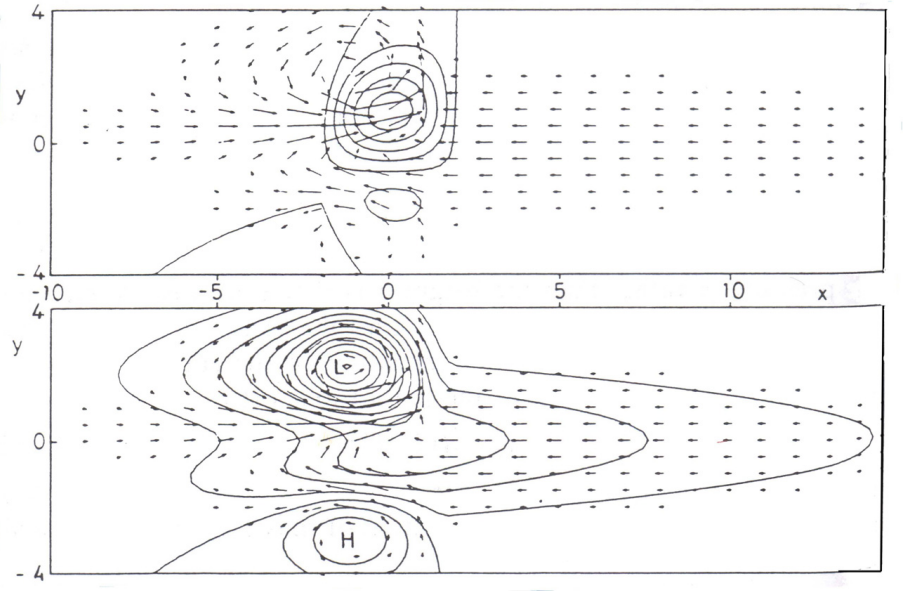

Figure 2.4: The low-level winds, shown as arrows, in response to a heat surce with exponential meridional decay. The heating is confined to a band of longitude 20° wide centered on $x = 0$. The contours in the upper panel show the vertical velocity and in the lower panel the pressure. The unit of distance is te radius of deformation λ, which is 10°. Adapted from Gill [34].

heat source can be assumed to depend linearly on the sea surface temperature anomaly T,

$$Q = \alpha T. \tag{2.49}$$

It is now necessary to relate T to the oceanic variables. The simplest assumptions to explore are the substitutions

$$T = s\eta, \tag{2.50}$$

$$\frac{\partial T}{\partial t} + u\frac{\partial \bar{T}}{\partial x} = -rT. \tag{2.51}$$

Equation (2.50) exploits the high correlation between the sea surface temperature T and the depth of the thermocline η in certain parts of the tropics. This is a reasonable hypothesis, since a large thermocline anomaly represents a larger volume of warm waters on the upper oceanic layer, as can be seen in figure 2.2. Advection is included implicitly in this case because changes in the depth of the thermocline are attributable to a horizontal redistribution of warm surface waters. In equation (2.51), advection of the mean temperature gradient along the equator and newtonian cooling are explicitly the main mechanisms of heating. Specified are the zonal gradient of the mean temperature $\partial\bar{T}/\partial x$, which is generally negative, and the constants s and r.

It is possible to perform a stability analysis introducing perturbations of the form $\exp i(kx - \sigma t)$, where σ is complex so that the growth rate (the imaginary part of σ times -1) and the frequency (its real part) depend on the zonal wave number k. There are two different scenarios depending on the coupling mechanism between the ocean dynamics and its temperature, equation (2.50) or (2.51). In the case of a dependence of the sea surface temperature on the thermocline anomaly, in the absence of coupling between the ocean and atmosphere ($\alpha = \gamma = 0$), the modes are Kelvin and equatorially trapped Rossby waves as those of figure 2.3, except that they are damped. As the coupling coefficients increase, the eastward Kelvin waves become less damped and eventually unstable, while the westward Rossby waves remain damped. This happens since the winds to the east tend to be more intense and have a larger zonal extent than the winds to the west, as a response to an oceanic heating (figure 2.4), so that they coincide with the perturbation

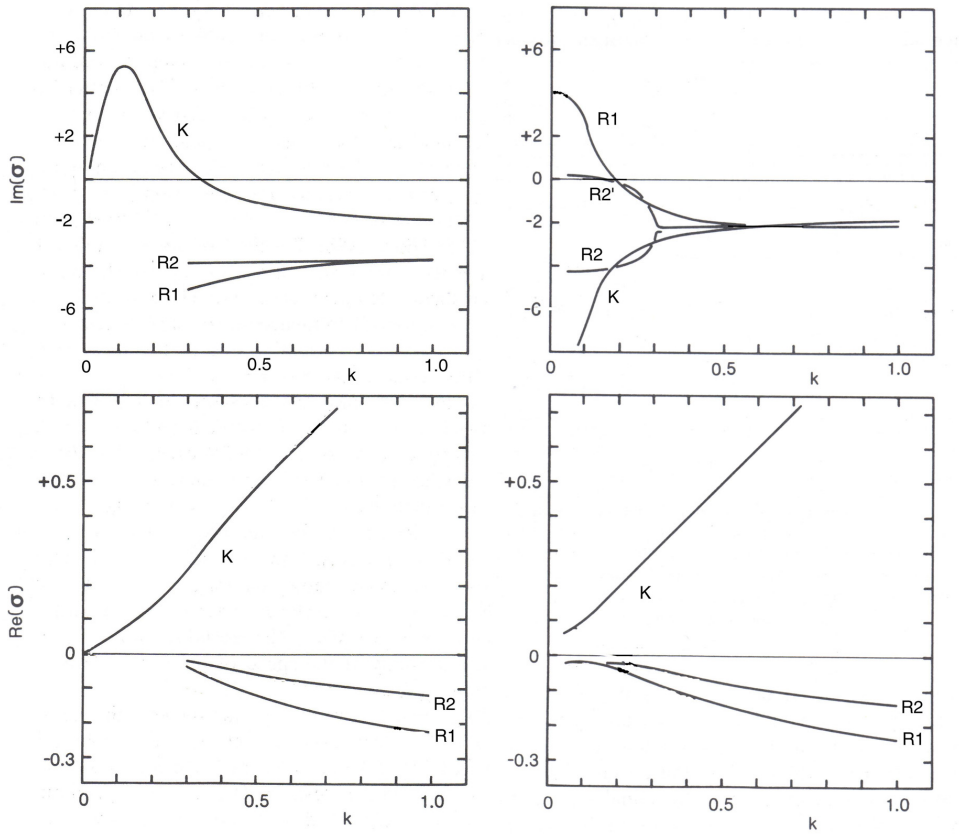

Figure 2.5: The growth rate ($\mathrm{Im}(\sigma)$) and frequency ($\mathrm{Re}(\sigma)$) of unstable modes, as a function of wave number k in the x direction. The upper panels are derived from a model in which atmospheric heating is proportional to the depth of the thermocline (eq. (2.50)). The lower panels correspond to the case in which the atmospheric heating and sea surface temperature depend on advection (eq. (2.51)).

on thermocline traveling eastward due to the Kelvin wave. The growth factor and frequency of these waves in dependence of the wave number k is shown in the left panels of figure 2.5. The most unstable of these possible modes has a

wavelength near $16,000$ km and an e-folding time of the order of two months.

If the oceanic thermodynamics depends on mean zonal advection, equation (2.51), that is, when the temperature of water decreases where the mean temperature is highest due to its displacement towards colder regions, the instability characteristics are very different. In this case, the Kelvin wave is damped but the gravest Rossby mode ($n = 1$) is unstable (right panels in figure 2.5). The rate of growth increases with the wavelength and the phase speed is to the west, since it has opposite sign to k. The reason for the opposite direction of wave propagation with respect to the case discussed above can be similarly understood from figure 2.4. To amplify the Rossby wave it is necessary to displace the heat source to the west of the thermocline disturbance, so that the easterly oceanic currents of the Rossby waves and easterly winds coincide. This is the case when heating depends on mean zonal advection, provided the condition for the mean temperature along the ocean $\partial\bar{T}/\partial x < 0$ is sufficed. The coefficients used for this analysis are $c_A = 30$ m/sec, $c = 1.4$ m/sec, $A = B = 50 \times 10^{-7}\,\mathrm{sec}^{-1}$, $a = b = 10^{-7}\mathrm{sec}^{-1}$, $\gamma = 8 \times 10^{-1}\mathrm{sec}^{-1}$ and $\alpha = 7 \times 10^{-3}\mathrm{m}^2/\mathrm{sec}^{-3}/\mathrm{K}$.

Similar Kelvin and Rossby modes appear in models in which the sea surface temperature equation takes more realistic forms, as

$$\frac{\partial T}{\partial t} + u\frac{\partial \bar{T}}{\partial x} + v\frac{\partial \bar{T}}{\partial y} + w\frac{\partial \bar{T}}{\partial z} + \bar{u}\frac{\partial T}{\partial x} + \bar{v}\frac{\partial T}{\partial y} + M(\bar{w})\frac{T - s\eta}{h} + rT = 0, \quad (2.52)$$

where quantities with a bar describe a specified mean state, so that advection due to gradients of mean temperatures and temperature anomalies are taken into account. Here M is the Heaviside function ($M = \bar{w}$ if $\bar{w} > 0$, otherwise $M = 0$) and appears in an additional term representing the upwelling of a subsurface temperature proportional to the thermocline depth η. In this case, nevertheless, if the mean quantities vary spatially in a reasonable realistic manner, a new nonpropagating unstable mode appears [11] with high sea surface

temperature anomalies primarily in the eastern tropical Pacific. Conversely, to the west, a wave dynamics, which seems to answer the difficult question of the oscillating pattern of El Niño and La Niña, takes place.

According to this model, during a warm El Niño phase, westerly wind anomalies excite westward-traveling Rossby waves, which elevate the thermocline cooling the ocean according to equation (2.52). These waves propagate into the western Pacific where the thermocline depth is so large that they have little influence on the sea surface temperature and hence on the atmosphere, but are reflected as eastward-traveling Kelvin waves, which also elevate the thermocline upon reaching the western boundary of the basin. When this elevation reaches the central Pacific, it reduces the deepening of the thermocline caused by the local westerly winds, reducing consequently the intensitiy of the interactions between the ocean and atmosphere. Persistence of the westerly wind anomalies in the central Pacific implies continued excitation of Rossby and reflected Kelvin waves that further erode the development of El Niño conditions in the central Pacific until the westerly wind anomalies start to decay and La Niña starts to develop. Conversely, new easterly wind anomalies excite westward-propagating Rossby waves that now deepen the thermocline so that the cycle closes when these return to the central Pacific and terminate the cold La Niña. Since there are still thermocline-deepening waves on the way, these will be responsible for the intensity of El Niño which is up to come. This mechanism, explained for the first time in the work of Suarez and Schopf [106] is known as the *delayed oscillator*. The most important parameter in this model is the length of the basin, which determines the time needed by the reflected waves to return. The length of the Pacific is large enough to sustain oscillations of this kind, while that of the Atlantic is too small, so that initial perturbations in the winds would barely amplify.

2.3 Recent Developments

Since the oscillating pattern of the Southern Oscillation has been found as a consequence of the intrinsic dynamics of the coupled system of the ocean and the atmosphere, most of the attention in the understanding of this phenomenon has been directed to study its irregularity. There are several models which capture different modes, [10, 106, 135] , which are however periodic, so that random noise is necessary to make the oscillations irregular. It is also possible to obtain different frequencies by tuning the coupling parameters [74], and introducing nonlinearity in the interaction [119]. This assumption has been very productive, especially by modifying the equation (2.50) for the coupling of the sea surface temperature with the thermocline anomaly [70], since it has allowed the investigation of the Southern Oscillation as a chaotic time series [118], [126]. This could signify that the irregularity of the Southern Oscillation is, as its oscillating character, a consequence of the coupled dynamics.

Another interesting problem is the effect of the seasonal cycle on the Southern Oscillation. Most studies specify the values of the cycle in the dynamical equations, for it is extremely difficult to approach this problem in an attempt to illuminate quantitatively in detail the origin of the seasonal cycle itself. This problem has been tried only with coupled general circulation models [67]. Hence, the annual variability is examined primarily parametrizing the interaction between the ocean and the atmosphere. Chaos is also possible in this scenario, which however does not explain some well-defined temporal correlations of El Niño and the seasonal cycle [18]. The procedure of a seasonal depending parametrization has simulated correctly the phase locking of the Southern Oscillation to the seasonal cycle so that the heat anomaly in the eastern Pacific peaks in a standard composite El Niño towards the end of the year, principally as a consequence of a dynamical balance between the Kelvin and Rossby waves [32].

The introduction of stochastic forcing has been a fruitful step in examining the origin of the irregularity of the Southern Oscillation [83], since it accounts for "weather"phenomena of high frequency and very short memory, which have an effect in the dynamics that depends on the coupling of the ocean and atmosphere, which is in turn a function of the month of the year. Hence, it appears that the Southern Oscillation is more appropriately described as a stochastic process than as a result of chaotic dynamics [19]. Moreover, Wang [125] argues that the introduction of noise allows to consider El Niño as a phenomenon caused by stochastic resonance [2]. In the light of this results and the characteristic regular Oscillation of the ocean-atmosphere dynamics, it is possible to pose the problem of the irregularity of El Niño in terms of the role of stochastic forcing over modes which can be stable or unstable without forcing. There are consequently four possible scenarios for the dynamics of the El Niño and the Southern Oscillation (ENSO):

- ENSO is an unstable chaotic mode where stochastic forcing plays no important role,
- ENSO is an unstable, saturated mode, where external noise causes transient growth that either cancels or reinforces the warm and cold events so that they take on their irregular appearance,
- ENSO is a neutral or slightly damped mode where noise alters the phase and amplitude of the peaks so that they take on their irregular appearance, and
- ENSO is a highly damped mode where noise and transient growth create all warm and cold events.

Philander and coworkers [29] claim that the two extreme cases cannot describe appropriately the Southern Oscillation. The two latter possibilities are studied in detail in the work of Thompson and Battisti [111], [112].

The predictability of El Niño is a problem which is studied with dynamical and statistical methods. While the dynamical methods depend on the performane of the models, statistical methods have been affected by the scarcity of oceanographical data. Nevertheless, early studies such as [31], [36] and [37] have tried put some limits to the time in advance a correct forecasting can be made. Dynamical predictions [58], [134], [5] have shown that there is a so-called "spring barrier", which makes the prediction of events during the northern spring more difficult than during other times of the year. It has been tried to explain this effect as a consequence of the smallness of the signal to be forecasted [134]. The most addressed topics in the study of the predictability of the Southern Oscillation are the time in advance of a succesful prediction and the variability of the predictability along the months of the year. There is nevertheless much more to investigate about the predictability of the Southern Oscillation. The relationship of the predictability and time correlations of indices of El Niño has been analyzed by Ausloos and Ivanova [3] and Ortiz-Tanchez, Ebeling and Lanius [76]. In the latter of the works, the fact that the predictability of La Niña is significantly higher than that of El Niño has been detected and quantified. The study of the predictabilities of the Southern Oscillation in the present work is devoted to its relationship to mid-range correlations and a detail of the predictability of specific sequences obtained with three significative indices of the Southern Oscillation.

The El Niño of 1997-98 has shown that there is still much effort is necessary to understand and predict the Southern Oscillation reasonably. Many prediction methods [47], [105], [50] performed badly [80] and the search for an explanation for this circumstance is still on the run [120]. It is a possibility that during the past two decades the Southern Oscillation has changed, as investigations on the spring barrier reveal [6]. The effect that the global warming has on El Niño is studied at the present [28], [113], especially with modifications of the seasonal cycle. It remains to be seen to which extent the

overall changing dynamics of the earth affect the Southern Oscillation.

2.4 Impacts of El Niño

2.4.1 The problem of deep warm waters

The ocean of the western coast of South America is one of the most productive regions of the world oceans. The prevailing equatorward winds drive the surface waters offshore and cause the upwelling of deep and cold water, that is rich in inorganic plant nutrients, such as nitrate, phospate and silicate. This continuous injection of nutrients in the surface layers, where optimal light conditions prevail, sustains the high rate of primary production. Abundant phytoplankton are eaten by herbivores and, through grazing and predation, the organic matter passes up the food chain.

During El Niño there is decreased primary production, which disrupts the food chain and contributes to the reproductive failure of some species. The reason for that is not cessation of upwelling. The problem is that the upwelled water comes from relatively shallow depths. Normally the cold, nutrient-rich water is close to the surface, but during El Niño the depth of surface layer warm, nutrient-poor water increases so that the deeper richer water is inaccesible. It was noted by Gardiner-Garden [33], that the depth from which the upwelled water comes depends on the offshore shear of the wind. During El Niño the winds close to the coast remain strong but offshore the winds relax. Such a shear in the wind induces shallow upwelling. If the winds have no shear, then the depths of the water surface layer would not be affected; upwelling will always bring deep water to the surface. More references on the ecology on the coastal zone are given in Barber and Chavez [7], [8].

2.4.2 Some specific ecological changes

Several factors contribute to the decimation of the bird and marine life along the coast of South America during El Niño. One is reduced primary production, which affects the entire food chain. As El Niño evolves, nutrient-rich, cold water occupies a smaller and smaller volume, usually close to the coast. This causes some species to redistribute themselves spatially. For example, Peruvian anchovy (*Engraulis ringens*), which seek out and remain in relatively cold water of 16°C to 18°C, a temperature at which phytoplankton are abundant, become more concentrated on small pockets of cold water. Natural predators, especially humans can then reduce their numbers significantly. Some will survive a mild El Niño but during a severe El Niño, such as that of 1982-83 and 1997-98, the cool pockets disappear altogether and huge numbers of anchovies perish. The anchovy cath off Peru in 1983 was less than 1% of the catch a decade earlier.

Ecological damages during El Niño is not confined to the coast of South America. In 1982-83, relatively warm, nutrient-poor water appeared off the coast of California and contributed to productive failure of the northern anchovy (*Engraulis mordax*) and other species. In the central equatorial Pacific much of the usual marine life disappeared and the bird populations of several islands were decimated. Not only the food of the birds disappeared but nests in sand bars were flooded by the heavy rains [95]. Farther west, a severe drought in Indonesia contributed to a fire that ravaged vast tropical forest in 1997. Many details on the damages of El Niño of 1982-83 can be found in Caviedes [17].

Last but not least, not al species are adversely affected by the change in environment during El Niño. Along the coast of Peru both shrimp and scallop *Argopecten purpuratos* rapidly increased in abundance during El Niño of 1982-83. The scallops were local and probably increased because of excellent growing

conditions; the shrimp were probably carried southwards by the currents.

Chapter 3

Entropies and predictabilities of the observed data

This chapter presents the results of the application of the entropy concepts and methods to three relevant quantifiers of El Niño and the Southern Oscillation. These are the observed data of the sea surface temperature (SST) of the Hadley Centre for Climate Prediction and Research in England [92]; the Southern Oscillation Index (SOI) [116]; and the Multivariate ENSO Index (MEI) [133]. Attention has been paid to the behavior of these variables in the following two aspects: their evolution in the time after substracting the monthly means, and the evolution of the fluctuations of these series in the time. Hence, we have worked with six series, namely three *anomalies* and three *persistences*. The former are given by the difference of the climatic time series and its mean monthly values over a defined interval of time (known commonly as the climatology). Additionally, the persistences give the information about the relative monthly changes of the anomalies, i.e. the fluctuations y_{n+1} of the time series, $x_{n+1} - x_n$. With this set of variables the predictability of the Southern Oscillation will be explored.

3.1 The Hadley Series Data and the SOI and MEI Indices

The Hadley Centre for Climate Prediction and Research mantains a relatively long record of many global oceanographical variables and updates it regularly. The last of their publications [92], from 2002, includes the HadISST1 data set, comprising sea surface temperature since 1870. This data set is freely available [1] after sending a signed research license. The data of the HadISST1 set includes monthly means of the surface temperature of the global waters. These will be called henceforth chapter SST. For representing El Niño in the eastern tropical Pacific, it has been necessary to find the means of these data for the region known as Niño3, by averaging the data of the area between 5 °N and 5 °S and 90 and 150 °W.

As shown in figure 3.1, there is a remarkable difference between the Niño3 SST raw data and their anomalies. This is understandable in the light of the monthly variations of the SST data, figure 3.1. It is evident from this figure that during the spring months, the sea surface temperature in the tropical Pacific reaches a maximum, and that its growth is steeper than the descent to the lower temperature ranges of the autumn and winter months. It is also interesting that the maximum temperature is reached before the summer equinox and similarly the minimum is reached before the winter equinox, showing a phase shift with the planetary trend. By taking the difference between the data and the monthly means, the range of the SST anomalies reduces to a range of 4 degrees Celsius, with higher peaks in the positive side. This suggests there were large events of El Niño in the years of 1880, 1892, 1976, 1982 and the highest in 1998, while large La Niña occurences are observed in 1895, 1918, 1989 and the strongest in 1956, and are less strong than the El Niño phases.

[1] at http://dss.ucar.edu/ds277.3/

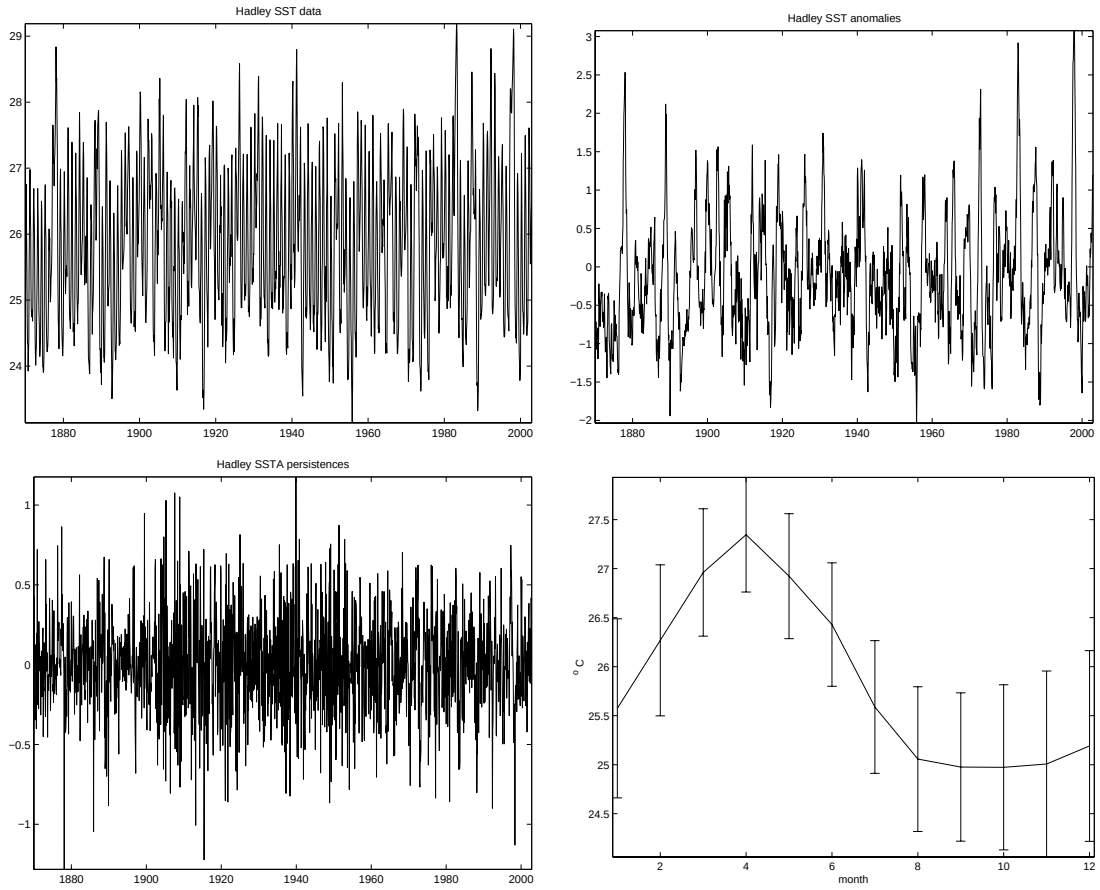

Figure 3.1: Time series of the Niño3 Hadley Centre's SST raw data, their anomalies, persistences and yearly trends.

In the following, the interesting characteristics of the sea surface temperature will be found on the basis of its anomalies. These appear to be considerably nonlinear or stochastic, and show time-dependent trends which are not directly related to the yearly cycle. These trends can be addressed with, for instance, the method of detrended fluctuation analysis [82, 128]. Here, the series will be considered as stationary for their short lengths, leaving further analyses of their structure in the time for the next chapter.

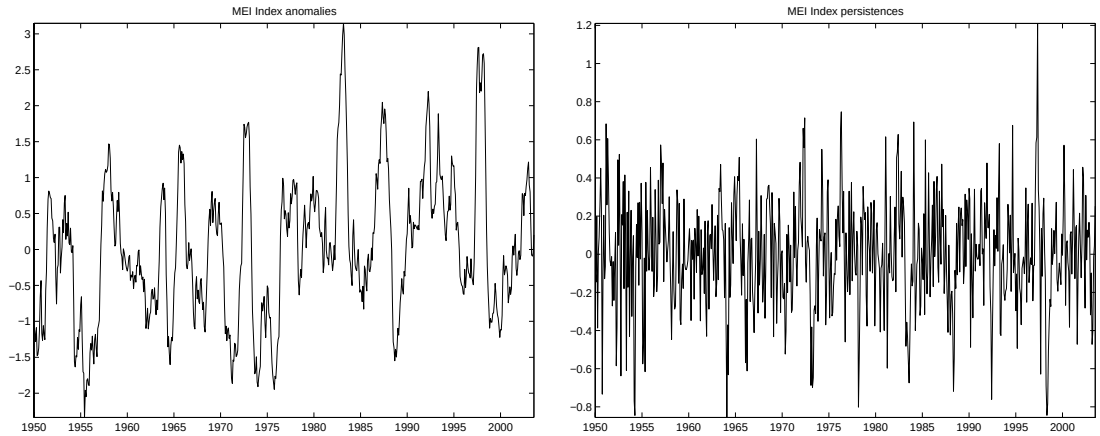

Figure 3.2: MEI Index data (anomalies) and their persistences.

The persistences of the sea surface temperature, as figure 3.1 reveals, have on the other hand a very fluctuating character. There are some fluctuations which exceed the 0.5 °C mark, while most of them do not surpass the 0.15 °C limit. The largest fluctuations in the Southern Oscillation have been only partially related to the largest events of El Niño and La Niña. This is the case for La Niña of 1918 and 2000, consequently making the prediction of large negative SST fluctuations a more interesting problem than that of positive fluctuations.

The Multivariate ENSO Index, also known as MEI and obtained as a courtesy of Professor Klaus Wolter [133], is a complex index which takes into account several oceanographical and meteorological variables and the principal component method [88] to construct a quantifier. The MEI index consists of already detrended values and further its variance for every month is normalized to one. This makes the term "MEI Anomalies"a tautology in a strict sense; nevertheless we will use it ocassionally to point to the detrended character of all the series.

The MEI Index is a very short time series, comprising the time since Jan-

uary 1950. This poses several problems to the analysis, since the frequencies and significances will make the interpretation more difficult than for the other series. It is however a considerably deterministic series, which can be useful to make predictions, since it is relatively continuous and has nevertheless well definite peaks.

The maximum values of the MEI Index took place in 1972, 1982 and 1998, in accordance with the SST record. The minimum values are also corroborated, which is a consequence of the role of SST as an important component in the construction of MEI. It is expected that the MEI will be of particular interest in the study of its persistences. These are evidently less erratic than those of SST and is thereby more appropriate for searching more predictable short sequences.

The Southern Oscillation Index (SOI) [116] consists of the atmospheric pressure difference between Darwin in Australia and Tahiti. It is a very fluctuating quantity, more than the foreshown indexes, as shown in figure 3.1. As with MEI, this index is already detrended so that both terms SOI and SOI anomalies will be used equivalently. Since a positive pressure gradient from the western to the eastern Pacific corresponds to the phase of La Niña, the SOI has the opposite sign with respect to the other quantifiers of the Southern Oscillation.

It is possible to trace the SOI back to 1870. In this period of time, the SOI gives evidence of two big El Niño events around 1900 and reveals large pressure disturbances during the events of 1940, 1952, 1992 and 1998. It is nevertheless a characteristic of El Niño and SOI that this does not show the same largest anomalies of SST and MEI, which are far stronger in these series. The persistences series of the SOI is comparable to that of MEI, larger and without visible trends, it is a series which could complement the information on the fluctuations with more frequent data.

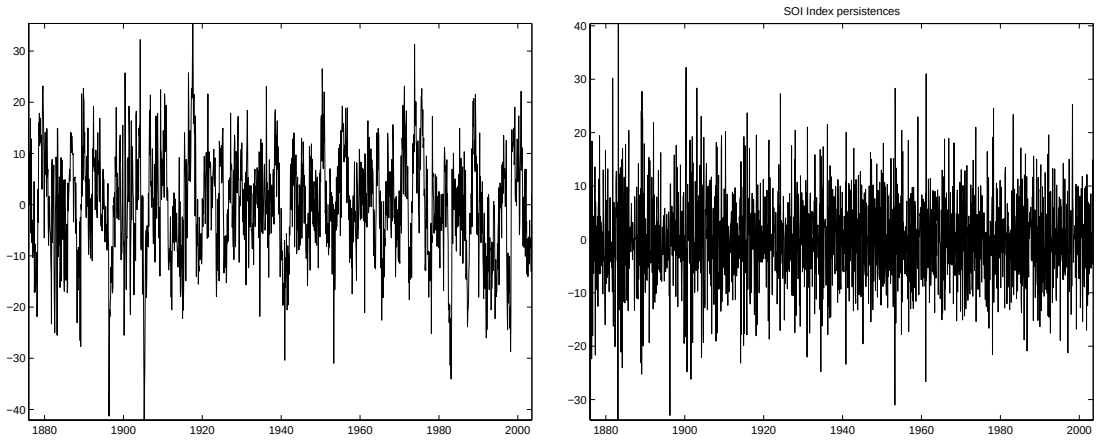

Figure 3.3: SOI Index data (anomalies) and their persistences.

3.2 Power spectra and correlations

The most important characteristic of the Southern Oscillation are its irregular periodicities. They determine in which year a phenomenon of El Niño or La Niña will take place, or if the tropical Pacific behavior will be neutral. Since none of the time series of SST, MEI or SOI anomalies or persistences correspond to a linear *and* deterministic process, the Fourier power spectra in the time of these variables show many peaks, where the highest of them represent the most recurrent periodicity to be expected for every variable.

As figure 3.4 reveals, the anomalies of the Hadley Centre's SST data show their strongest periodicities in a time interval between three and four years, with a third large peak around six years. There are two other peaks of smaller extent around five years and another around three years, which together should account for most of the variability of the time series in its extreme episodes. There exists, however, variability of SST on longer time scales. This cannot be found for larger periods, since the Fourier transform is strongly affected by the length of the series. This will be the case in the study of the MEI anomalies below.

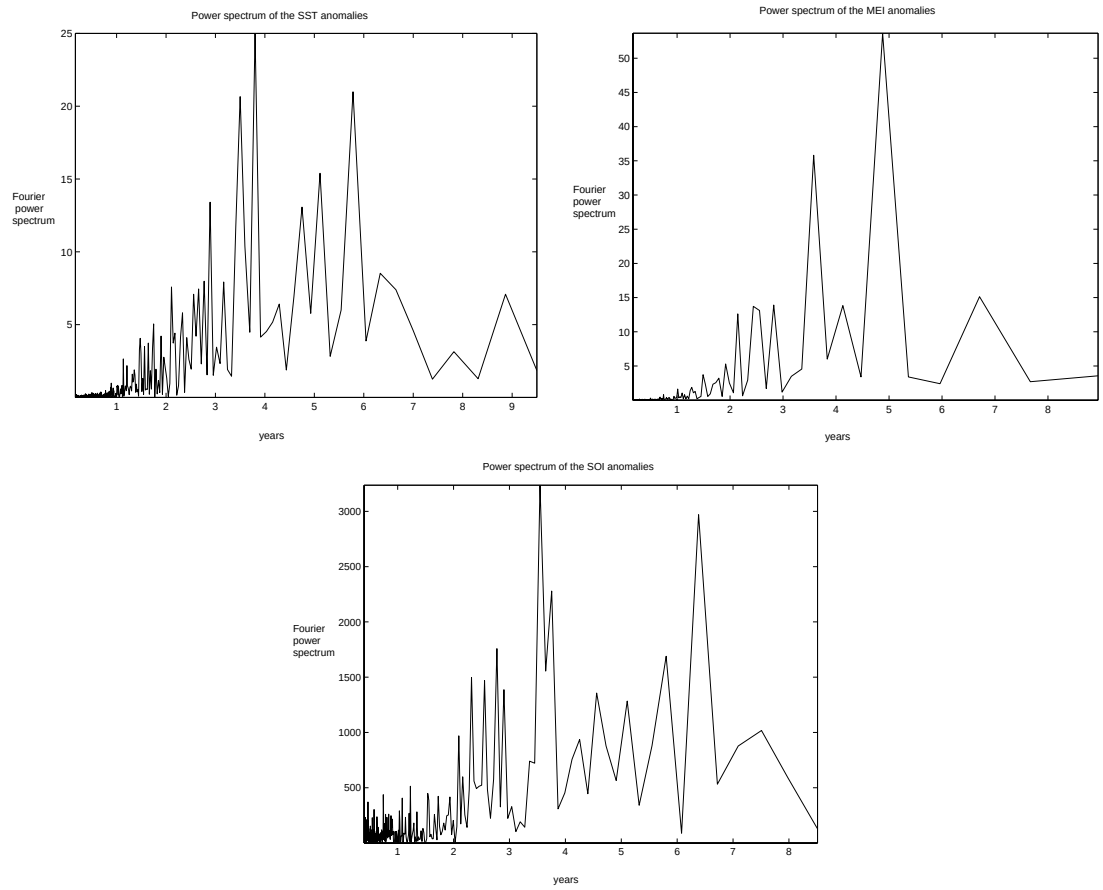

Figure 3.4: Power spectra vs. time in years for the SST, MEI and SOI anomalies series.

Conversely, the MEI anomalies show only two high peaks, around five and three and half years. This is not fully in concordance with the spectrum of the foregoing series, even though SST is definitely an important component of MEI. Part of the answer to this discrepancy lies in the fact that, as a much shorter time series, MEI does not allow for the same resolution as SST, leaving a broad band of time in which the peaks of MEI can really be sharply located or distributed between the depicted points. A consequence of the shortness of the MEI series is thus that the spectrum cannot be extended with any desirable

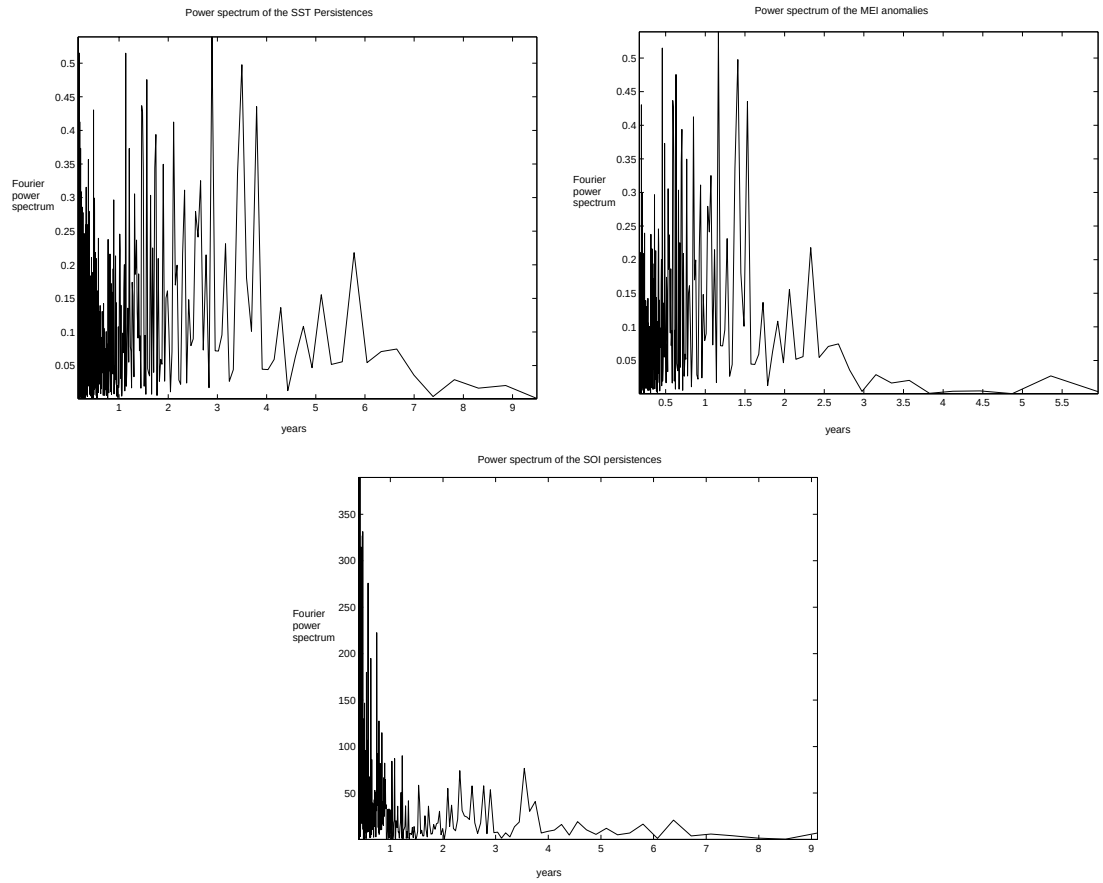

Figure 3.5: Power spectra vs. time in years for the SST, MEI and SOI persistences series.

reliability beyond a periodicity of eight years.

The anomalies of the SOI present a somewhat more similar structure to the SST than those of MEI. This is a remarkable result though the difference in the series is evidence for the importance of interactions between the ocean and atmosphere in El Niño and La Niña phases, which perceived as a superposition of high anomalies in the climatological variables are responsible for most of the interannual variability. Again, periods of three to four years and around six years are the most pronounced. It is notable that the last of these periods has

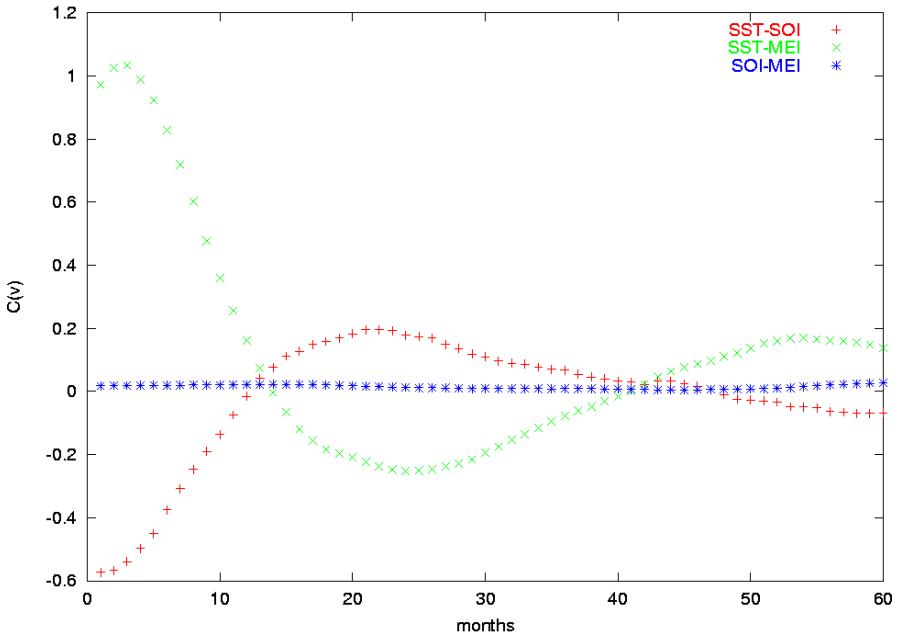

Figure 3.6: Correlations between the SST anomalies, MEI and SOI series.

been responsible for the strong El Niño events of the last decade.

The spectra of the fluctuations are much more complex than that of the anomalies. This is shown in the figure 3.5, where no definite periods in the persistences of any of the time series is found. There is a prohibitive amount of noise in them originated in the plot of the spectrum as a function of the period in a linear scale, since it is the inverse of the frequency found in the periodogram. This effect is included to illustrate more complex noise frequencies of the following chapter. The SST persistence data presents the periodicities at the higest time scales, up to four years, but like for the other variables, with no more influence than periodicities even under one year. As an extrem case, the SOI series consists almost only of very rapid fluctuations.

It is also interesting to observe the redundancy in the information given by the different time series. For this purpose the cross-correlations between the

time series have been found, as given for the time series $X = x_1, ..., x_{max}$ and $Y = y_1, ..., y_{max}$ as

$$C(t) = \frac{< x_n y_{n+v} > - < x >< y >}{\sigma_x \sigma_y} \tag{3.1}$$

and is depicted in the figure 3.6. It is found that there is certain redundancy in the information given by the SST anomalies and the SOI, which takes the form of an anticorrelation, related to the different signs of the series at El Niño and La Niña events. This correlation has the magnitude of 0.6 of the product of the standard deviations of both series and decreases as a damped sinusoid, reaching the first zero correlation after thirteen months. A similar case is found between the SST and MEI series, which higher correlations than the former ones. Here, the correlation reaches the value of the product of the standard deviations and is highest until the time lag of MEI is larger than four months, and becoming zero again after thiteen months. In this both cases is the behaviour of the correlation oscillatory, though not periodic or related to the yearly trend. Conversely, the correlation between the SOI and MEI indexes is negligible and independent of the time lag. Hence, it appears that there is a certain redundancy specially in the data of SST and MEI, an understandable result, since SST is one of the variables used in computing MEI. Nevertheless, it should be remembered that this correlation analysis only accounts for linear relationships between the variable and hence nonlinear quantifiers as the transinformation lead to complementary results.

3.3 Shannon and dynamical entropies and Partitions

In order to make an entropy anaylisis of SST, MEI and SOI, it is first necessary to find the optimal partition for the series. As known from chapter one, it is useful to approximate empirically the optimal partition, as long as no generating partition can be found. Some extensions of this procedure are given in the references [26, 90, 104]. Consequently, we have maximized the Shannon entropy as a function of the partition borders for every series, to divide them into two to five segments corresponding to a binary to a fifth-order partitioning procedure. This procedure is justified from the principle of maximum entropy, which establishes the condition for the less-biased prediction and prevents us from applying other apparently more comfortable (e.g. noise-reducing) partitions. We will analyze the results of this partitioning in the following sections.

3.3.1 Binary Partition

We introduced one partition to the anomalies and persistences series, and calculated the Shannon entropies and the dynamical entropies up to the fifth order in dependence of the location of the partition. From the discussion about the principle of maximum entropy (section 1.1.2), the location of the partition border which produces the maximum entropy values is of primary importance, since it is the best estimator of the border for the less biased prediction. This location is given in terms of the cumulative probability associated to finding one value of up to this point in a time series. This means, for instance, that a probability of 0.5 represents the median of the histogram of the series, and 0 and 1 are its extreme values.

The dependence on the partition border is a simple problem for the case

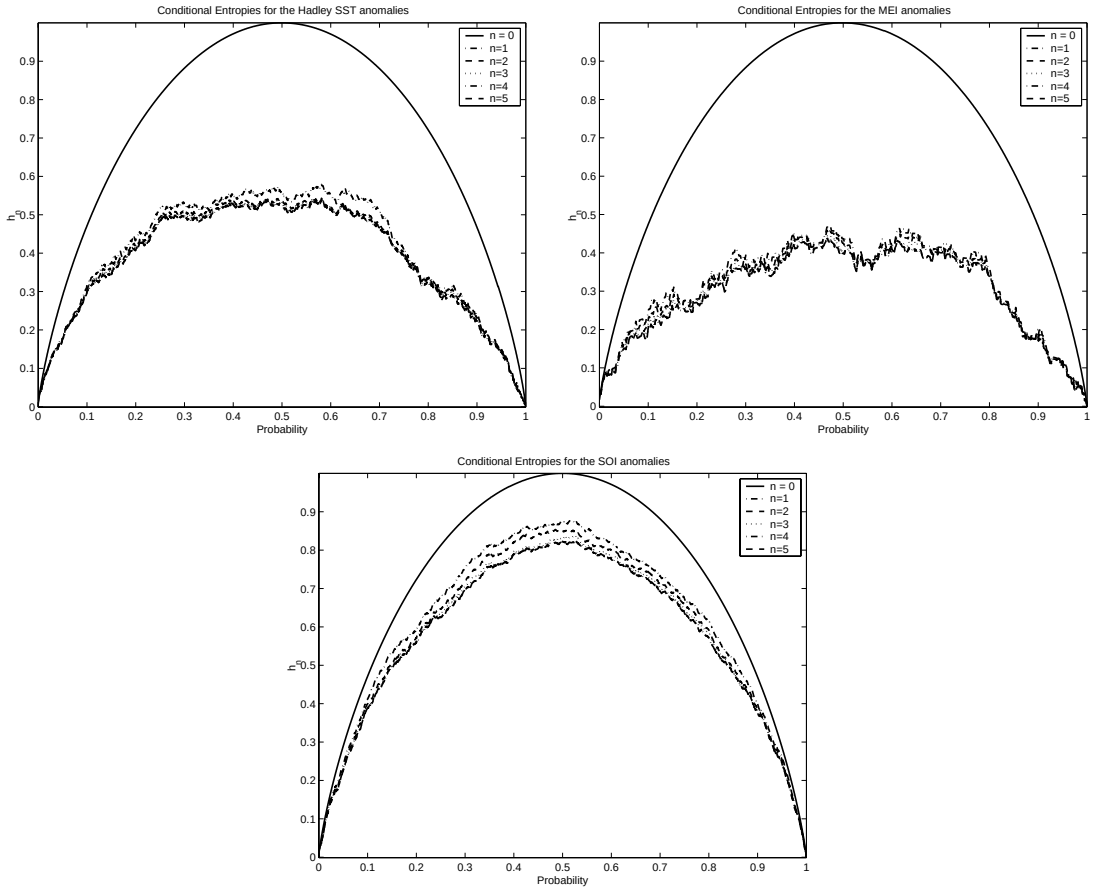

Figure 3.7: Shannon and dynamical entropies for the SST, MEI and SOI anomalies as a function of the location of the partition, in probability.

of the Shannon entropy of zero order, since this attains its maximum value of one only for the equiprobable distribution. In general, the behavior of the Shannon entropy with a variable partition border is given by its definition, the $p(x)\log p(x)$ law, which appears as the upper curve in the plots of figure 3.7.

It is found in this figure that the greatest dynamical entropies for every anomalies series are located not far from the median of the distribution, even though not necessarily there. Several regions of relative entropy maxima can be found, especially for the SST anomalies. Nevertheless, for the different orders

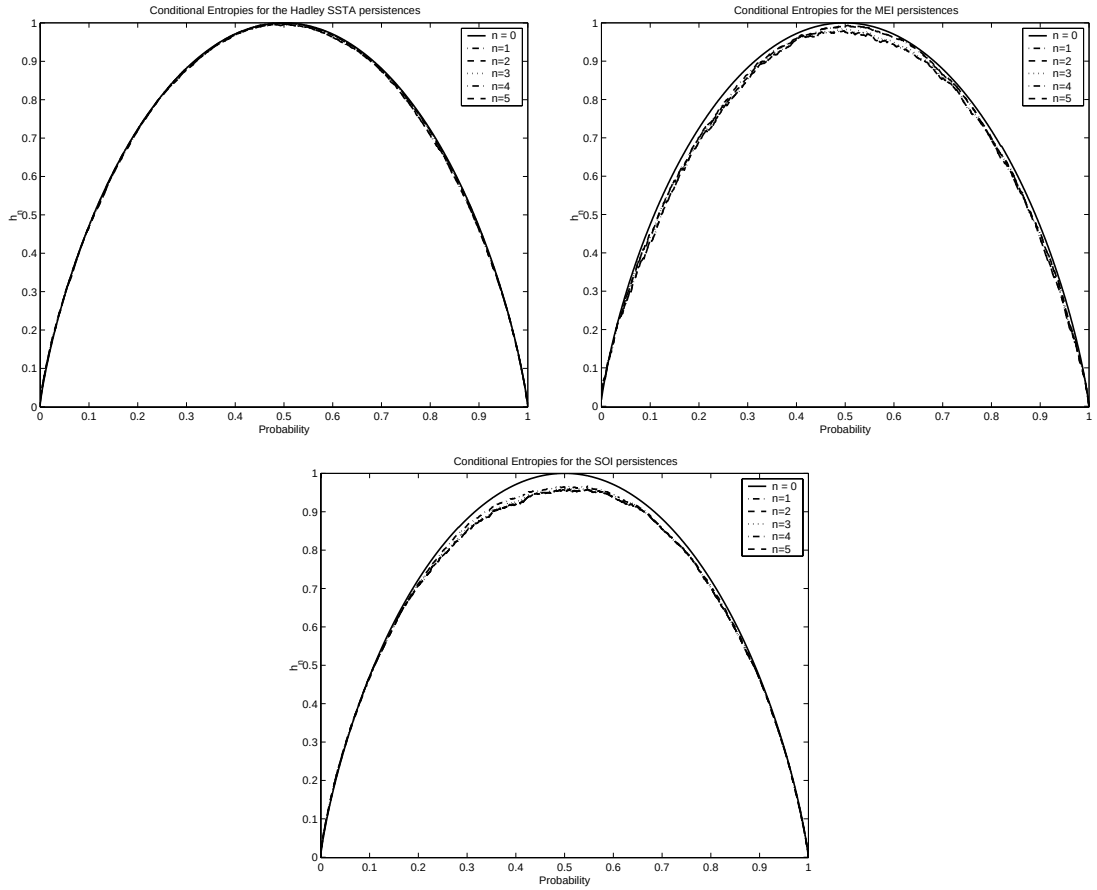

Figure 3.8: Shannon and dynamical entropies for the SST, MEI and SOI persistence as a function of the location of the partition, in probability.

of the dynamical entropies, henceforth *dynamical orders*, the entropy maxima of a series are located in the same probability region, so that variations in their location result negligible. For the SST anomalies series, the greatest entropies are found in the peak at probability 0.58, while for the MEI this happens at 0.47 and for the SOI, the maximum is more symmetric and is located at probability 0.51.

The persistences series in figure 3.8 show, in accordance with the previous results, very high entropies for every order. Here the dynamical entropies are

almost not distinguishable from the Shannon entropy, being the SST series the extreme case. This fact is evidence in the average, that there is only a small gain in predictability by providing the values of one of these time series in the past, up to the fifth month. The maximum entropies are found introducing the partition in the immediate vicinity of the median of each series and these attain values well above 0.95 for any index in any order. Though the entropies are high on average, the persistences series remain interesting to investigate to which extent the predictabilities are enhanced with a finer partitioning procedure or if there are some particular blocks in the persistences series, which have nevertheless a well-defined symbol following them in the sequences.

3.3.2 Tertiary Partition

By introducing a tertiary partition, it is possible to follow the dynamics of a process in the positive and negative directions, as well as differentiating it from fluctuations below a threshold. For this purpose, an evaluation of the entropies for every time series of the anomalies and persistences was performed, after

order	SST borders		MEI borders		SOI borders	
0th	0.325670	0.670498	0.293160	0.635179	0.319574	0.659121
1st	0.249042	0.574713	0.244300	0.635179	0.339547	0.679095
2nd	0.249042	0.574713	0.439739	0.781759	0.339547	0.659121
3rd	0.249042	0.613027	0.390879	0.781759	0.339547	0.659121
4th	0.249042	0.613027	0.390879	0.781759	0.319574	0.599201
5th	0.249042	0.613027	0.390879	0.732899	0.339547	0.739015

Table 3.1: Borders of the optimal tertiary partitions applied to the SST, MEI and SOI anomalies series.

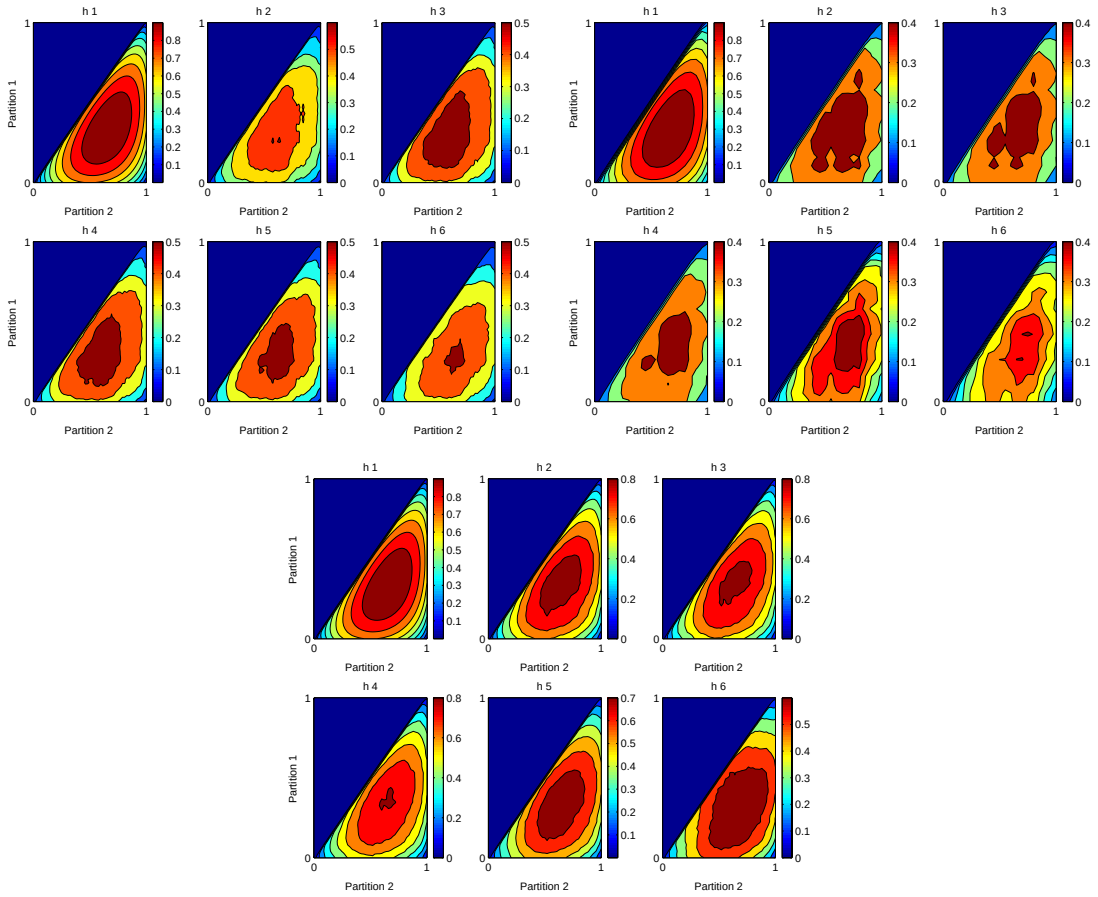

Figure 3.9: Shannon and dynamical entropies up to the fifth order for the SST, MEI and SOI anomalies as a function of the location of the borders of a bidimensional partition, in probability units. The graphs are in groups of six according to its originating time series from left on the top to bottom, h1 to h6 refer to the order of the Shannon entropies, which is one more than the order of the dynamical entropies.

dividing the series in three segments. The borders of the series are determined again applying the principle of maximum entropy and are displayed in figure 3.9 for the anomalies and figure 3.10 for the persistences. The pictures in this figure show as contour plots the entropies associated with any couple of

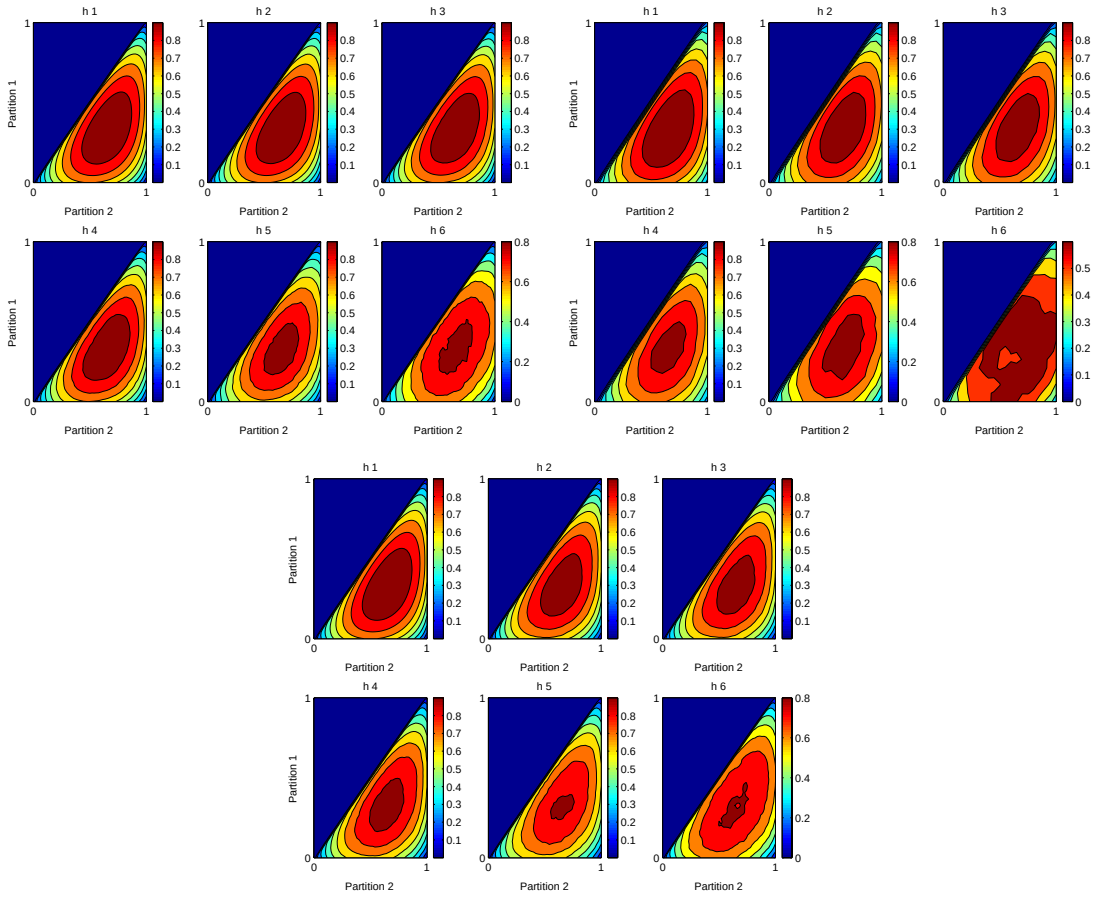

Figure 3.10: Shannon and dynamical entropies up to the fifth order for the SST, MEI and SOI persistences as a function of the location of the borders of a bidimensional partition, in probability units. The graphs are in groups of six according to its originating time series from left on the top to bottom, h1 to h6 refer to the order of the Shannon entropies, which is one more than the order of the dynamical entropies.

partition borders, where the x axis represents the first border in the units of cumulative probability along the series, and the y axis the second border, as a probability beyond the first. This representation requires only the usage of the space below the diagonal of the space of probabilities represented by the

order	SST borders		MEI borders		SOI borders	
0th	0.325879	0.670927	0.331754	0.663507	0.319787	0.659560
1st	0.325879	0.651757	0.347551	0.663507	0.319787	0.659560
2nd	0.325879	0.651757	0.315956	0.631912	0.299800	0.639574
3rd	0.287540	0.651757	0.315956	0.663507	0.299800	0.639574
4th	0.287540	0.632588	0.410742	0.710900	0.319787	0.659560
5th	0.249201	0.594249	0.221169	0.774092	0.259827	0.599600

Table 3.2: Borders of the optimal tertiary partitions applied to the SST, MEI and SOI persistences series.

unit square. This is justified by the symmetry of the entropy to the labeling of the partition borders: it is enough to let the second border to run after the position of the first. As the upper half of the probability square is equivalent to interchange the borders of the half square below, it does not contain any additional information and does not need to be computed.

Figure 3.9 shows the entropies for the series of the anomalies, and in particular the existence of a pattern of increasing entropies towards the center, which attain its maximum values when a set of approximately equal partitions is applied. There is a strong decrease on the maximal dynamical entropies of the SST series when their order is increased from zero ($h = 1$) to one ($h = 0.60$), while for higher orders the decrease is moderate, reaching $h = 0.53$ for the fifth order. The entropies of the MEI series attain for the first order the value $h = 0.48$ and similarly continue decreasing moderately until $h = 0.40$ for the fifth order. For the SOI series this happens in a more gradual manner and conserving better the symmetry of the partition sizes. The first-order maximal entropy reaches the value 0.85, the third-order maximal entropy of 0.81 and

the sixth order of 0.69. The borders of the optimal partition for these and the persistences series are summarized in the tables 3.1 and 3.2. As for the binary partition, when the dynamical order is one, both the SST and MEI anomalies series are best partitioned with asymmetric partitions. Interestingly, since the highest partition remains similar to that for a binary partition, the intermediate partition appears to have been incorporated in the lower partition in the binary case. The symmetry properties of the partition borders nevertheless change with the dynamical order, since now there are more regions of relative maxima as those in figure 3.7, whose heights depend on the election of the other border.

For the persistences series, the variability with the tertiary partition is characterized by a slow decrease in the entropy for an increasing partitioning order, as can be observed in figure 3.10. that the first-order dynamical entropies differ only slightly from the zero-order entropies which have value unity. After a slight decrease of the entropies with the first dynamical order, in contrast to the analysis for the binary partition, the entropies of the persistences decrease further considerably as the dynamical order grows. It is found that the enhancement in the predictabilities for the SST, MEI and SOI elevating the dynamical order from 1 to 5 are 0.17, 0.30 and 0.15 respectively. Since this difference is largest for the MEI series, this appears to be the quantifier which, on average, allows by far the best results when applying entropy methods to the noisy series of persistences. Reminding that there was no difference found in the predictability for any series with any dynamical order in the binary partition analysis, it appears that a finer partition is necessary to investigate the predictability of the fluctuations of all indices.

3.3.3 Quaternary and fifth-order partitions

A graphical representation of the borders of the optimal partitions for the Shannon entropy as given by the cumulate distribution of the ENSO indices is shown in figure 3.11. The partitions borders are found by searching an equal amount of symbols in every partition, which is revealed by the fractions of the y axis contained between two neighboring borders of partitions of the same order. Since it is not possible to display the partition borders for higher entropy orders, we limit to refer to their basic properties with the help of tables.

A detail of the quaternary partitions with the maximum entropies is given in the tables 3.3 and 3.4. The entropies of the anomalies series are in the range of 0.99 to 0.47, the latter in the fifth order for the SST, and similarly 0.36 for the MEI and 0.56 for the SOI in the fifth dynamical order. For the persistences series the minimum entropy values are 0.61, 0.51 and 0.61 respectively.

order	SST borders			MEI borders			SOI borders		
0th	0.2263	0.4851	0.7438	0.1954	0.4397	0.7328	0.2361	0.5060	0.7422
1st	0.2263	0.4204	0.6468	0.2443	0.4397	0.7817	0.2699	0.5060	0.7759
2nd	0.2263	0.4204	0.6468	0.2443	0.4397	0.7817	0.2361	0.4723	0.7085
3rd	0.2263	0.4527	0.6791	0.1954	0.4397	0.7817	0.2361	0.5060	0.7759
4th	0.2263	0.4527	0.6791	0.1954	0.4397	0.7817	0.2024	0.4385	0.8434
5th	0.2263	0.6144	0.8732	0.1465	0.3908	0.7328	0.1686	0.5398	0.9446

Table 3.3: Borders of the optimal quaternary partitions applied to the SST, MEI and SOI anomalies series.

These partitions are interesting since they allow a dynamic determination of fluctuations and relevant events in the positive and negative directions.

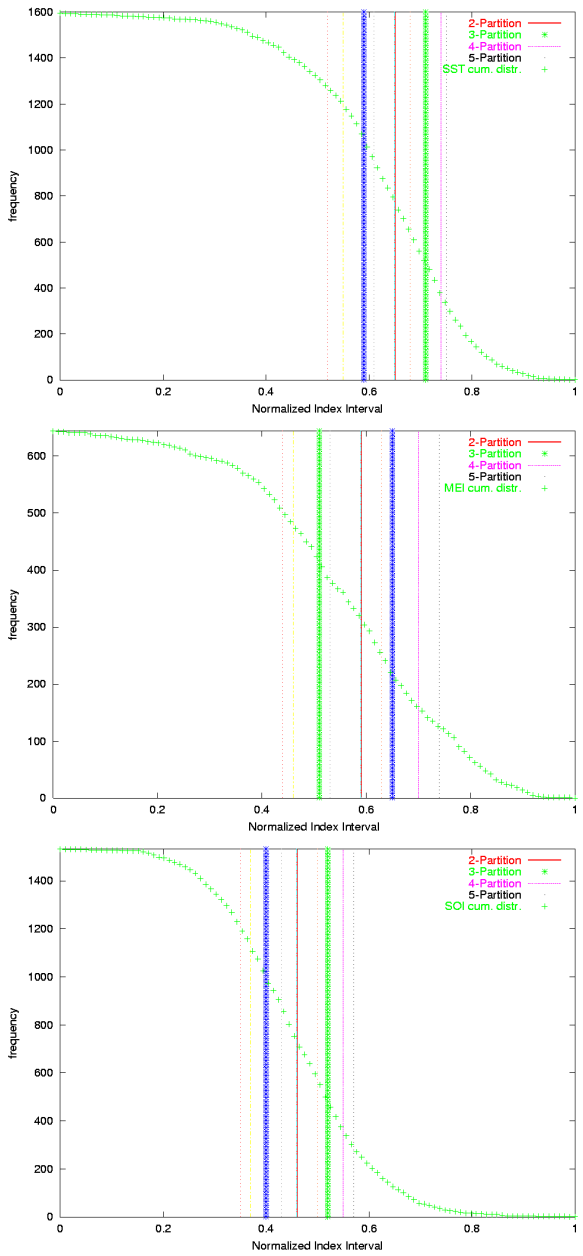

Figure 3.11: Cumulative distribution of the ENSO indices and partition borders of order 2 to 5 for the Shannon Entropy.

order	SST borders			MEI borders			SOI borders		
0th	0.2265	0.4854	0.7443	0.2388	0.5015	0.7404	0.2363	0.5064	0.7427
1st	0.2265	0.4854	0.7443	0.2627	0.5015	0.7404	0.2025	0.4726	0.7427
2nd	0.2265	0.4854	0.7443	0.2388	0.5015	0.7165	0.2025	0.5064	0.7427
3rd	0.2589	0.4854	0.7443	0.2388	0.5015	0.7643	0.2025	0.5064	0.7427
4th	0.2265	0.4530	0.7443	0.2388	0.4060	0.7165	0.1688	0.4388	0.7427
5th	0.2265	0.5501	0.5825	0.2388	0.2149	0.7643	0.1584	0.4025	0.7427

Table 3.4: Borders of the optimal quaternary partitions applied to the SST, MEI and SOI persistences series.

Nevertheless, we are here confronted with a new problem: the distribution of the actual events in the space of the n-blocks. For l symbols, each derived from a partition, and a dynamical order of m, the amount of possible blocks which exists for any time series is l^m, which for this case attains values up to 1024. This is a bigger value than the possible 5-blocks of the MEI series $N_{MEI}-4$, and hence the entropy becomes an unreliable predictability estimator. It is, on the other hand, desirable to have many blocks representing the different frequencies for each of the possibilities. This is a condition beyond the possibilities of any of our series with a quaternary partition to the 5th dynamical order.

A fifth-order partition has an ever larger number of blocks, which should all be occupied in order to achieve good statistics. The computation with an increase of the number of blocks to this extent is very time consuming, too. Such a fine partition is extremely interesting, but since this condition cannot be fulfilled for large dynamical orders, we have opted to use this partition to find the borders only for the zeroth and first orders. The optimal partitions found and used in the entropy analysis with a fifth-order partition are given

order	SST anomalies borders			
1	0.161708	0.355757	0.582147	0.776197
2	0.226391	0.388098	0.549806	0.679172
order	MEI anomalies borders			
1	0.168350	0.336700	0.589226	0.757576
2	0.168350	0.420875	0.589226	0.757576
order	SOI anomalies borders			
1	0.168691	0.371120	0.573549	0.775978
2	0.134953	0.371120	0.573549	0.775978
order	SST persistences borders			
1	0.161812	0.355987	0.582524	0.776699
2	0.161812	0.355987	0.550162	0.776699
order	MEI persistences borders			
1	0.195759	0.391517	0.587276	0.783034
2	0.146819	0.342577	0.538336	0.734095
order	SOI persistence borders			
1	0.168805	0.371371	0.573937	0.776502
2	0.168805	0.371371	0.573937	0.776502

Table 3.5: Borders of the optimal fifth-order partitions applied to the SST, MEI and SOI anomalies and persistence for second order entropies.

in the table 3.5.

3.4 Conditional and Local Entropies

In this section we present the results of the entropy analysis concerning the predictability of individual n-blocks. For this purpose, the conditional en-

tropies for each of the anomalies and persistences series have been computed, for binary to fifth-order partitions, with the borders found in the previous section. These entropies have been depicted in the figures 3.12 to 3.17 with several details. There are many interesting aspects which can be analyzed, such as the distribution of the entropies and its values, the associated frequencies for every event and the relationship between the predictability of the blocks and chance, all of them for each series. A relevant methodic step in the analysis is given by the division of the blocks consisting of sequences of only the same symbol (*constancies*) and blocks which consist of different symbols (*transitions*).

To address these issues, the conditional entropies of 589 useful n-blocks were analyzed. These are the blocks of the following combinations of number of partitions and dynamical orders: a binary partition from the second to the sixth-order conditional entropies, a tertiary partition from the second to the fifth-order entropies, a quaternary partition from the second to the third-order entropies and a fifth-order partition in a second-order entropy analysis. All the partition borders used are those found in the optimal partition analysis of the latter section. These combinations of partitions and dynamical orders were selected to exploit the maximum information content of all three ENSO quantifiers permitted by their lengths while keeping comparable results between the series. Since the estimation of the variance of higher-order entropies is not yet solved problem, we will introduce an alternative approach to test the meaningfulness of the entropies, based on the significance that the entropies of the blocks probably will not be found by chance. This will be of use in the detailed study and selection of the interesting transitions, since there will be no prior need for a particular selection other than a sufficient frequency of the blocks.

3.4.1 Entropies and Frequencies

Figure 3.12 shows the distributions of the entropies and frequencies of the SOI, SST and MEI anomalies corresponding to all 589 analyzed n-blocks, each for all time series. The plots of the entropies and frequencies are characterized by a left side with blocks of zero or unity frequency and, consequently, zero entropy, and a right side with blocks of irregular frequencies and a steeply growing entropy. The plot takes this form as is ordered in the manner of an histogram in which the entropy increases. Each part of every plot is of different length: this is an expression of the proportion of the blocks which occur only once or are not present in the series (and therefore are given entropy zero) and those which appear more frequently.

It can be seen for all series that the most frequent blocks coincide in great part with those of the least entropy. This is an important result and a necessary condition for a reliable estimation of the most predictable states. Comparing the indices, the SOI series (on top) shows the largest section of populated blocks, leaving seventy of the 589 blocks empty, and containing a uniform curve of growing entropies which is steeper than that of the other two ENSO indices. To this series belongs only one block with an entropy below 0.5. In the plot in the middle, the SST anomalies series presents 217 blocks of zero-frequency, a fact which is not a consequence of finite-size effects, since its length is comparable to that of SOI. Having in addition 31 blocks with high frequency and uncertainties below 0.5, this is evidence for a predictability and order inherent to this series which is higher than that of the SOI. Due to its smaller length, the MEI anomalies series (at the bottom) shows the graph with the largest section of zero-frequency blocks. This series shows 343 empty blocks and simultaneuosly the smallest entropies of all the series in most of its 28 blocks of uncertainties below 0.5. Thus, it could be believed that the most predictable symbolic sequences of the anomalies of ENSO can be detected by

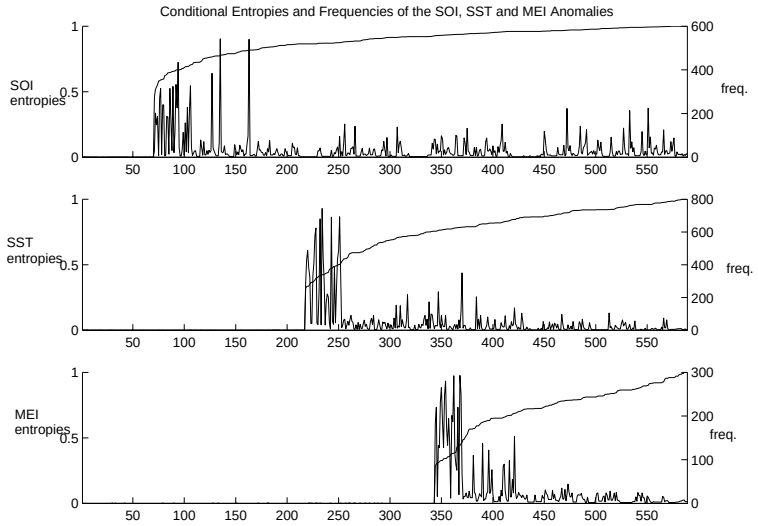

Figure 3.12: Conditional entropies of 589 blocks from the SOI, SST and MEI anomalies series. The histogram of the entropies (continuous curve, scale in the left y-axis) and the frequencies of the respective blocks (irregular curve, scale in the right y-axis) are depicted. The x axis denotes the numbering of the blocks, which obeys an order of increasing entropy.

the MEI quantifier, while its most complete dynamics in the symbolic phase space are found with a study of the SOI. Nevertheless, these indices present difficulties for they are extreme cases of an opposite relationship between an extense distribution of the blocks in the space and the amount of blocks with low predictability. Thus, a more equilibrated variable in length and predictability like the SST should be more reliable. Having similar predictabilities as MEI and being much more deterministic than SOI, this series allows for a more significant and sharply distributed study of the lowest predictabilities of the anomalies of the Southern Oscillation, after the occurence of an arbitrary block.

Figure 3.13 shows the same plot for the persistences of ENSO, which are

considerably different. First of all, there is no visible correlation between the size of the entropies and the frequency of the blocks. In this light, it cannot be assured that most of the interesting blocks comply with enough statistics. Comparing again the indices, the SST (middle plot) is the index which populates the most possible blocks after the symbolic dynamic analysis. There are only four symbolic events which do not occur from this series, all of them at the fifth order with a terniary partition. Hence, the SST is the variable which fluctuates in most of the symbolic phase space, while it can be seen that its entropies are distributed very steeply towards one. Contrary to the analysis of the anomalies, the SOI persistences series (on top) has more unused blocks and a more broadly distributed spectrum of frequent blocks than SST. The entropies of the series are, however, similarly very high, a fact which prevents most of the fluctuations from having a definite following block. As ever, the MEI series (below) is the only series giving a large number of zero-frequency blocks. This fact is related to the length of the MEI series but also to a particular regularity of its anomalies, since it is shown from SST that a relatively ordered anomalies series does not imply an order in their persistences.

The steepness of the growth of the entropies is much higher for all of these series than for their anomalies, as can be illustrated with three statistics of the distributions of the entropies: for the SOI, 88% of the blocks of non-zero frequency have entropies above 0.90, 69% of them above 0.95 and 25% above 0.99. The same results for the SST are 96%, 73% and 30% respectively, as 78%, 50% and 15% for the MEI. Consequently, it is difficult to choose any of the ENSO persistence sequences for using the conditional entropies up to the fifth order in predictability problems. The general problem of finding useful predictabilities is better suited for an investigation of the anomalies series. However, an interesting question for the study of both anomalies and persistences remains unanswered: which of these series gives a higher predictability

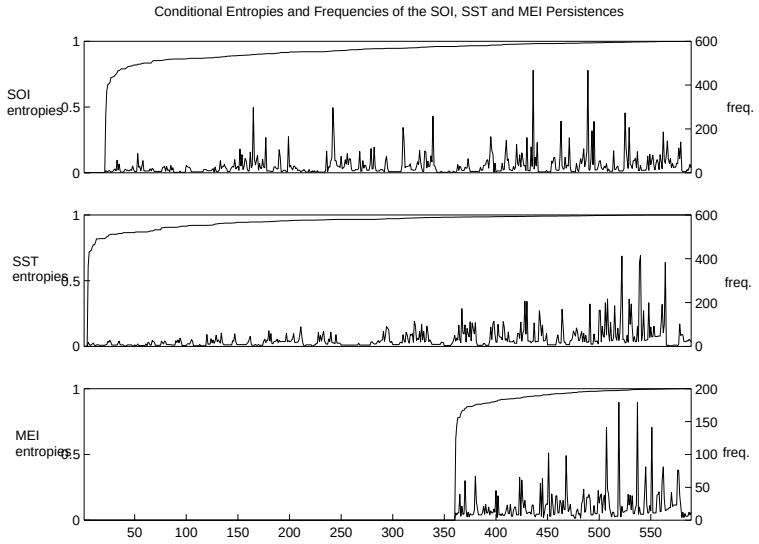

Figure 3.13: Conditional entropies of 589 blocks from the SOI, SST and MEI persistences series. The histogram of the entropies (continuous curve, scale in the left y-axis) and the frequencies of the respective blocks (irregular curve, scale in the right y-axis) are depicted. The x axis denotes the numbering of the blocks, which obey an order of increasing entropy.

after a specific development in the Southern Oscillation, i.e. a definite n-block has been found.

The study of the frequencies of the analyzed series gives results which similarly differ for the anomalies and persistences. For the anomalies, as will be evident in the next section, it is found that the most frequent blocks represent constancies, and that these are more frequent over many lengths for some partition than over several partitions for some length. This means that, for the resolution allowed by the length of the series, the tendency for a state to be maintained is considerably preponderant over the fluctuations. This can be illustrated, for instance, with the fact that the most frequent block of a tertiary partition is found in the sixth, seventh and eight position in the histograms of

frequencies of SOI, SST and MEI, respectively, while before them only binary constancies (which are sequences of zeros and ones) are present.

For partitioning orders greater than two, the constant blocks at the extremes of the partitioned space are more frequent than those in its center, and their entropies are lower in the extremes than in the center. As a further example, for the second-order blocks from tertiary partitions of the SOI anomalies, the El Niño phase is represented with 327 blocks, La Niña with 315 and the neutral state in between with 214. There are 195 transitions to an El Niño, 184 to a La Niña and 294 to the intermediate state. Remembering that the constancies of each state correspond to one block, while the amount of transitions to each of the states for this partition is given as the sum of two blocks, it should be clear that the constant blocks are the most represented even in the noisiest series.

The case of the persistences differs, since the frequency of the blocks is not related to their character of constancies or transitions, and small blocks of higher-order partitions are found with higher frequencies than larger ones of smaller partitions. The most frequent blocks of the SOI fluctuations are the elementary binary transitions 01 and 10, occuring 467 times and followed by their respective constancies 00 and 11 which occur 297 times. The same four blocks are more frequent in the SST, where the constancies appear more often (414 times) than the transitions (383 times), as occurs in the MEI, with 179 against 141 times. These results will be encountered and addressed in more detail below, in the context of their predictabilities.

For the study of individual blocks we shall introduce the following notation: the label of the block will be followed by a p preceding the number of the partitions. Thus, for instance, the mentioned elementary blocks of dynamical order 2 with a binary partition will be denoted as $'00\,p1'$ and $'11\,p1'$ for the constancies, and $'01\,p1'$, $'10\,p1'$ for the transitions.

3.4.2 Conditional entropies of the constancies

The most predictable constancies for the anomalies and persistences are shown in the figures 3.14 and 3.15, ordered as their conditional entropies grow. Each plot shows the conditional entropies of the constant blocks occuring with a minimum frequency of thirty times along a series. The meaning of the labels above and below in the x axes needs not to be unique, since several n-blocks with the same symbolic label can be originated applying different partitionings to a series. For instance, '000' is a block which in this analysis can be created with a binary to a quaternary partitioning, each dividing differently the phase space. Hence the color of the histogram bars is added. It is a representation of the most probable symbol following the depicted block, shown as an interval of colors from dark red to dark blue, as their optical wavelength increases, so that red can be the lowest and dark blue the highest value for a border of the bar standing for the expected symbol. Hence, for example, a histogram bar whose color varies between green and red represents the upper half of the symbolic space, or more specifically, a one of a binary partition ($'1\,p2'$). Consequently, the color of the histogram bar adquires the function of not only introducing the most probable symbol expected after an occurence of the analyzed n-block, but to specify the order of the partitioning. As a comparison, the symbol '2' of a tertiary partition covers from red to yellow, and the symbol '4' of a fifth-order partition is represented as a whole by dark red.

By comparing the frequencies of figure 3.14 with those of figure 3.12, it can be confirmed that the constancies of the anomalies series belong to the most frequent blocks of the 589 possibilities. The transitions, plotted in figure 3.16, for blocks with a minimum frequency of 20 events, take place much less frequently. In the case of the persistences, however, this is not true (figure 3.17), where the frequencies of the constancies are comparable to those of the transitions, especially for the SOI series. Thus the frequencies of the constancies and

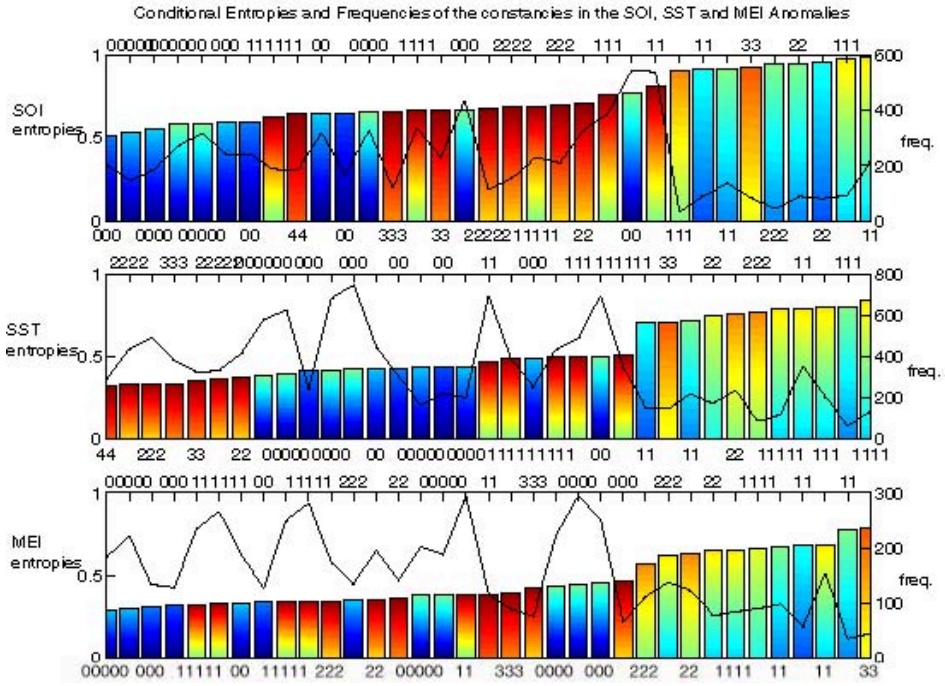

Figure 3.14: Conditional entropies of the constant blocks of the SOI, SST and MEI anomalies series. The entropies are depicted as bar plots and the frequencies of the blocks as the irregular curve. The color range of the bars denote the fraction of the series corresponding to the expected symbol after an occurence of the depicted block. The lower and upper x axes denote the blocks, the left y axis the entropies and the right y axis the frequencies.

transitions are an explanation for most of the time-evolution of the anomalies of the Southern Oscillation, which behave with slow dynamics for the partitionings performed. On the other hand, the faster dynamics of the fluctuations of ENSO given by the persistences allows for a better distribution of blocks representing constancies and transitions when applying symbolic dynamics.

Constancies of the SOI anomalies

For the anomalies of SOI, the blocks with the smaller conditional entropy are those of the extreme values of El Niño and La Niña. The constancies of this series begin with a group of seven blocks of relative low entropies, from 0.51 to 0.60, belonging to phases of El Niño given by the lower SOI values. The three most predictable blocks are $'000\,p4'$, $'00000\,p3'$ and $'0000\,p3'$, with uncertainties below 0.55, as can be seen in figure 3.14. Since these blocks correspond to blocks of zeros in a balance of the highest possible dynamical orders and the higher-order partitionings, this indicates that the best possible predictability in the series corresponds to the lowest thirds and quarters of the SOI index, with the longest possible knowledge of the series. The uncertainty in the determination of the symbol to come after one of these blocks has occured is in the range between 0.52 and 0.60, which is considerably high for the most predictable evolutions, and in all cases, tends towards a continuity of the state of El Niño. From there on, there is a large sequence of blocks in La Niña and El Niño states, whose conditional entropy grows continuously up to 0.70. Four of these blocks correspond to El Niño and ten to La Niña, and for all of them a constancy is similarly expected. The most predictable blocks of this group correspond to two La Niña states, this time from a large dynamical order or a fine partitioning: $'111111\,p2'$ and $'44\,p5'$. These blocks have a continuity as the most probable evolution as well and their conditional entropies are of 0.63 and 0.64. Conversely, three binary blocks, two of them with the shortest possible memory build the last section of El Niño and La Niña constancies with entropies between 0.76 and 0.81. After a large jump of the conditional entropies, values from 0.91 are introduced from the constant blocks which correspond to intermediate states between El Niño and La Niña. In spite of the high uncertainty associated to these blocks, it is found that for all of them, the most probable symbol to come remains equal to the value of

the preceding symbols.

Constancies of the SST anomalies

The Hadley Sea Surface Temperature data begin with a conditional entropy of 0.320 for the highest sea surface temparatures corresponding to El Niño, the block $'44'$ of the fifth-order partition. Its low conditional entropy is given by a probability of 0.86 for an evolution of the next symbol towards a continuity with the symbol '4', a probability of 0.13 for a '3' and probabilities under 0.01 for other transitions. The block $'2222\,p3'$ is the following as the conditional entropy increases, with is equal to 0.333. In this case the probability that the next block will continue with the value of '2' is of 0.89, while the probability for a transition to the symbol '1' is of 0.10. There is a total of other five blocks of low uncertainty, up to the entropy of 0.374, which represent solely El Niño states and forecast their continuity, without evidence for a correlation between their uncertainty and the dynamical or partitioning orders. In contrast, all the following 10 blocks belong to the class of La Niña and show conditional entropies which increase with decreasing dynamical order for all but the third-order partitioning. They begin with $'000000\,p2'$, which has an entropy of 0.382 and run up to the value of 0.442. Afterwards, blocks of the lowest partitioning orders appear, with conditional entropies between 0.472 and 0.507, where a large jump in the conditional entropy values occurs. The blocks of intermediate partitions, beginning with $'11\,p5'$, of conditional entropy 0.702 occupy again the final range of entropies in the plot. Interestingly there can be seen in the figure that the conditional entropy of these blocks grows from the edges of the series to its center and from the finer to the coarser partitions.

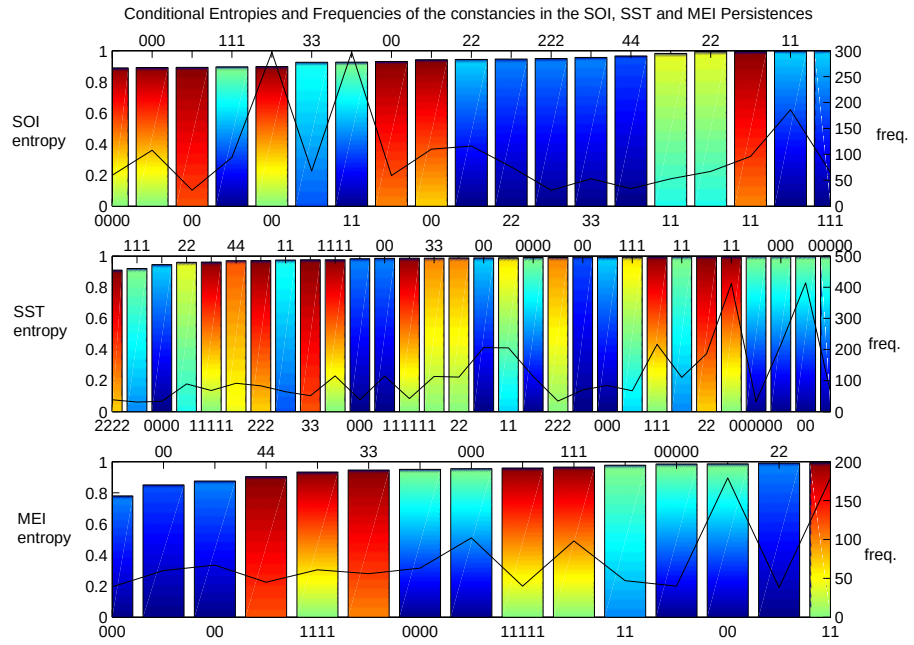

Figure 3.15: Conditional entropies of the constant blocks of the SOI, SST and MEI persistences series. The entropies are depicted as bar plots and the frequencies of the blocks as the irregular curve. The color range of the bars denote the fraction of the series corresponding to the expected symbol after an occurence of the depicted block. The lower and upper x axes denote the blocks, the left y axis the entropies and the right y axis the frequencies.

Constancies of the MEI anomalies

The plot of the constancies of the MEI anomalies series begins with four blocks of zeros, $'00000\,p3'$, $'0000\,p3'$, $'000\,p4'$ and $'00\,p5'$ indicating for this series a higher predictability starting from La Niña conditions. The conditional entropies of these blocks range from 0.29 to 0.32, and from their order of appearance, are possibly correlated with the length of the sequence known at the time of prediction and give as the expected symbol the same of the preced-

ing block. It is reassuring that the high predictability of these blocks cannot be reduced solely to length effects, as a look at the curve of the frequencies reveals. Then, two blocks of El Niño states appear, with their origins in a binary partition with large dynamical orders of 4 and 6. Their conditional entropies have values around 0.33, as for the following two blocks, which represent again La Niña states, in the second dynamical order and tertiary and quaternary partitions. From there on, the blocks of intermediate predictability consist of ten El Niño states with a smaller mean conditional entropy than the six neighbouring La Niña states, until the next jump in predictability at entropy of 0.47 takes place. Then, the block $'222\,p4'$, is found, representing with a conditional entropy of 0.57 the first intermediate block of any series with a somewhat sharp probability distribution for its immediate evolution. This block has a probability of 0.09 for a '1', of 0.77 for a '2' and 0.12 for a '3' to be the following symbol. The following eight blocks have conditional entropies between 0.62 and 0.69 and represent constant evolutions near an El Ninño or a La Niña and in the center of the series. As an example of the last, the block $'22\,p5'$ has an entropy of 0.66 and leads with probability of 0.62 to a '2', with 0.18 to a '1' and with 0.19 to a '3'. It is apparent that the conditional entropy increases as the blocks tends to the center of the series.

Constancies of the persistences

Figure 3.15 depicts the conditional entropies and frequencies of the constancies for the persistences series. It is first of all interesting that many blocks do not suffice the condition of sufficient frequency chosen in order to be included in the analysis, as several of the 35 possible constant blocks for each series occur less than thirty times. It is readily apparent that it is difficult to consider any block as a good starting point to make predictions, since the smallest conditional entropy of every series is considerably high. For the SOI series this

is of 0.89 and corresponds to the block $'0000\,p2'$. Due to the coarseness of the partition, this is, however, still a somewhat deterministic block with preferred probability for a transition to '1' with 70% probability. The next block corresponds to the sequence of fluctuations $'000\,p2'$, with a preference of 0.69%, similarly, for a transition to one. The block $'00\,p5'$ is more broadly distributed, since its corresponding probabilities for the symbols '0' to '4' are 0.06, 0.10, 0.13, 0.26 and 0.45, respectively. It can be then postulated the existence of an anticorrelation between the symbols in large blocks of constant fluctuations or after a large fluctuation with the expected symbol. This is not a strange result in light of the fact that for an oscillating series like ENSO, there is a limit on the number or intensity of fluctuations which take place in the same sense. The same behavior is observed for the blocks $'111\,p2'$ until $'22\,p3'$. The first intermediate constancy appears with the block $'33\,p5$ of entropy 0.93.

The constant blocks of the SST persistences begin with the minimum conditional entropy of 0.92 for the block $'111\,p4'$. The expected symbol is the '1' with a probability of 0.48; the next probability is 0.23 for a '3'. The following blocks are $'0000\,p3'$, $'22\,p5'$ and $'11111\,p2'$, with uncertainties between 0.95 and 0.97. For these blocks the expected development is a continuation of the constancy, with probabilities 0.48, 0.31 and 0.62 respectively. From here on, all the blocks have conditional entropies above 0.84. The most important characteristic of this series is that, in opposition to the SOI, there is a tendency to maintain the symbol of the preceding block. The only exceptions to this case are $'44\,p5'$, $'33\,p5'$ and $'44\,p4'$. The dynamic behavior of the MEI persistences is similar. One finds here the block with the least uncertainty, $'000\,p4'$, with a conditional entropy of 0.78 and the preferred probability of 0.62 for a continuity towards a large negative fluctuation. Two blocks follow with the same behavior and conditional entropies of 0.85 and 0.88, $'00\,p5'$ and $'00\,p4'$. For these blocks the expected constancy of the symbol occurs with a probability of 0.5. The following three blocks represent fluctuations in the positive direc-

tion with conditional entropies over 0.9 and the series of blocks continues only with the extreme constant events of the different partitionings. Hence, albeit affected by many blocks without enough frequency, the MEI anomalies series shows the fluctuations with the most definite distributions for the forthcoming symbol.

3.4.3 Conditional entropies of the transitions

The condition of significance

In the study of the transitions, it is useful to introduce a methodic difference in the selection of the blocks. Since there are 554 possible transitions in contrast to the 35 possible constancies, the frequency of their appearance is reduced, especially in the most deterministic and shortest series. Hence, the threshold of thirty events has been reduced to twenty, to allow the observance of the entropies obtained from the MEI series Additionally, a significance test will be introduced for selecting the blocks whose entropy is less likely to be a consequence of chance. This is an important detail which deserves more attention.

The significance introduced here is an important descriptor of the entropies of the blocks, since it points out the mean difference between the conditional entropies of blocks of the ENSO sequences and those of blocks of random sequences without correlations. As there is no known expression for the distribution of the conditional entropies, this is a way to explore the most meaningful conditions for a prediction. To this end, 100 surrogate sequences were created to simulate the three ENSO quantifiers as random processes with the same transition probabilities after the occurence of one symbol. An estimate of the extent to which the predictability of a block of one measured ENSO sequence could be attained by chance can be computed by comparing the conditional

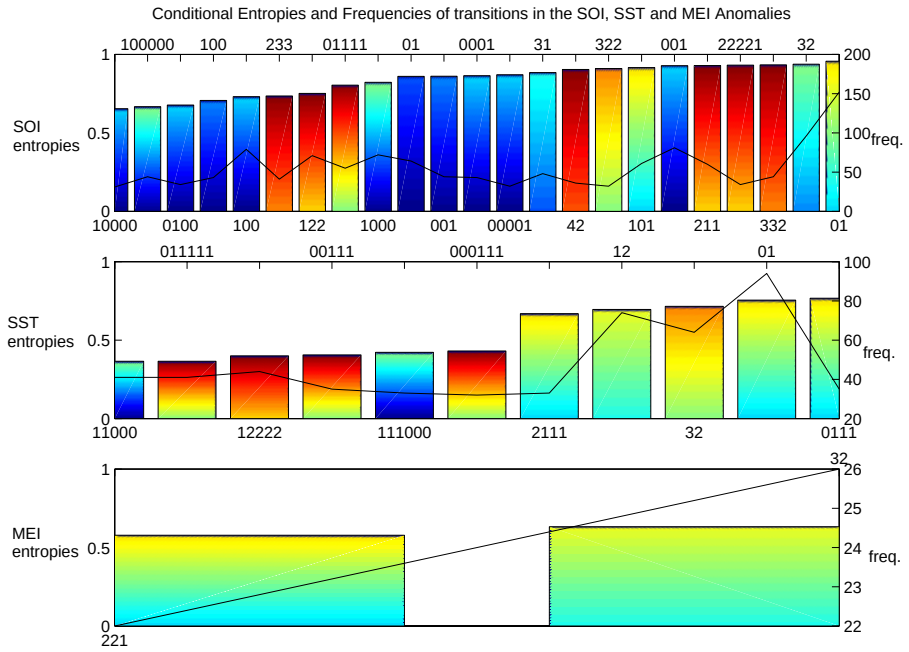

Figure 3.16: Conditional entropies of the transition blocks of the SOI, SST and MEI anomalies series. The entropies are depicted as bar plots and the frequencies of the blocks as the irregular curve. The color range of the bars denote the fraction of the series corresponding to the expected symbol after an occurence of the depicted block. The lower and upper x axes denote the blocks, the left y axis the entropies and the right y axis the frequencies.

entropies of the measured sequence with the mean conditional entropy of its surrogates $< h_{s_n} >$. The significance $s_n(x)$ of the n-block x is then defined as

$$s_n(x) = \frac{h_n(x) - < h_{s_n}(x) >}{\sigma^2_{s_n}(x)}, \tag{3.2}$$

Thus, if the significance is a negative value, it means that the conditional entropy of the measurements is smaller than the mean conditional entropy of the surrogates for a block x, so that the predictability is more likely to be a

result of time correlations in ENSO than to be given by chance. Assuming that the conditional entropies of the surrogates are gaussian distributed, it is possible to estimate the probability for a conditional entropy of being a true indicator of structure. This assumption is nevertheless not obvious [97] and will be avoided in this work. The surrogate series analysis will be applied hence primarily to select the relative amount of information given by a block and to complement the condition of sufficient frequency.

Transitions of the anomalies and persistences

It can be expected for the blocks denoting transitions of the indices of ENSO to be a considerably difficult set, since most of the anomalies occupy constancies and most of the persistences have very high conditional entropies. Figures 3.16 and 3.17 show the conditional entropies and frequencies of these blocks, whose significance exceeds -1 towards $-\infty$ and whose frequency exceeds the threshold for its originating series. It is found that the SOI series has the largest number of blocks which satisfy these conditions, and that the effect of the short length of the MEI series reduces almost entirely its utility.

The transitions of interest of SOI consist of 23 blocks beginning with $'10000\,p3'$, of entropy 0.65 and significance -2.0. This is the first of five blocks which consist of transitions to a state of El Niño, which then assumes the role of an attractor. This series of blocks indicates that the transition $'10000\,p3'$ and the fluctuation from El Niño to an intermediate state and back $'0100\,p3'$ are more predictable than the transition in the shorter time $'100\,p3'$. The same occurs with the blocks $'100000\,p2'$ and $'1000\,p2'$ later. The attractor of La Niña states is apparent in the following three blocks, where the partitioning order decreases as the entropy increases. A transition towards a higher La Niña is then more predictable and stable the higher the reached state is. The transitions from El Niño towards an intermediate state are characterized by

a instability which drives the SOI back. This is illustrated with the series of four blocks ending in '1'. Of these, the blocks $'0001\,p3'$ and $'00001\,p3'$ show very similar uncertainties, meaning that there is no information difference by knowing that the atmosphere has been in El Niño three or four months before going to an intermediate state. From here on, there are only four blocks which attest that the last symbol will be the most probable. On the other hand, some transitions are to be interpreted as fluctuations as $'42\,p5'$, which returns with a slightly higher probability to '4' than to '2' or '3'. Here the high uncertainties are again reached, that prevent and these prevent the following blocks from having a sharply defined expected value.

The SST anomalies show the most interesting predictabilities, for they present the smallest conditional entropies of all the possible transitions. The blocks of the smallest conditional entropy, as presented in figure 3.16 pertain primarily to low-order partitions showing strong mid-range correlations, with conditional entropies between 0.37 and 0.43. The distributions of the following symbol are considerably sharp, as the probabilities for a constancy following the blocks $'11000\,p2'$ and a $'011111\,p2'$ are of 0.95 and for the block $12222\,p3'$ is 0.91. Mid-range correlations are however not evident, as there are blocks of higher order which have greater conditional entropies than smaller blocks which are identical to their ends. Following this series of blocks, there is another one corresponding to intermediate states with uncertainties beginning at 0.67. The first of them $'2111\,p3'$ has a probability of 0.79 of continuing to a '1' and is an example of a relatively predictable intermediate state. Not very different are the following blocks, where a finer phase space is prefered to correlations over larger time scales. The MEI series show only two transitions to intermediate states, of conditional entropies 0.58 and 0.63. It appears that the shortness of the series is the most important obstacle for a useful investigation of its transitions.

The case for the persistences is dominated by huge uncertainties. Only the

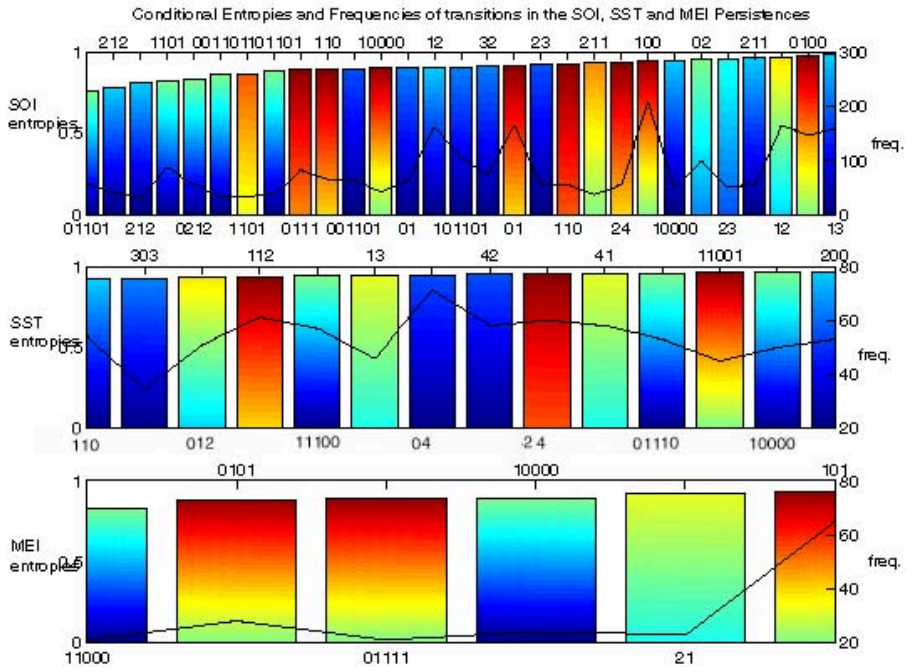

Figure 3.17: Conditional entropies of the transition blocks of the SOI, SST and MEI persistences series. The entropies are depicted as bar plots and the frequencies of the blocks as the irregular curve. The color range of the bars denote the fraction of the series corresponding to the expected symbol after an occurence of the depicted block. The lower and upper x axes denote the blocks, the left y axis the entropies and the right y axis the frequencies.

SOI series show conditional entropies below 0.8, for the erratic series $'01101\,p2'$. With a probability of 0.79 of returning to a cold system and a significance of -2.54 it is a block of relatively well-defined evolution which cannot be easily produced with an uncorrelated process. The uncertainties for this series grow as a stair function until there is a plateau at the conditional entropy 0.86. For the MEI series there are six blocks of conditional entropies between 0.83 and 0.94, while for the SST, the most predictable blocks begin with 0.92.

Chapter 4

Wavelets and temporal structure of the observed data

Wavelet analysis has become in the last decade a useful method to study the temporal structure of time series. By decomposing a time series into the time-frequency space, this method makes possible to determine both the dominant modes of variability and how those modes vary in time of the series. In this way, it also allows detailed analyses of the structure of time seeries. In this chapter wavelet analysis will be applied to analyze the variability in the time, i.e. the periodicities, of the three indices of the Southern Oscillation, and to test their difference to white noise over their whole span of time.

4.1 Wavelet analysis

The range of application of wavelet analysis has grown recently from the fields of engineering and pattern reconstruction to earth and planetary sciences and general time series analysis. In short, wavelet analysis consists of

the decomposition of a time series into variability patterns in time and frequency. Some of the work on wavelet analyisis has been objected because of this diffusing character: a wavelet transform changes a one-dimensional time series into a two-dimensional time-frequency image. This difficulty has been recently overcome as significance tests for wavelet transforms have been developed [114]. Beyond any discussion, it is innegable that wavelet analysis is one of the most succesful tools in analyzing the intensity in the time of a time series and that it gives much more information than Fourier analysis in the analysis of periodicities. It allows a study of the stationarity of the series, or conversely, for stationary time series, wavelet analysis allows for high-resolution studies of the structure of the series. In the contexts of climatology and geophysics, interessant results with the application of this method have been found for time series of temperature in central England [4], tropical convection [130] and dispersion of waves [68]. A general introduction to wavelets can be found in [21], or in the context of climatological time series, in [60].

El Niño and the Southern Oscillation have been also investigated using wavelet analysis [65, 124, 127]. Some of the most important results from these works are the quantification of the relative strength of the different periodicities, in the interdecadal, decadal and bidecadal time scales, and the resolution of the frequencies which are directly related to the larger El Niño events since 1960. Correlations between the SOI index and an SST-type variable have also been thoroughly studied in the reference [65]. Several of the mentioned properties of ENSO will appear naturally in the results of this chapter. Particularly new is, to the best knowledge of the author, the first wavelet analysis of the MEI Index and, following [76] a study of the processes underlying the onset of El Niño or La Niña.

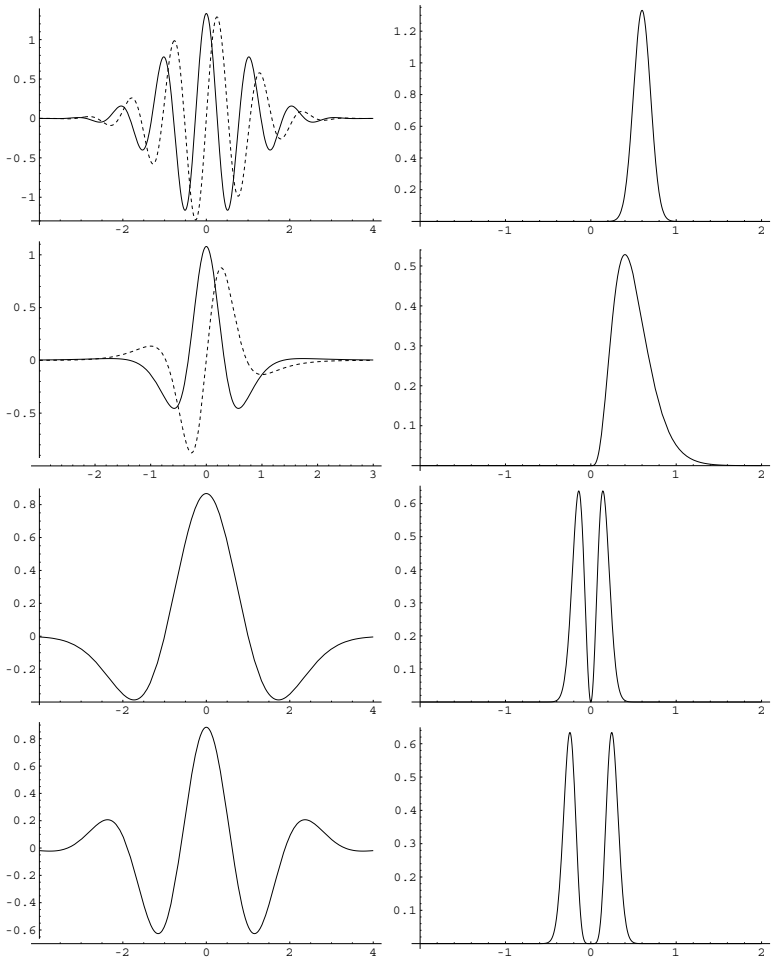

Figure 4.1: Form of four different wavelets. The left panels show the wavelet functions in time domain, where their imaginary parts are dot-dashed. The right panels show the same wavelets in the frequency domain. The wavelets shown are (from top to bottom) Morlet, Paul (order $m = 4$), DOG ($m = 2$) and DOG ($m = 6$).

4.1.1 Wavelet functions

The wavelet transform is based on a *wavelet function* $\psi(\xi)$ that depends on the nondimensional timelike parameter ξ. The wavelet function represents a wave which is localized in time and frequency, acting as a bandpass filter over the time series. Consequently, another condition for the wavelet function is that should have zero mean. Some common wavelet functions are depicted in figure 4.1. As can be seen in this figure, it is possible to employ real or complex wavelet functions. It is similarly possible to employ functions derived from an orthogonal basis or simply nonorthogonal wavelet functions. Functions from an orthogonal basis imply the use of a discrete wavelet transform [62], while nonorthogonal wavelet functions can be used with either continuous or discrete wavelet transforms. Orthogonal wavelet analysis is appropriated for signals in which discontinuous variations are expected, so that this study will restrict to the use of nonorthogonal wavelets. The expressions for the wavelet functions of figure 4.1 is given in table 4.1.

From the functions of figure 4.1, the Morlet and Paul wavelets are complex and the DOGs (derivatives of the gaussian) are real for any order. Complex wavelet transforms return information about amplitude and phase of the signal and are especially useful for oscillating series. Real wavelet transforms return only a single component and can be used to isolate peaks or discontinuities. The shape of the wavelet function is similarly important, since this should reflect the type of features present in the time series. Defining the width of the wavelet function as the e-folding time of the wavelet amplitude, the resolution of a wavelet function is determined by the balance between its width in time and frequency. As these variables are complementary, a function which is narrow in time will have good time resolution but poor frequency resolution, while a function which is broad in time will have poor time resolution, yet good resolution in frequency. Hence, when the information in both time and

Name	$\psi(\xi)$	$\hat{\psi}(\omega)$
Morlet (ω_0 = frequency)	$\pi^{-1/4} e^{i\omega_0 \xi} e^{-\xi^2/2}$	$\pi^{-1/4} H(\omega) e^{-(s\omega-\omega_0)^2/2}$
Paul (m = order)	$\frac{2^m i^m m!}{\sqrt{\pi(2m)!}}(1-i\xi)^{-(m+1)}$	$\frac{2^m}{\sqrt{m(2m-1)!}} H(\omega)(s\omega)^m e^{-s\omega}$
DOG (m = derivative)	$\frac{(-1)^{m+1}}{\sqrt{\left(m+\frac{1}{2}\right)}} \frac{d^m}{d\xi^m}\left(e^{-\xi^2/2}\right)$	$\frac{-i^m}{\sqrt{\Gamma\left(m+\frac{1}{2}\right)}}(s\omega)^m e^{(-s\omega)^2/2}$

Table 4.1: Table of three wavelet functions in time and frequency domain. DOG means Derivative of the Gaussian, $H(\omega)$ is the Heaviside step function, $H(\omega) = 1$ if $\omega > 0$, $H(\omega) = 0$ otherwise. Here $\xi = t/s$ is the transcurred time in a defined time scale (for instance, δt or a product of it), so that the Fourier transform depends on $s\omega$.

frequency is interesting, as in a general survey of the Southern Oscillation, an intermediate wavelet function is appropriated. For this purpose the Paul wavelet function of figure 4.1 has been chosen.

4.1.2 Wavelet transforms

Given a discrete time series $X = x_0, \ldots, x_{N-1}$, where $n = 0, ..., N-1$ are equally spaced intervals of time with difference δt, the *continuous wavelet transform* is approximated as the convolution of X with the complex conjugate of the wavelet function $\psi(\xi)$. The wavelet function used in this case is a *displaced and scaled* function, in order to let it act over the whole span of the time series in several scales related to the Fourier frequencies. Denoting the displacement parameter as n' and the scale as s, the wavelet transform of the time series at the point n takes the form

$$W_n(s) = \sum_{n'=0}^{N-1} x_{n'} \psi^* \left(\frac{(n-n')\delta t}{s} \right), \tag{4.1}$$

where the displaced and scaled variable substitutes the parameter ξ. The wavelet transform can be similarly found in Fourier space, by taking the discrete Fourier transform of the time series

$$\hat{x}_k = \frac{1}{N} \sum_{n=0}^{N-1} x_n e^{-2\pi i k n/N} \tag{4.2}$$

and applying the convolution theorem. Since in the continuous limit, the Fourier transform of a function $\psi(t/s)$ is given by $\hat{\psi}(s\omega)$, the wavelet transform is given by the inverse Fourier transform of the product of $\hat{x}_k$ and $\hat{\psi}(s\omega)$,

$$W_n(s) = \sum_{k=0}^{N-1} \hat{x}_k \hat{\psi}(s\omega) e^{i\omega_k n \delta t}, \tag{4.3}$$

where the angular frequency is defined as

$$\omega_k = \begin{cases} \frac{2\pi k}{N\delta t} & \text{for} \quad k \leq \frac{N}{2} \\ -\frac{2\pi k}{N\delta t} & \text{for} \quad k > \frac{N}{2}. \end{cases} \tag{4.4}$$

This representation of the continuous wavelet transform is particularly useful, since it can be therefore computed (for a given s) at all n simultaneously and efficiently. It should be noted that the scale s does not correspond necessarily to a Fourier frequency of s^{-1}. Meyers and coworkers [68] developed a method to derive the *equivalent Fourier period* analytically from a wavelet scale, so that it is possible to transform the scales of the wavelet transform to Fourier periods. The Fourier periods for the wavelet functions of table 4.1 are given in table 4.2.

Name	Equivalent Fourier Period
Morlet (ω_0 = frequency)	$\frac{4\pi s}{\omega_0+\sqrt{2+\omega_0}}$
Paul (m = order)	$\frac{4\pi s}{2m+1}$
DOG (m = derivative)	$\frac{2\pi s}{\sqrt{m+\frac{1}{2}}}$

Table 4.2: The Fourier equivalent frequencies for the Morlet, Paul and Derivative of the Gaussian

For the complex wavelet transforms, obtained with complex wavelet functions, the *wavelet power spectrum* is $|W_n(s)|^2$. To make comparisons between power spectra of different time series, the power spectra must be normalized. A good choice is to normalize the expectation value of the spectrum with the expectation value of a white noise process. For wavelet functions which satisfy the condition

$$\int_{\infty}^{\infty} |\hat{\psi}(\omega')| d\omega' = 1, \tag{4.5}$$

at each scale the sum over the N points of the time series will equal N:

$$\sum_{k=0}^{N-1} |\hat{\psi}(s\omega)|^2 = N. \tag{4.6}$$

Consequently, the expected value of $|W_n(s)|^2$ according to equation (4.3) is equal to N times the expectation value for $|\hat{x}_k|^2$. Since for a white-noise time series this expectation value is σ^2/N, where σ is the variance, then the expectation value for the wavelet transform of a series of white noise is $|W_n(s)|^2 = \sigma^2$ at all n and s. Hence, expressing the wavelet power spectrum as $|W_n(s)|^2/\sigma^2$,

the wavelet transform measures the power relative to white noise, so that it can be compared for all indices of the Southern Oscillation.

4.1.3 Length effects

Since the wavelet transform is an operation over a time series which takes place over several window lengths, it is convenient to make the series compatible so that the transform can be defined over the whole time interval of the series for any width s. Moreover, it is required by the Fourier transform (equation (4.2)) that the data be cyclic and it is desired on computational grounds that the length of the time series be an integer power of two. Hence, it is useful to extend the time series in order to let their first and last element be equal and let its length be a power of two. A method to achieve this is to pad with zeroes the edges of the series. This procedure introduces a discontinuity at the edges and decreases the wavelet amplitude near them as more zeroes enter the analysis.

A way of quantifying this effect is by computing the decorrelation times of the wavelet power at each scale. This quantity allows to measure not only the effect of the discontinuity at the edges of the series, but also to discriminate single spikes in the time series. The *cone of influence* is hence defined as the e-folding time for the autocorrelation of wavelet power at each scale. This e-folding time is chosen so that the wavelet power for a discontinuity at the edges drops by a factor of e^{-2} and ensures that the edge effects are neglibigle beyond this point. At the same time, the proportion of the cone of influence quantifies the effect of the finite length of the time series. The region under the line of the cone of influence as depicted in figures 4.2 to 4.7 is consequently affected by the finite size of the series of the Southern Oscillation.

4.2 Wavelets and the process underlying a time series

As has been seen above, the normalized Fourier power spectrum of a time series is given by $N|x_k|^2/\sigma^2$, where N is the number of points of the series, x_k is given from equation (4.2) and σ^2 is the variance of the time series. Now let Y be a time series $y_0, \ldots, y_{N-1}$ which is normally distributed. Since y_n is a normally distributed random variable, both the real and imaginary parts of y_k are normally distributed [89]. Moreover, since the square of a normally distributed variable is χ^2-distributed with one degree of freedom, then $|y_k|^2$ is χ^2-distributed with two degree of freedom (χ^2_2).

With this result, it is possible to assign significance levels to the power spectra obtained from any process which gives gaussian-distributed random variables with any correlations in the time. For example, when P_k is the Fourier power spectrum, then it is possible to write the distribution for its values:

$$\frac{N|x_k|^2}{\sigma^2} \quad \text{is distributed as} \quad \frac{1}{2}P_k\chi^2_2 \tag{4.7}$$

where the 1/2 is introduced as a consequence of the additional degree of freedeom. This expression can be illustrated with a gaussian white-noise process — which has a Fourier power spectrum which is flat and is normalized to one. Consequently, a peak in the power spectrum of a time series would be evidence with the significance α for other structure than white noise if it surpasses the $1-\alpha$ percentile of (χ^2_2). This would signify that the spectrum of the time series does not correspond, with the probability $1-\alpha$, to that of a white-noise process.

More interesting is the case of a Markov or red noise process. The most simple of this class of processes, the autoregressive process of first-order

$$y_n = a y_{n-1} + \eta_n, \tag{4.8}$$

where a is a constant, $y_0 = 0$ and η_n is taken from Gaussian white noise, has the normalized discrete Fourier power spectrum

$$P_k = \frac{1 - a^2}{1 + a^2 - 2a\cos(2\pi k/N)}, \tag{4.9}$$

where $k = 0, \ldots, N/2$ is the frequency index. Hence, a time series which has, with probability $1 - \alpha$, larger correlations than this Markov process, should have at least one peak which is higher than the product of the power given by equation (4.9) at the same frequency times the $1 - \alpha$ percentile of (χ_2^2).

The time resolution of the wavelet power spectra can be used in this context by finding the wavelet transform for a definite process at any given time. This can be achieved with Monte Carlo techniques, and with them has been found [114] that the wavelet power spectrum at any given time for first-order autoregressive processes is well-described by equation (4.9). Thus, for complex wavelet functions, eq. (4.7) applies and

$$\frac{N|x_k|^2}{\sigma^2} \quad \text{is distributed as} \quad \frac{1}{2} P_k \chi_2^2, \tag{4.10}$$

while for real wavelet functions a χ^2 distribution with one degree of freedom applies so that

$$\frac{N|x_k|^2}{\sigma^2} \quad \text{is distributed as} \quad P_k \chi_1^2, \tag{4.11}$$

It has been seen in the foregoing chapter that surrogate time series analysis is not very useful for analyzing the indices of the Southern Oscillation, since the chance of any of the indices of the Southern Oscillation of not being possibly modeled with a white noise process is small. However, there is the

possibility of obtaining positive results when testing with the time-resolved wavelet transforms. It is of special interest to search for the *intervals of time* where the memory of the time series is more likely to be different to that of a white or red noise process.

4.3 Wavelet spectra of the ENSO Indices

The wavelet power spectra give a detailed explanation in the time where the periodicities are present, having different intensities along the length of the time series. We have analyzed this periodicities for the ENSO indices with the Paul wavelet function ($n = 2$) and compared the duration of the time intervals where periodic behavior is most present, as well as the frequencies and intensities of the periodicities. It was possible to test for the differences between the wavelet spectra of the measurements and that of the autocorrelation first-order Markov process for the anomalies series, while for the persistences series, interesting results were achieved by searching for the regions significantly different from white noise.

4.3.1 Wavelet power spectra of the anomalies series

Figure 4.2 shows the periodicities in the time of the SOI anomalies series. It appears that for this series, there are strong periodicities of three to seven years, which are present over most of the length of the time series. There are two exceptions to this behavior, between 1924 and 1937 and between 1962 and 1966, while regions of larger periods have been active in the last three decades. These intervals have been observed to account for a shift in the correlation lag between SOI and SST and to start the trend of larger El Niño events which has peaked in the last two decades.

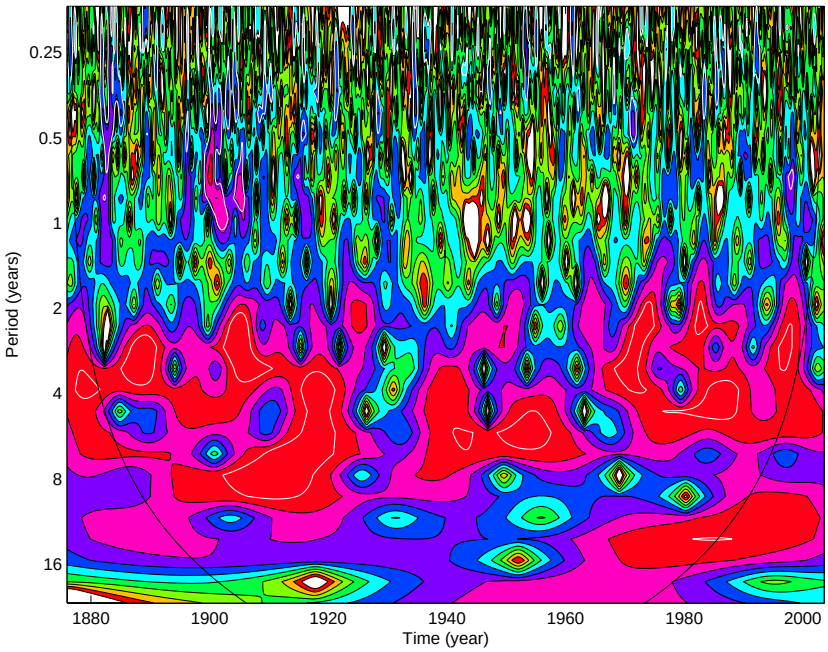

Figure 4.2: Paul wavelet power spectrum of the SOI anomalies series. The concave line below is the cone of influence, where finite-size effects underestimate power. The white contours indicate significant regions of different structure than the autocorrelation first-order Markov process.

For periods smaller than two years, the patterns are irregular and of smaller intensity than for the strongest interdecadal periods. Much of these signals represent effectively noise as was observed in the Fourier spectra of the last chapter. Length effects are of importance for this series in periodicities smaller than ten years between 1895 and 1995, as can be seen from the black curve representing the cone of influence. There are some regions, inside the patterns for the largest periodicities, which represent areas with a significant difference to an autocorrelation first-order Markov process simulating the series.

The wavelet power spectrum of figure 4.3, for the SST anomalies series,

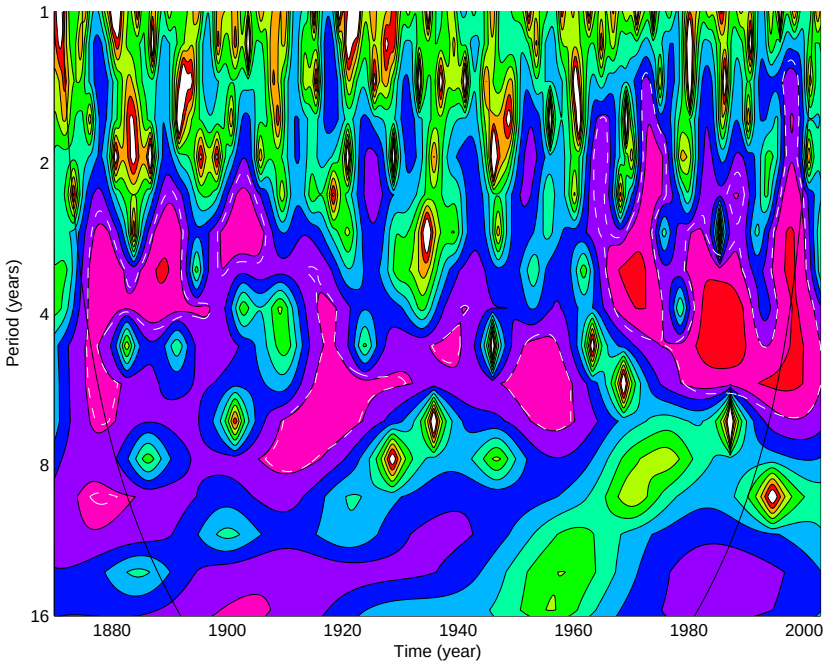

Figure 4.3: Paul wavelet power spectrum of the SST anomalies series. The concave line below is the cone of influence, where finite-size effects underestimate power. The white contours indicate significant regions of different structure than the autocorrelation first-order Markov process.

is evidently affected by high-frequency random disturbances. The regions of strong periodicities are found to be larger than for the SOI anomalies series, showing only the interruption around 1960. In the last decades, moreover, strong periodicities of higher frequency have taken place, so that a shift in the frequencies appears to have occured since the begin of the record. This shift enlightens considerably the search for mechanisms which are sought to be responsible for the variability of ENSO in the past half century. The length effects are similar to those of the SOI anomalies, but the significant regions are by far much larger. It is found that these areas occupy more space than

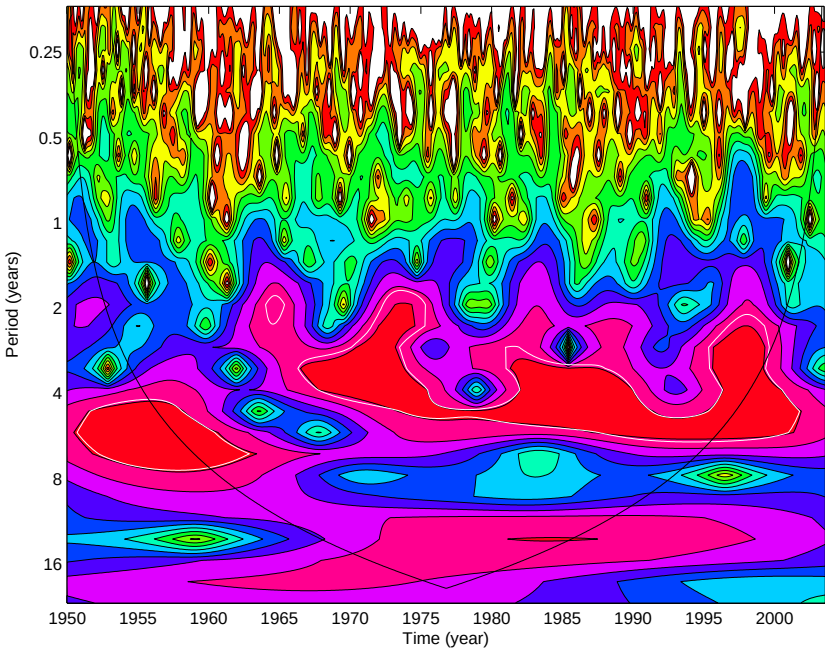

Figure 4.4: Paul wavelet power spectrum of the MEI anomalies series. The concave line below is the cone of influence, where finite-size effects underestimate power. The white contours indicate significant regions of different structure than the autocorrelation first-order Markov process.

five percent of the plot, the limit which could have been given by chance, so that this series has been significantly under the action of correlations, especially from 1880 to 1930 and since 1960. Another argument for the positive evaluation of correlations is the localization of the significant areas: these are not likely to have the forms they take by chance.

The wavelet power spectrum of the MEI anomalies series is shown in figure 4.4. This plot appears as a detail of the wavelet power since 1950, and consists primarily of three large regions of acting periodicities. It is necessary to considerate only the smallest periods, which reach their maximum of 16 years

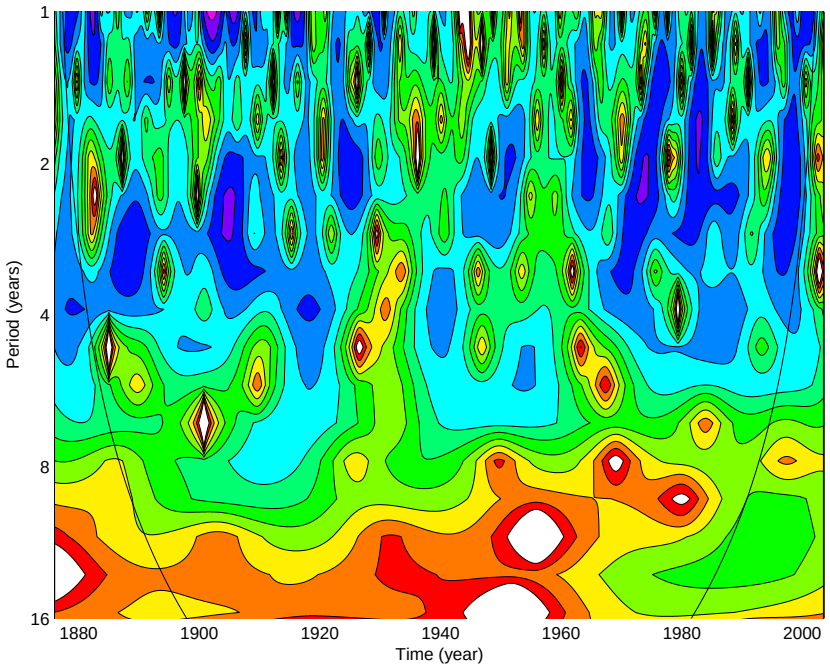

Figure 4.5: Paul wavelet power spectrum of the SOI persistences series. The concave line below is the cone of influence, where finite-size effects underestimate power. The white contours indicate significant regions of different structure than white noise.

in 1976, for the size of the series allows for large areas of length effects. The largest region of strong influence on ENSO has a periods between 2 to 4 years and is found between 1965 to 2000. Before 1965, a region of larger periods between 4 and 8 years appears. Hence, the MEI series confirms the importance of the shift in the acting frequencies in the evolution of ENSO in the sixties. The third region of periodicities over the scale of a decade are found mostly below the cone of influence, nevertheless it coincides with the appearence of a similar region for the SOI series.

As for the SST, most of the regions of greater variance in the interdecadal

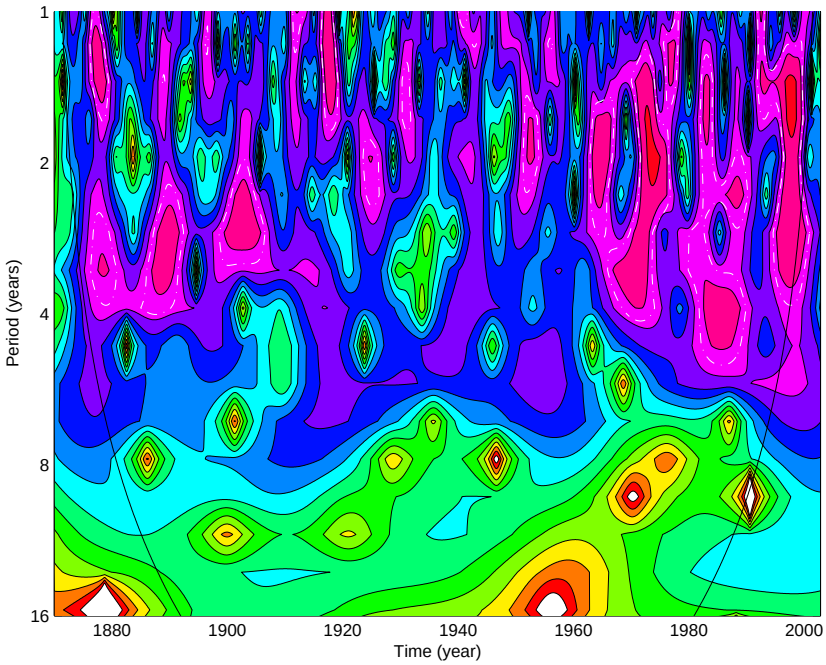

Figure 4.6: Paul wavelet power spectrum of the SST persistences series. The concave line below is the cone of influence, where finite-size effects underestimate power. The white contours indicate significant regions of different structure than white noise.

scale are found to differ from the most similar first-order Markov process. From the MEI series, it appears that practically the last half century presented mid-range correlations.

Many of the apparently non-Markovian areas of the SOI are found to be the events where mid-range correlations take place, which have been found as constant blocks during El Niño or La Niña state. The most prominent of these episodes are found between 1900 and 1920, as in the large episodes between 1965 and 1998. In the case of SST, there are larger continuous areas suggesting non-Markovian behavior. The results of the MEI index support this

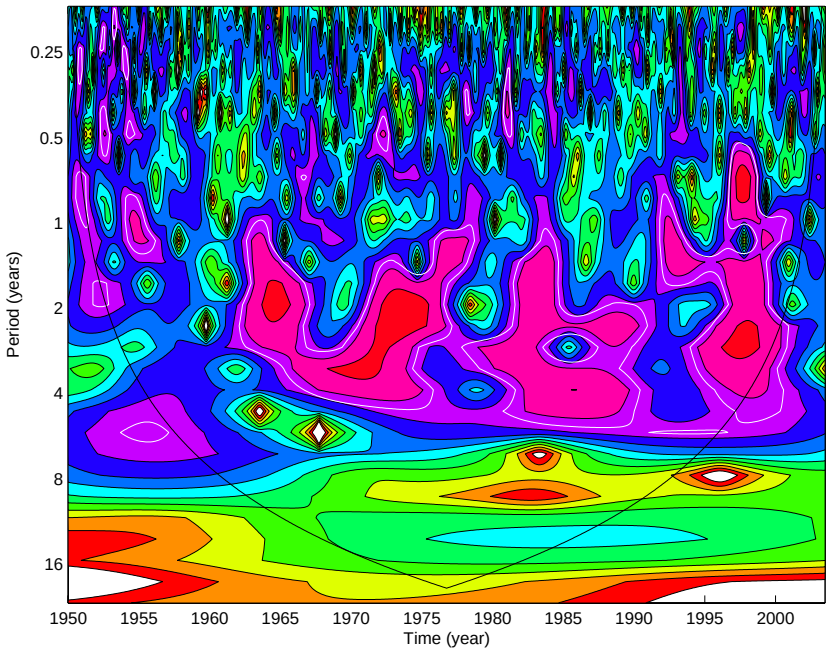

Figure 4.7: Paul wavelet power spectrum of the MEI persistences series. The concave line below is the cone of influence, where finite-size effects underestimate power. The white contours indicate significant regions of different structure than white noise.

conjecture. This approach is an interesting argument in the development of coupled models which show a larger correlations in their oceanic than in their atmospheric parts.

4.3.2 Wavelet power spectra of the persistences series

The wavelet power spectra of the persistences series are, as expected, much less regular than those of the anomalies series. It is in this light understandable that it is more appropriate to look for areas of significant different power with respect to a white noise series than with respect to a Markov process. This

approach reveals more clearly the differences between the three indices of the Southern Oscillation, as will be seen below.

The wavelet power spectrum of the SOI persistences series, shown in figure 4.5, is evidence for a meager information content in the fluctuations of this index. It is difficult to define periods which are particularly important in the series, as it is for an evolution in the time which is related to the cold and warm phases of the Southern Oscillation. There are no areas found, whose variance with respect to that of white noise could appear as evidence for a more complex structure with probability 0.95.

Figure 4.6 shows a strikingly different picture for the SST series. Now there are some regions with their largest intensities taking place approximately every five to ten years, depending on the decade. These are present at the same time when the wavelet spectrum of the anomalies indicate a strong event. The frequencies of these periodicities are between 1 and 4 years and reveal a localized difference to white noise which is significant during the largest events in persistences and anomalies. Consequently, it is possible to associate the most prominent peaks in the SST anomalies series with coherent periodic fluctuations occuring at higher frequencies. Since during these episodes most of the constant blocks with enhanced predictability occur, it is possible to relate this increase in predictability with a correlation between anomalies and fluctuations of the SST, which is not present in SOI .

A considerably similar picture is obtained by taking the wavelet transform of the MEI series (figure 4.7). There are large similitudes between the spectrum of this series and SST, as three regions of largest intensity are present, which differ well over the five percent allowed by chance from a white noise series. This suggests that the inclusion of variables other than SST which are taken into account in the derivation of MEI are not of relevance for the form of the distribution of frequencies acting in an El Niño or La Niña. The MEI index is

largely affected by length effects in the description of the Southern Oscillation in the analyses of the present work and does not additional reliable information than the sea surface temperature in the region Niño 3.

The wavelet method hence is useful to verificate that the regions of highest predictability are associated with i) the states during the most prominent El Niño and La Niña events, ii) constant evolutions, and that iii) the anomalies series allow for a succesful discrimination of ENSO from red noise while the ENSO persistence series can barely differ from a white noise process. Additional results of interest are the finding of the regions since 1870 where the Southern Oscillation calms and acts primarily as noise, and the possible elevation of the frequencies taking place in the oscillations in sea surface temperature.

Chapter 5

Conclusion

In this work, methods of information theory and wavelet analysis have been applied to investigate the predictability properties of indices of the climatic variability in the tropical Pacific known as El Niño-Southern Oscillation (ENSO). Moreover, these techniques have allowed to compare the properties and potential utility of the indices of the ENSO phenomenon. The indices which have been studied are: the Southern Oscillation Index [116], the sea surface temperature (SST) from the Hadley Center for Climate Prediction and Research [92], and the Multivariate ENSO Index [133], all on a monthly basis.

With the analysis of the Shannon entropies of symbolic sequences of the departures from the climatological mean (anomalies) of the indices of ENSO it has been found that the average predictability with an optimal binary (warm/cold) partition is highest for the MEI series and lowest for the SOI series. On the other hand, the predictability of the fluctuations (persistences) of the three indices of the Southern Oscillation, (divided in the space large/small), are extremely unpredictable even knowing the past five months in advance, as their Shannon entropies do not attain levels below 0.95 and for any value up

to five of the dynamical order. This picture changes with the introduction of a terniary partition (warm/ neutral/ cold), for the predictabilities are apparently enhanced by increasing the dynamical order in two cases: i) for the anomalies of the SOI series and ii) for all the persistence series. The effect of the finite size of the series is still a factor not to be neglected; nevertheless, there is evidence for a real structure detection and enhancement of the predictability in the SST and SOI anomalies series, supported from the usage of the Bayesian probability measure, and the asymmetrical decrease of the entropies. In the case of the MEI series, additional caution with the results is required, for the entropies at the highest dynamical orders cannot be regarded as reliable.

An investigation of the events, in the form of symbolic blocks, which correspond to the conditions of the highest predictability of the Southern Oscillation has been addressed in this work. The analysis shows that the blocks with the least uncertainty correspond principally to those of the highest frequency in the anomalies series. A comparison between the anomalies of ENSO additionally reveals that the space of the n-blocks is best exhausted with the optimal partitions of the SOI series and least exhausted with those of the MEI series. Nevertheless, it is found that there is a negative interplay between the values of the lowest entropies and the amount of the blocks which is occupied by a series. The quantitative analysis of these interactions leads consequently to postulate that the SST anomalies series, which is intermediate in the proportions of occupied blocks and smallest entropies, is the most useful in the prediction of the evolution of the Southern Oscillation in an arbitrary moment. The analysis of the persistences series of the indices of the Southern Oscillation gives a less promising picture. For all persistence series, the most predictable blocks are not correlated with the most frequent ones and the entropy distributions are extremely skewed to one.

The analysis of the symbolic dynamics of the indices of the Southern Oscillation reveals another important difference between the series of the anomalies

and persistences. In the case of the anomalies, the most frequent blocks are those which denote a constant evolution of the phenomenon along the whole length of the predicting block. Since for the anomalies series, the most frequent blocks are generally those with the smallest entropies, this allows to classify the most predictable sequences as *constancies*, the evolutions of a constant state. The series of the persistences, on the other hand, do not allow to recognize a definite class of the most frequent or most predictable fluctuation sequences.

A more detailed study of the predictability of the constant blocks reveal that the most probable states of the SOI anomalies correspond to El Niño. The most predictable blocks consist are attained in a balance between the highest length possible for the analysis and the finest partitioning. While the evolution after states corresponding to La Niña are less predictable, the blocks corresponding to the intermediate states reach by far the highest uncertainties. Similarly, the most predictable blocks of the SST anomalies series are those of El Niño states. The predictability for this series is considerably better, with seven blocks of entropies betwee 0.32 and 0.37. The La Niña states follow with entropies between 0.38 and 0.44. The starting entropy for the neutral states is of 0.70. For this series in the El Niño states, there is no apparent correlation between the predictability and the memory of the symbolic sequence, while for La Niña, this is more likely to be the case. The neutral states appear to be most uncertain towards the center of the range of the time series. Opposite to the former results, the blocks with the higher predictability of the MEI anomalies series correspond to states of La Niña. The lowest entropies of all the series are found in this series, beginning at 0.29 in blocks satisfying a criterium of minimum statistics. Similarly, the blocks denoting neutral states are most predictable within this series, with entropies from 0.57. Possible correlations appear after La Niña states, since the predictability increases with the block length, or in neutral states where it decreases towards the center of the series. For the constancies of the SOI persistences series, it appears that there is

an anticorrelation between the expected symbol and the symbols of a large fluctuation or a block of large memory. The SST and MEI indices indicate on the other hand a positive correlation between these variables.

Since the distribution of the blocks of the anomalies is concentrated in the constancies and the conditional entropies of the persistences tend in most cases to one, it is a difficult problem to study the most predictable blocks which denote transitions with the actual length of the records. With a procedure which discriminates the most likely blocks to present correlations over one month, the most interesting blocks found pertain to the anomalies of the SOI and SST series. The results of the analysis with the anomalies of SOI show that El Niño and La Niña states behave as attractors, enhancing the predictability of blocks which grow to an extreme state or return after a fluctuation to an intermediate state. The most predictable transitions correspond to states of El Niño, and the predictability for a transition towards La Niña increases with finer partitions. The most predictable transitions are found with the SST series, where transitions to states of El Niño and La Niña have uncertainties below 0.5. It is, however, not possible to look after higher-order correlations with this series, since the distribution of the blocks limits the statistics of the transitions. Relatively low uncertainties of non-constant blocks are found in the persistences series almost exclusively for the coarse binary partitioning.

A wavelet analysis for every index of ENSO enlightens the time structure of the anomalies and persistences series and gives an insight into the properties of the process underlying the time series. Further, to the knowledge of the author, this work presents publishes the first wavelet spectrum of the MEI index. It is found that there is a strong activity of periodicities responsible for El Niño and La Niña between 2 and 8 years before 1920 and since 1965. The time between these intervals appears to be under a smaller influence of periodic perturbations. Large events of El Niño are moreover characterized by the presence of the shortest periods around two years, which stand for two or

more warm phases which merge in a large El Niño. All anomalies series attain variances which are larger than those achieved by chance from the first-order Markov process obtained from the autocorrelation of the index, to a probability of 0.95. These are localized in regions in which constancies and, hence, some mid-range correlations are found, corroborating the results discussed above.

The persistences series of the indices of ENSO show remarkable different wavelet power spectra. While there are no recognizable patterns and no regions significantly different to white noise from the SOI persistence series, the patterns of the spectra of the anomalies of SST are reflected in the spectra of its persistences. Very similar patterns to the SST spectrum are found by taking the wavelet power spectrum of the MEI persistences, even though the latter is affected by length effects. There is little gain in information about the general properties of the time structure of the Southern Oscillation by considering the additional variables taken into account in MEI. This indicates that SST is a good estimator for the overall form of the distribution of frequencies participating in the Southern Oscillation.

The approach applied in this study combines the techniques of entropy analysis and wavelet power spectra to detect and corroborate the most predictable events of the indices of the Southern Oscillation while revealing some dynamical properties of the process. This has been succesfully achieved for the constant events of the anomalies, which are well-behaved in frequency and entropy. Those interested mainly on the transitions should wait until larger data sets are avalaible, compensating the statistical difficulties of the high number of possible transition events. This will be hopefully the case, not until the SOI, Hadley Centre SST and MEI series become much longer, but with the completion of several studies in paleoclimatic series performed thus far. Provided the series are found relatively stationary, it could be possible to detect the difference in the predictabilities for the possible states of the Southern Oscillation. Another aim of this study has been to compare the statistical properties for

a forecast of the three indices of ENSO. As said, SST was found as the most appropriate series, which for some specific events could be in some time be replaced by MEI. As a last, but not least, the differences in information content between the anomalies and persistences have been constantly adressed, and it has been found that it is better to concentrate on the anomalies than in the persistences (or transformations of them). Together, this results represent the main contribution of this work to the scientific community and the populations of living in or surrounding the tropical Pacific.

Chapter 6

Appendix

6.1 Entropies and significances of the SOI, SST and MEI data

Constancies of the SOI anomalies				
block	partitions	entropy	frequency	significance
000	4	0.518098	202	-6.883513
00000	3	0.535290	148	-4.846946
0000	3	0.551226	186	-5.527582
000000	2	0.583468	270	-6.402428
00000	2	0.590503	314	-7.318957
000	3	0.595289	240	-6.289613
00	4	0.595758	240	-5.266694
111111	2	0.631263	187	-5.483289
44	5	0.643819	183	-2.921143
00	3	0.645554	315	-5.365269
00	5	0.647502	170	-3.083338

Constancies of the SOI anomalies (continued)				
block	partitions	entropy	frequency	significance
0000	2	0.654749	324	-7.837209
333	4	0.657320	120	-2.511439
1111	2	0.664825	333	-5.851187
33	4	0.666201	226	-2.940852
000	2	0.666578	435	-7.565865
22222	3	0.677336	113	-2.303438
2222	3	0.690002	157	-2.436835
11111	2	0.693342	229	-4.974776
222	3	0.698848	209	-2.764803
22	3	0.704907	327	-2.599911
111	2	0.765244	384	-4.182693
00	2	0.774405	542	-4.539847
11	2	0.815635	540	-2.488775
111	4	0.906812	34	-0.536121
11	5	0.912917	90	-0.898095
11	4	0.914455	138	-1.849279
33	5	0.930396	84	-0.614778
222	4	0.943832	45	-0.969414
22	4	0.946903	88	-0.554635
22	5	0.962306	80	-0.042720
111	3	0.982887	91	0.350913
11	3	0.990852	214	0.727245

Constancies of the SST anomalies				
block	partitions	entropy	frequency	significance
44	5	0.319542	288	-1.574486
2222	3	0.332943	433	-3.814060

Constancies of the SST anomalies (continued)				
block	partitions	entropy	frequency	significance
222	3	0.335621	487	-4.083103
333	4	0.336354	381	-3.303079
33	4	0.352477	325	-1.494243
22222	3	0.366187	331	-2.600534
22	3	0.374310	413	-4.366916
000000	2	0.382113	576	-4.535329
00000	2	0.396071	624	-4.212323
000	4	.412995	238	-3.190310
0000	2	0.414662	680	-3.881939
000	2	0.422655	743	-3.700375
00	3	0.423752	444	-1.393335
00	4	0.425746	299	-2.234253
00000	3	0.435965	169	-2.550464
00	5	0.438008	221	-1.875712
0000	3	0.441950	203	-3.030112
11	2	0.472189	691	-2.695225
11111	2	0.486716	386	-3.656922
000	3	0.492151	251	-2.148925
1111	2	0.493994	433	-3.793804
111	2	0.501210	487	-3.845463
00	2	0.502298	693	-2.143646
111111	2	0.507089	345	-2.857916
11	5	0.702017	153	-1.208691
33	5	0.710771	150	-1.175928
11	4	0.719550	217	-1.469584
22	5	0.750296	173	-0.242413
22	4	0.761169	235	0.051384

Constancies of the SST anomalies (continued)				
block	partitions	entropy	frequency	significance
222	4	0.764432	89	-2.473250
11111	3	0.785822	118	-0.637268
11	3	0.786759	350	-0.814034
111	3	0.795613	204	-1.546567
111	4	0.801884	68	-1.085331
1111	3	0.845045	136	-0.150711

Constancies of the MEI anomalies				
block	partitions	entropy	frequency	significance
00000	3	0.286318	182	-1.579632
0000	3	0.300479	220	-1.173105
000	4	0.310220	133	-2.017039
00	5	0.317941	128	-1.408359
111111	2	0.325753	233	-2.044559
1111	2	0.327147	265	-2.053687
00	3	0.327690	185	-1.207162
00	4	0.339746	128	-1.172901
11111	2	0.342135	249	-1.802999
111	2	0.342464	280	-1.938961
222	3	0.344134	172	-1.598944
000	3	0.354734	133	-1.823074
22	3	0.356496	194	-1.310576
33	4	0.359427	139	-0.995239
00000	2	0.380281	201	-1.758675
000000	2	0.380947	187	-1.788343
11	2	0.383695	292	-1.041057
44	5	0.387524	116	-1.384909

Constancies of the MEI anomalies (continued)				
block	partitions	entropy	frequency	significance
333	4	0.388689	89	-1.744953
2222	3	0.427411	76	-1.875424
0000	2	0.436770	220	-1.046076
00	2	0.441541	293	-0.168986
000	2	0.454948	249	-0.725187
22222	3	0.465971	66	-1.303862
222	4	0.570961	110	-1.081687
111	3	0.618514	137	-0.866285
22	4	0.632259	122	-0.418209
11111	3	0.648522	77	-0.427756
1111	3	0.655101	84	-1.056205
22	5	0.657875	90	-0.510767
11	4	0.671499	98	-0.498615
11	5	0.681312	55	-1.369884
11	3	0.686603	153	-0.263888
111	4	0.780244	35	-0.350286
33	5	0.786318	44	-0.426103

Constancies of the SOI persistences				
block	partitions	entropy	frequency	significance
0000	2	0.889035	60	-5.111371
000	2	0.892121	108	-2.642959
00	5	0.892698	31	-0.641661
111	2	0.896038	94	-1.490045
00	2	0.898166	297	-3.529821
33	5	0.925441	68	-2.320557
11	2	0.925903	297	-1.799897

Constancies of the SOI persistences (continued)				
block	partitions	entropy	frequency	significance
00	4	0.930514	59	-0.534794
00	3	0.942101	110	-0.513225
22	3	0.943128	116	-0.398417
22	4	0.945881	76	-1.111211
222	4	0.949309	31	-0.209546
33	4	0.956615	53	0.593425
44	5	0.965829	34	0.864766
11	5	0.982227	53	0.642459
22	5	0.994477	67	1.173992
11	4	0.994665	96	0.617128
11	3	0.997901	186	0.767360
111	3	0.999802	65	1.082426

Constancies of the SST persistences				
block	partitions	entropy	frequency	significance
2222	3	0.909584	38	-2.549763
111	4	0.920078	31	-2.107698
0000	3	0.945683	33	-0.565537
22	5	0.959584	89	-1.192949
11111	2	0.961978	68	-1.545701
44	5	0.970580	91	-0.756324
222	3	0.970782	83	-1.024573
11	5	0.974664	64	-0.119585
33	5	0.976381	51	0.243482
1111	2	0.976635	115	-1.567488
000	4	0.983230	38	0.600504
00	4	0.985928	114	0.082078

Constancies of the SST persistences (continued)				
block	partitions	entropy	frequency	significance
111111	2	0.986545	42	0.296653
33	4	0.986972	113	-0.022395
22	4	0.988182	111	-0.005443
00	3	0.988688	206	-0.466085
11	3	0.988994	205	-0.324198
0000	2	0.990762	113	-0.285561
222	4	0.991356	34	0.854374
00	5	0.992424	70	0.972655
000	3	0.992518	84	0.567726
111	3	0.993150	67	0.609173
111	2	0.996111	216	-0.115893
11	4	0.996261	110	0.986402
22	3	0.997056	186	0.634024
11	2	0.997153	412	-0.093552
000000	2	0.997503	32	0.539869
000	2	0.998146	215	0.463835
00	2	0.998933	414	0.452799
00000	2	0.999829	63	0.768730

Constancies of the MEI persistences				
block	partitions	entropy	frequency	significance
000	4	0.779676	39	-4.172022
00	5	0.850686	60	-1.805557
00	4	0.875657	67	-1.982508
44	5	0.904302	45	-1.213411
1111	2	0.933357	61	-2.411062
33	4	0.946469	56	-1.123931

Constancies of the MEI persistences (continued)				
block	partitions	entropy	frequency	significance
0000	2	0.950080	63	-1.288634
000	2	0.954434	102	-2.588874
11111	2	0.958712	40	-0.518856
111	2	0.964800	98	-1.394646
11	4	0.977124	47	0.179280
00000	2	0.985228	40	0.271384
00	2	0.986194	179	-0.247861
22	4	0.990702	38	0.737501
11	2	0.993627	179	0.545311
222	4	0.887929	9	-1.326973
44	5	0.904302	45	-1.213411
333	4	0.922470	24	-0.585278
1111	2	0.933357	61	-2.411062
000000	2	0.942683	23	-0.274123
33	4	0.946469	56	-1.123931
0000	2	0.950080	63	-1.288634
11	5	0.953115	22	-0.139142
22	5	0.953583	24	-0.170436
000	2	0.954434	102	-2.588874
11111	2	0.958712	40	-0.518856
111	2	0.964800	98	-1.394646
33	5	0.966661	24	0.325291
111111	2	0.975119	25	0.289582
11	4	0.977124	47	0.179280
00000	2	0.985228	40	0.271384
00	2	0.986194	179	-0.247861
22	4	0.990702	38	0.737501

Constancies of the MEI persistences (continued)				
block	partitions	entropy	frequency	significance
11	2	0.993627	179	0.545311
111	4	0.995538	14	1.122949

6.2 Entropies of the transitions of the SOI, SST and MEI data

Transitions of the SOI anomalies				
block	partitions	entropy	frequency	significance
10000	3	0.653678	31	-2.025641
100000	2	0.666578	44	-2.798596
0100	3	0.676819	34	-1.746667
100	4	0.706403	43	-1.053394
100	3	0.730233	79	-1.233432
233	4	0.734715	41	-1.053749
122	3	0.751645	71	-1.186797
01111	2	0.804252	55	-1.230471
1000	2	0.821813	72	-1.021731
01	5	0.860195	64	-3.109431
001	4	0.860546	44	-2.443958
0001	3	0.864523	43	-5.335517
00001	3	0.869916	32	-3.763861
31	5	0.884245	48	-1.334929
42	5	0.903969	36	-1.765472
322	4	0.909715	32	-1.629716
101	3	0.916308	61	-1.247227
001	3	0.928127	81	-1.811372

Transitions of the SOI anomalies (continued)				
block	partitions	entropy	frequency	significance
211	3	0.928928	60	-1.674639
22221	3	0.931672	34	-1.325572
332	4	0.933201	44	-1.597529
32	4	0.937146	96	-1.364540
01	3	0.956815	152	-1.229406

Transitions of the SST anomalies				
block	partitions	entropy	frequency	significance
11000	2	0.365055	41	-1.949877
011111	2	0.365055	41	-2.824272
12222	3	0.399988	44	-1.520250
00111	2	0.405977	35	-2.324015
111000	2	0.422001	33	-1.406454
000111	2	0.430552	32	-1.933983
2111	3	0.668184	33	-2.532567
12	5	0.695212	74	-1.953956
32	4	0.715390	64	-1.251553
01	3	0.755133	94	-1.061563
0111	3	0.766916	35	-1.035308

Transitions of the MEI anomalies				
block	partitions	entropy	frequency	significance
221	3	0.578006	22	-1.402150
32	5	0.631984	26	-1.873228

Transitions of the SOI persistences				
block	partitions	entropy	frequency	significance
01101	2	0.760786	57	-2.542603
212	3	0.776750	40	-4.488909
0212	3	0.813652	31	-3.074736
1101	2	0.824363	87	-2.285464
0111	2	0.831474	55	-1.472394
001101	2	0.863121	33	-1.305496
01	5	0.865920	33	-3.498455
101101	2	0.881291	38	-1.598793
01	4	0.892758	82	-7.368113
110	3	0.893953	65	-1.678685
24	5	0.899714	64	-1.905629
10000	2	0.902393	42	-3.629825
23	4	0.903141	62	-1.053776
12	3	0.904509	160	-2.740986
13	4	0.910659	105	-1.650461
32	4	0.912157	73	-2.588033
10	3	0.916284	164	-1.747799
23	5	0.924885	54	-1.674599
02	5	0.927203	55	-2.715905
211	4	0.933041	37	-1.216586
101	3	0.939925	55	-2.683606
100	2	0.947062	206	-1.370734
121	3	0.950918	50	-1.611432
02	4	0.954465	99	-1.111901
32	5	0.957978	50	-1.127427
211	3	0.965989	56	-1.228862

Transitions of the SOI persistences (continued)				
block	partitions	entropy	frequency	significance
01	3	0.969355	164	-3.545197
0100	2	0.976182	147	-1.144602
21	3	0.985035	159	-1.345244

Transitions of the SST persistences				
block	partitions	entropy	frequency	significance
110	3	0.921094	54	-2.928603
303	4	0.921933	35	-1.462236
012	3	0.930923	51	-2.697332
112	3	0.935862	61	-3.125366
11100	2	0.939255	57	-2.834783
13	5	0.945923	46	-1.410021
04	5	0.948689	71	-1.553449
42	5	0.949215	58	-1.258136
24	5	0.955045	60	-1.056981
41	5	0.957760	58	-1.086386
01110	2	0.959316	53	-1.453708
11001	2	0.960119	45	-1.278765
10000	2	0.961237	50	-1.395268
200	3	0.965519	53	-1.375938

Transitions of the MEI persistences				
block	partitions	entropy	frequency	significance
11000	2	0.828056	21	-2.886548
0101	2	0.881291	28	-1.757788
01111	2	0.886541	21	-1.284144

Transitions of the MEI persistences (continued)				
block	partitions	entropy	frequency	significance
10000	2	0.890492	24	-1.976673
21	5	0.919986	23	-1.749292
101	2	0.927926	65	-2.495555

Bibliography

[1] K. AchutaRao and K.R. Sperber. Simulation of the El Niño Southern Oscillation: Results form the Coupled Model Intercomparison Project. *Clim. Dyn.*, 19:191–209, 2002.

[2] V.S. Anishchenko, V.V. Astakhov, A.B. Neiman, T.E. Vadivasova, and L. Schimansky-Geier. *Nonlinear dynamics of chaotic and stochastic systems*. Springer, Berlin, 2001.

[3] M. Ausloos and K. Ivanova. Power law correlations in the Southern Oscillation Index fluctuations characterizing El Nino. *ArXiv Condensed Matter e-prints*, March 2001.

[4] S. Baliunas, P. Frick, D. Sokoloff, and W. Soon. Time scales and trends in the central England temperature data (1659-1990): A wavelet analysis. *Geophys. Res. Lett.*, 24:1351–1354, 1997.

[5] M.A. Balmaseda, D.L.T. Anderson, and M.K. Davey. ENSO prediction using a dynamical ocean model coupled to statistical atmospheres. *Tellus*, 46A:497–511, 1994.

[6] M.A. Balmaseda, M. K. Davey, and D.L.T. Anderson. Decadal and seasonal dependence of ENSO prediction skill. *J. Climate*, 8:2705–2715, 1995.

[7] R.T. Barber and F.P. Chavez. Biological consequences of El Niño. *Science*, 222:1203–1210, 1983.

[8] R.T. Barber and F.P. Chavez. Ocean variability in relation to living resources during the 1982-83 El Niño. *Nature (London)*, 319:279–285, 1986.

[9] T.P. Barnett. Statistical relation between ocean/atmosphere fluctuations in the tropical Pacific. *J. Phys. Oceanogr.*, 11:1043–1058, 1981.

[10] D.S. Battisti. The dynamics and thermodynamics of a warming event on a coupled tropical atmosphere-ocean model. *J. Atmos. Sci.*, 45:2889–29919, 1988.

[11] D.S. Battisti and A.C. Hirst. Interannual predictability in the tropical ocean system: influence of the basic state and ocean geometry. *J. Atmos. Sci.*, 46:1687–1712, 1989.

[12] C. Beck and F. Schlögl. *Thermodynamics of chaotic systems*. Cambridge University Press, Cambridge, 1993.

[13] J. Bjerknes. A possible response of atmospheric Hadley circulations to equatorial anomalies of ocean temperature. *Tellus*, 18:820–829, 1966.

[14] A. Bunde, J. Kropp, and H.-J. Schellnhuber. *The science of disasters*. Springer, Berlin, 2002.

[15] L.L. Campbell. A coding theorem and Rényi's entropy. *Inform. Contr*, 8:423–429, 1965.

[16] M. Casdagli and S. Eubank (eds.). Nonlinear modeling and forecasting. In *Santa Fe Studies in the Sciences of Complexity*. Addison-Wesley, Reading, Mass. USA, 1992.

[17] C.M. Caviedes. El Niño 1982-83. *Geogr. Rev.*, 74:267–290, 1984.

[18] P. Chang, B. Ji, and T. Li. Interactions between the seasonal cycle and ENSO-frequency entrainment and chaos in a coupled ocean-atmosphere model. *Geophys. Res. Lett.*, 21:2817–2820, 1995.

[19] P. Chang, H. Li, and M. Flügel. Chaotic dynamics versus stochastic processes in El Niño-Southern Oscillation in coupled ocean-atmosphere models. *Phys. D*, 98:301–320, 1996.

[20] I. Csiszer. A class of measures of informativity of observation channels. *Periodic Math. Hungarica*, 2:191–213, 1972.

[21] I. Daubechies. The wavelet transform time-frequency localization and signal analysis. *IEEE Trans. Inform. Theory*, 36:961–1004, 1990.

[22] W. Ebeling, H. Engel, and H. Herzel. *Selbstorganisation in der Zeit.* Akademie Verlag, Berlin, 1990.

[23] W. Ebeling, J. Freund, and F. Schweitzer. *Komplexe Strukturen: Entropie und Information.* B.G. Teubner, Stuttgart/Leipzig, 1998.

[24] W. Ebeling, M.A. Jiménez-Montaño, and T. Pohl. Entropy and complexity of sequences. In Karmeshu, editor, *Entropy Measures, maximum entropy principle and emerging applications*, New Delhi, 2003. Springer.

[25] W. Ebeling, L. Molgedey, J. Kurths, and U. Schwartz. Entropy, complexity, predictability and data analysis of time series and letter sequences. In *Theory of disasters: Scaling laws governing weather, body and stock market*, Berlin, 2000. Springer.

[26] W. Ebeling, R. Steuer, and M.R. Titchener. Partition-based entropies of deterministic and stochastic maps. *Stochastic and Dynamics*, 1:45–61, 2001.

[27] J.P. Eckmann and D. Ruelle. Ergodic theory of chaos and strange attractors. *Rev. Mod. Phys.*, 57(3), 1985.

[28] A. V. Fedorov and S. G. Philander. Is El Niño changing? *Science*, 288:1997–2001, 2000.

[29] A.V. Fedorov, S.L. Harper, S.G. Philander, B. Winter, and A. Wittenberg. How predictable is El Niño? *Bull. Am. Met. Soc.*, 84:911–919, 2003.

[30] R. Feistel. A new extended thermodynamic potential of seawater. *Prog. Oceanog.*, 58:43–114, 2003.

[31] K. Fraedrich. El Niño/Southern Oscillation predictability. *Mon. Weather Rev.*, 116:1001–1012, 1988.

[32] E. Galanti and E. Tziperman. ENSO's phase locking to the seasonal cycle in the fast-SST, fast-wave and mixed-mode regimes. *J. Atmos. Sci.*, 57:2936–2950, 2000.

[33] R.S. Gardiner-Garden. *Some aspects of modeling the vertical structure of currents in wind-forced coastal upwelling systems.* PhD Dissertation, Princeton University, Princeton, New Jersey, 1987.

[34] A.E. Gill. *Atmosphere-Ocean Dynamics.* Academic Press, New York, 1982.

[35] A.E. Gill. *Coupled ocean-atmosphere models.* Elsevier, Amsterdam, 1985.

[36] N.E. Graham, J. Michaelsen, and T.P. Barnett. An investigation of the El Niño-Southern Oscillation cycle with statistical models, part 1: Predictor field characteristics. *J. Geophys. Res.*, 92:1425, 1987.

[37] N.E. Graham, J. Michaelsen, and T.P. Barnett. An investigation of the El Niño-Southern Oscillation cycle with statistical models, part 2: Model results. *J. Geophys. Res.*, 92:1427, 1987.

[38] P. Grassberger. Finite sample corrections to entropy and dimension estimates. *Phys. Lett. A.*, 128:97–113, 1994.

[39] P. Grassberger and H. Kantz. Generating partitions for the dissipative Hénon map. *Physics Letters*, 113A(5), 1985.

[40] I. Grosse. *Statistical analysis of biosequences.* Diplomarbeit, Humboldt University, Berlin, 1995.

[41] I. Grosse. Estimating entropies from finite samples. In J. Freund, editor, *Dynamik, Evolution, Strukturen*, Berlin, 1996. Akademie Verlag.

[42] J. Havrda and F. Charvat. Quantification method of classification processes: concept of structural $\alpha-$entropy. *Kybernetika*, 3:30–35, 1967.

[43] H. Herzel. Finite sample effects in sequence analysis. *Chaos, Solitons & Fractals*, 4:97–113, 1994.

[44] H. Herzel, W. Ebeling, and A.O. Schmitt. Entropies of biosequences: The role of repeats. *Phys. Rev. E*, 50(4):5061–5071, 1994.

[45] H.H. Hildebrandsson. Quelque recherches sur les entres d'action de l'atmosphere. *K. Sven. Vetenskaps akad. Handl.*, 29:1–33, 1897.

[46] D. Holste. *Statistische Analyse mit verallgemeinerte Entropien.* Diplomarbeit, Humboldt University, Berlin, 1997.

[47] B. Huang and E.K. Schneider. The response of an ocean general circulation model to surface wind stress produced by an atmospheric general circulation model. *Mon. Weather Rev.*, 1999. Forecasts are published at http://www.iges.org./ellfb.

[48] E.T. Jaynes. Information theory and statistical mechanics. *Phys. Rev.*, 106, 1957.

[49] E.T. Jaynes. Information theory and statistical mechanics II. *Phys. Rev.*, 108, 1957.

[50] M. Ji, A. Leetma, and V.E. Kousky. Coupled model predictions of ENSO during the 1980s and 1990s at the National Centers for Environmental Prediction. *J. Climate*, 9:3105–3120, 1997.

[51] M.A. Jiménez-Montaño, W. Ebeling, T. Pohl, and P.E. Rapp. Entropy and complexity of finite sequences as fluctuating quantities. *Biosystems*, 64:23–32, 2001.

[52] H. Kantz and T. Schreiber. *Nonlinear time series analysis*. Cambridge University Press, Cambridge, 1997.

[53] J.N. Kapur. *Maximum entropy models in science and engineering*. Wiley Eastern Ltd., New Delhi, 1989.

[54] A. Khinchin. *Mathematical Foundation of Information Theory*. Dover, New York, 1967.

[55] E. Koscielny-Bunde, A. Bunde, S. Havlin, H.E. Roman, Y. Goldreich, and H.-J. Schellnhuber. Indication of a universal persistence law governing atmospheric variability. *Phys. Rev. Lett.*, 81:729–732, 1998.

[56] S. Kullback. *Information Theory and Statistics*. Wiley, New York, 1951.

[57] S. Kullback and R.A. Leibler. On information and sufficiency. *Annals Math. Stat.*, 2, 1951.

[58] M. Latif and M. Flügel. An investigation of short-range climate predictability in the tropical Pacific. *J. Geophys. Res.*, 96:2661–2673, 1991.

[59] M. Latif, K. Sperber, J. Arblaster, P. Braconnot, D. Chen, A. Colman, U. Cubasch, C. Cooper, P. Delecluse, D. Dewitt, L. Fairhead, G. Flato, T. Hogan, M. Ji, M. Kimoto, A. Kitoh, T. Knutson, H. Le Treut, T. Li, S. Manabe, O. Marti, C. Mechoso, G. Meehl, S. Power, E. Roeckner, J. Sirven, L. Terray, A. Vintzileos, R. Voss, B. Wang, W. Washington, I. Yoshikawa, J Yu, and S. Zebiak. ENSIP: The El Niño Simulation Intercomparison Project. *Clim. Dyn.*, 18:255–276, 2001.

[60] K.-M Lau and H.-Y. Weng. Climate signal detection using wavelet transform: How to make a time series sing. *Bull. Amer. Meteor. Soc.*, 76:2391–2402, 1995.

[61] W. Li and K. Kaneko. On the relationship between complexity and entropy for Markov chains and regular languages. *Complex Systems*, 5, 1991.

[62] R.W. Lindsay, D.B. Percival, and D.A. Rothrock. The discrete wavelet transform and the scale analyis of the surface properties of sea ice. *IEEE Trans. Geosci. Remote Sens.*, 34:771–787, 1996.

[63] N. Lockyer and W.J.S. Lockyer. On some phenomena which suggest a short period of solar and meteorological changes. *Proc. R. Soc. London*, 70:500, 1902.

[64] N. Lockyer and W.J.S. Lockyer. On the similarity of the short-period pressure variation over large areas. *Proc. R. Soc. London*, 71:134–135, 1902.

[65] O.A. Lucero and N.C. Rodriguez. Statistical characteristics of interdecadal fluctuations in the southern oscillation and the surface temperature of the equatorial pacific. *Atmos. Res.*, 54:87–104, 2000.

[66] A.M. Mathai and P.M. Rathie. *Basic concepts in information theory.* John Wiley and Sons, 1975.

[67] C.R. Mechoso. The seasonal cycle over the tropical Pacific in general circulation models. *Mon. Weather Rev.*, 123:2825–2838, 1995.

[68] S.D Meyers, B.G. Kelly, and J.J. O'Brien. An introduction to wavelet analysis in oceanography and meteorology: with application to the dispersion of Yanai waves. *Mon. Wea. Rev.*, 121:2858–2866, 1993.

[69] L. Molgedey and W. Ebeling. Local order, entropy and predictability of financial time series. *Eur. Phys. J. B*, 15:733–737, 2000.

[70] M. Münnich, E.A. Cane, and S.E. Zebiak. A study of self-excited oscillations of the tropical ocean-atmosphere system. Part II: Nonlinear cases. *J. Atmos. Sci.*, 48:1238–1248, 1991.

[71] E.C. Murphy. Oceanic and climatic phenomena along the west coast of South America during 1925. *Geogr. Rev.*, pages 26–54, 1926.

[72] P. Nath. On a coding theorem connected with Rényi's entropy. *Inform. Contr.*, 29:234–242, 1975.

[73] D. Neelin. A note on the interpretation of the Gill Model. *J. Atmos. Sci.*, 46:2466–2468, 1989.

[74] J.D. Neelin. Interannual oscillations in an ocean GCM simple atmospheric model. *Philos. Trans. Roy. Soc. London Ser. A*, 329:189–205, 1989.

[75] C. Nicolis, W. Ebeling, and C. Baraldi. Markov processes, dynamic entropies and the statistical prediction of mesoscale weather regimes. *Tellus*, 49A:108–118, 1997.

[76] E. Ortiz-Tánchez, W. Ebeling, and K. Lanius. MEI, SOI and mid-range correlations in the onset of El Niño-Southern Oscillation. *Phys. A*, 310:509–520, 2002.

[77] M. Paluš. Coarse-grained entropy rates for characterization of complex time series. *Phys. D*, 93:64–77, 1996.

[78] M. A. Paluš, L. Pecen, and D. Pivka. Estimating probability: redundancy and surrogate data method. *Neur. Net. World*, 4:537–552, 1995.

[79] A.N. Pavlov, W. Ebeling, L. Molgedey, A.R. Ziganshin, and V.S. Anishchenko. Scaling features of texts, images and time series. *Phys. A*, 300:310–324, 2001.

[80] F. Pearce. Sneaky El Niño outwits weather forecasters. *New Scientist*, may 1997.

[81] J. Pedlosky. *Geophysical Fluid Dynamics*. Springer-Verlag, New York, 1987.

[82] C.K. Peng, S.V. Buldyrev, S. Havlin, M. Simons, H.E. Stanley, and A.L. Goldberger. Mosaic organization of DNA nucleotides. *Phys. Rev. E*, 49:1685–1689, 1994.

[83] C. Penland. A stochastic model of the IndoPacific sea surface temperature anomalies. *Phys. D*, 98:534–558, 1996.

[84] S.G. Philander. *El Niño, La Niña and the Southern Oscilllation*. Academic Press, San Diego, California, USA, 1990.

[85] S.G. Philander, R.C. Pacanowski, R.C. Lau, and M.J. Nath. Simulation of ENSO with a global atmospheric GMC coupled to a high-resolution, tropical Pacific ocean GCM. *J. Climate*, 5:308–329, 1992.

[86] S.G.H. Philander, T. Yamagata, and R.C. Pacanowski. Unstable air-sea interactions in the tropics. *J. Atmos. Sci*, 41:604–613, 1984.

[87] A. Politi and F. Christiansen. Generating partitions for standard map. *Physical Review E*, 51(5), 1995.

[88] R.W. Preisendorfer and C.D. Mobley. *Principal Component Analysis in Meteorology and Oceanography.* Elsevier Science, 1988.

[89] M. Priestley. *Spectral analysis and time series.* Academic Press, New York, 1981.

[90] N. Radhakrishnan, J.D. Wilson, and P. Loizou. An alternate partitioning technique to quantify the regularity of complex time series. *Int. J. Bifurc. Chaos*, 10(7):1773–1779, 2000.

[91] E.M. Rasmusson and T.H. Carpenter. Variations in tropical sea surface temperature and surface wind fields associate with the Southern Oscillation/El Niño. *Mon. Weather Rev.*, 110:354–384, 1982.

[92] N.A. Rayner, D.E. Parker, E.B. Horton, C.K. Folland, L.V. Alexander, D.P. Rowell, E.C. Kent, and A. Kaplan. Global analyses of SST, sea ice and night marine air temperature since the late nineteenth century. *J. Geophys. Res.*, 108:4407, 2003.

[93] A. Rényi. On measures of entropy and information. In *Proc. Fourth Berkeley Simp. Math. Statist. and Probability*, volume 1, pages 547–561, 1961.

[94] R. Schlittgen and B. Streitberg. *Zeitreihenanalyse.* Oldenbourg Verlag, Munich/Vienna, 1987.

[95] R.W. Schreiber and E.A. Schreiber. Central Pacific seabirds and El Niño Southern Oscillation: 1982 to 1983 perspectives. *Science*, 225:713–716, 1984.

[96] T. Schreiber. Constrained randomization of time series data. *Phys. Rev. Lett*, 80:2105, 1998.

[97] T. Schreiber and A. Schmitz. Surrogate time series. *Phys. D*, 142:346–382, 2000.

[98] H.G. Schuster. *Deterministic Chaos: An introduction*. VCH, Weinheim, 1989.

[99] C.E. Shannon. A mathematical theory of communication. *The Bell Systems Technical Journal*, 27:379–423, 623–656, 1948.

[100] J.E. Shore and R.W. Johnson. Axiomatic derivation of the principle of maximum entropy and minimum cross entropy. *IEEE Trans. Inf. Th.*, 26, 1980.

[101] H.E. Stanley, S.V. Buldyrev, A.L Goldberger, Z.D. Goldberger, S. Havlin, R. N. Mantegna, C. K. Peng, and M. Simon. Statistical mechanics in biology: how ubiquitous are long-range correlations? *Physica A*, 205:214–253, 1994.

[102] R. Steuer. *Die Shannon-Entropie: Analyse und Vorhersagbarkeit von empirischen Zeitreihen*. Diplomarbeit, Humboldt University, Berlin, 2001.

[103] R. Steuer, W. Ebeling, D.F. Russel, S. Bahar, A. Neiman, and F. Moss. Entropy and local uncertainty of data from sensory neurons. *Phys. Rev. E*, 64:061911, 2001.

[104] R. Steuer, L. Molgedey, W. Ebeling, and M.A. Jiménez Montaño. Entropy and optimal partition for data analysis. *Eur. Phys. J. B*, 19:265–269, 2001.

[105] T.N. Stockdale, D.L.T. Anderson, J.O.S Alves, and M.A. Balmaseda. Global seasonal reinfall forecasts using a coupled ocean-atmosphere model. *Nature*, 392:370–373, 1998.

[106] M.J. Suarez and P.S. Schopf. A delayed action oscillator for ENSO. *J. Atmos. Sci.*, 45:549–566, 1988.

[107] I.J. Taneja. On generalized information measures and their applications. *Adv. Electronics and Electron Phys.*, 76:327–412, 1989.

[108] G.I. Taylor. Experiments of the motion of solid bodies in rotating fluids. *Proc. Roy. Soc. A*, 104:213–218, 1923.

[109] J. Theiler, S. Eubank, A. Longtin, B. Galdrikian, and J.D. Farmer. Testing for nonlinearity in time series: the method of surrogate data. *Phys. D*, 58:77, 1992.

[110] J. Theiler and D. Prichard. Constrained-realization Monte-Carlo method for hypothesis testing. *Phys. D*, 94:221, 1996.

[111] C.J. Thompson and D.S. Battisti. A linear stochastic dynamical model of ENSO. Part I: Model development. *J. Climate*, 13:2818–2832, 2000.

[112] C.J. Thompson and D.S. Battisti. A linear stochastic dynamical model of ENSO. Part II: Analysis. *J. Climate*, 14:445–466, 2001.

[113] A. Timmermann, J. Oberhuber, A. Bacher, M. Esch, M. Latif, and E. Roeckner. Increased El Niño frequency in a climate model forced by future greenhouse warming. *Nature*, 398:694–696, 1999.

[114] C. Torrence and G.P. Compo. A practical guide to wavelet analysis. *Bull. Amer. Meteor. Soc.*, 79:61–76, 1998. Wavelet software can be found at paos.colorado.edu/research/wavelets/software.html.

[115] K.E. Trenberth. The definition of El Niño. *Bull. Am. Met. Soc.*, 78:2771–2777, 1997.

[116] A.J. Troup. The Southern Oscillation. *Quart. J. Roy. Meteor. Soc.*, 91:490–506, 1965.

[117] C. Tsallis. Possible generalizations of Boltzmann-Gibbs statistics. *J. Stat. Phys.*, 52(1/2):479–487, 1988.

[118] E. Tziperman, L. Stone, M.A. Cane, and H. Jarosh. El Niño Chaos: overlapping of resonances between the seasonal cycle and the Pacific ocean-atmosphere oscillator. *Science*, 264:72–74, 1994.

[119] G.K. Vallis. Conceptual models of El Niño and the Southern Oscillations. *J. Geophys. Res.*, 93C:13 979–13 991, 1988.

[120] G.J. van Oldenborgh. What caused the onset of the 1997-1998 El Niño? *ArXiv Physics e-prints*, apr 1999.

[121] C. Frömmel W. Ebeling. Entropy and predictability of information carriers. *BioSystems*, 46:47–55, 1998.

[122] G.T. Walker. Correlation in seasonal variations of weather. VIII. a preliminary study of world weather. *Mem. Indian Meteorol. Dep.*, 24(4):75–131, 1923.

[123] G.T. Walker and E.W. Bliss. World weather VI. *Mem. R. Meteorol. Soc.*, 4:119–139, 1937.

[124] B. Wang. Interdecadal changes in El Niño onset in the last four decades. *J. Climate*, 8:267–285, 1995.

[125] B. Wang, A. Barcilon, and Z. Fang. Stochastic dynamics of El Niño-Southern Oscillation. *J. Atmos. Sci.*, 56:5–23, 1999.

[126] B. Wang and Z. Fang. Chaotic oscillations of tropical climate: a dynamic system theory for ENSO. *J. Atmos. Sci.*, 53:2786–2802, 1996.

[127] B. Wang and Y. Wang. Temporal structure of the southern oscillation as revealed by waveform and wavelet analysis. *J. Climate*, 9:1586–1598, 1996.

[128] R. Weber and P. Talkner. Spectra and correlations of climate data from days to decades. *J. Geophys. Res.*, 106:20131–20144, 2001.

[129] A. S. Weigend and N. A. Gershenfeld (eds.). Time series prediction: Forecasting the future and understanding the past. In *Santa Fe Studies in the Sciences of Complexity*. Addison-Wesley, Reading, Mass. USA, 1993.

[130] H. Weng and K.-M. Lau. Wavelets, period doubling, and time-frequency localization with application to organization of convection over the tropical western Pacific. *J. Atmos. Sci.*, 51:2523–2541, 1994.

[131] P.C. Werner, F.-W. Gerstengarbe, and W. Ebeling. Changes in probability of sequences, exit time distribution and dynamical entropy in the Potsdam temperature record. *Theor. Appl. Climatol.*, 62:125–132, 1999.

[132] D.H. Wolpert and D.R. Wolf. Estimating functions of probability distributions from a finite set of samples. *LANL Rep.*, 1993.

[133] K. Wolter and M.S. Timlin. Monitoring ENSO in COADS with a seasonally adjusted principal component index. In *Proc. of the 17th Climate Diagnostics Workshop*, pages 52–57. University of Oklahoma, 1993.

[134] Y. Xue, M.A. Cane, S.E. Zebiak, and M.B. Blumenthal. On the prediction of ENSO: a study with a low-order Markov model. *Tellus*, 46 A:512–528, 1994.

[135] S.E. Zebiak and M.A. Cane. A model El Niño-Southern Oscillation. *Mon. Weather Rev.*, 115:2262–2278, 1987.

Aknowledgments

I thank Prof. Dr. Werner Ebeling for his invaluable support; Prof. Dr. Karl Lanius, Dr. Rainer Feistel and Prof. Dr. P. Talkner for enlightening discussions and Professors Eli Tziperman at Harvard and Bing Wang in Hawaii for their models, data and kind correspondence. Much of my scientific relationship to El Niño has been developed as a result of visits to the activities at the International Centre for theorethical Physics in Trieste. Special thanks to my friends Ramón Xulvi Brunet, Katharina Meier, Dagmar Rosengarten, Ana García, Gunnar Lorenzen and the team at the Microbiology Department of the Laboratorio Andaluz de Biología in Seville, for their support during the final stage of my work, and to Ross Benjamin and Karl Taylor-Robinson, for their help with the English languange. It would have been impossible to realize this work without the help of the german Catholic Academic Foreigners' Service (KAAD) for financing my research, and without the endless support of my wife Jutta and my mother Laura.

Selbständigkeitserklärung

Hiermit erkläre ich, die vorliegende Arbeit selbständig ohne fremde Hilfe verfaßt und nur die angegebene Literatur und Hilfsmittel verwendet zu haben.

Luis Eduardo Ortiz Tánchez
15. April 2004